Electronic transport, Fermi surface properties, and lattice dynamics of some topological semimetals

By

Ratnadwip Singha

PHYS05201404002

Condensed Matter Physics Division

Saha Institute of Nuclear Physics, Kolkata

A thesis submitted to the
Board of Studies in Physical Sciences

in partial fulfillment of the requirements

for the Degree of

DOCTOR OF PHILOSOPHY

of

HOMI BHABHA NATIONAL INSTITUTE

May 2019

Homi Bhabha National Institute

Recommendations of the Viva Voce Committee

As members of the Viva Voce Committee, we certify that we have read the dissertation prepared by **Ratnadwip Singha** entitled **"Electronic transport, Fermi surface properties, and lattice dynamics of some topological semimetals"** and recommend that it may be accepted as fulfilling the thesis requirement for the award of Degree of Doctor of Philosophy.

Chairman - Prof. Pradeep Kumar Mohanty	**Date:** 02/07/2019
Guide / Convener - Prof. Prabhat Mandal P. Mandal	**Date:** 2.7.2019
Co-guide -	**Date:**
Examiner – Prof. Pratap Raychaudhuri	**Date:** 2/7/19
Member 1- Prof. Satyaranjan Bhattacharyya	**Date:** 2/7/2019
Member 2- Prof. Dipten Bhattacharyya	**Date:** 2.7.2019

Final approval and acceptance of this thesis is contingent upon the candidate's submission of the final copies of the thesis to HBNI.
I hereby certify that I have read this thesis prepared under my direction and recommend that it may be accepted as fulfilling the thesis requirement.

Date: 2.7.2019

Place: Kolkata

P. Mandal
Prof. Prabhat Mandal
Guide

STATEMENT BY AUTHOR

This dissertation has been submitted in partial fulfillment of requirements for an advanced degree at Homi Bhabha National Institute (HBNI) and is deposited in the library to be made available to borrowers under rules of the HBNI.

Brief quotations from this dissertation are allowable without special permission, provided that accurate acknowledgement of source is made. Requests for permission for extended quotation from or reproduction of this manuscript in whole or in part may be granted by the Competent Authority of HBNI when in his or her judgment the proposed use of the material is in the interests of scholarship. In all other instances, however, permission must be obtained from the author.

Ratnadwip Singha

Ratnadwip Singha

DECLARATION

I, hereby, declare that the investigation presented in the thesis has been carried out by me. The work is original and the work has not been submitted earlier as a whole or in part for a degree/diploma at this or any other Institution or University.

Ratnadwip Singha

Ratnadwip Singha

To my parents

ACKNOWLEDGEMENTS

This thesis is the result of the collaborative efforts and team work for last five years, where numerous people have relentlessly contributed directly or indirectly. So, at this time of acknowledging, I may miss few of them and like to apologize in advance.

First of all, I express my gratitude to my thesis advisor Prof. Prabhat Mandal, Saha Institute of Nuclear Physics (SINP), Kolkata for providing me the opportunity to work in the fascinating field of topological materials, which emerged just few years before I started my doctoral work. His willingness to explore new field of research, adopt new experimental techniques and methodology have enabled me to independently pursue different problems, while working on a fixed project. But above all, I admire him as a great person and mentor, who inspires us with his deep insight on the subject, hour-long discussions, constructive criticisms and encouragement whenever we had any failures. His support even beyond the academia to personal level has made this thesis a reality and these years truly memorable to me.

I like to thank my collaborators, Prof. Biswarup Satpati (SINP), Prof. Tanmoy Das (IISc), Prof. Achintya Singha (Bose Institute), Prof. Lin Wang (HPSTAR), Dr. Sudeshna Samanta (HPSTAR), and Dr. Swastika Chatterjee (IISER Kolkata), who have provided their valuable experimental and theoretical inputs for different works related to this thesis. I am also thankful to them for their eagerness to help me understand the important aspect of their works and clarify any doubt or confusion.

I feel fortunate to work in a well-equipped laboratory with doctoral and post-doctoral students working in close collaboration with each other in a friendly environment. Each of them has expertise in certain directions and is always ready to share with others. It helped me to learn various things that may not only be reflected in the published works. I thank Dr. Nazir Khan, Dr. Arindam Midya, Dr. Dilip Kumar Bhoi, Dr. Prosenjit Sarkar, Dr. Biswanath Samantaray, Prithwish Dutta, Dr. Moumita Nandi, Dr. Arnab Pariari, Susmita Roy, Shubhankar Roy, Moumita Das, Suchanda Mondal, and Dr. Venkatesh Chandragiri for their help and support throughout this thesis work. I like to specially thank Arun Kumar

Paul for his technical help while performing the experiments, regularly trying to repair broken instruments as well as designing and fabricating new experimental set-ups. I also appreciate him for his support even if we come up with a new plan, which is destined to fail. I acknowledge all the members of the condensed matter physics division, SINP and institute's mechanical workshop for their help at various levels.

I am very thankful to SINP, Department of Atomic Energy, Government of India for the generous financial support through research fellowship, travel grants and research funding for carrying out this doctoral work.

Finally, my deepest gratitude to my family, without whom this thesis would not be possible. I like to thank my elder sister, who always stood by me as best friend and took up all my responsibilities so that I can chase my own dreams. My parents always remind me about my roots, tell me to stay humble, patient and never back off from the hard work to achieve even the smallest things in life. But most importantly, their sacrifices, support, and teachings have inspired me to be good person above all. I believe, this thesis belongs to them more than to me.

List of Publications

A. Publications in peer-reviewed journals

(Included in the thesis)

1. "Large nonsaturating magnetoresistance and signature of nondegenerate Dirac nodes in ZrSiS", **Ratnadwip Singha**, Arnab Kumar Pariari, Biswarup Satpati, and Prabhat Mandal, *Proceedings of the National Academy of Sciences of USA* **2017**, 114, 2468.

2. "Fermi surface topology and signature of surface Dirac nodes in LaBi", **Ratnadwip Singha**, Biswarup Satpati, and Prabhat Mandal, *Scientific Reports* **2017**, 7, 6321.

3. "Magnetotransport properties and evidence of a topological insulating state in LaSbTe", **Ratnadwip Singha**, Arnab Pariari, Biswarup Satpati, and Prabhat Mandal, *Physical Review B* **2017**, 96, 245138.

4. "Probing lattice dynamics and electron-phonon coupling in the topological nodal-line semimetal ZrSiS", **Ratnadwip Singha**, Sudeshna Samanta, Swastika Chatterjee, Arnab Pariari, Dipanwita Majumdar, Biswarup Satpati, Lin Wang, Achintya Singha, and Prabhat Mandal, *Physical Review B* **2018**, 97, 094112.

5. "Probing the Fermi surface and magnetotransport properties of $MoAs_2$", **Ratnadwip Singha**, Arnab Pariari, Gaurav Kumar Gupta, Tanmoy Das, and Prabhat Mandal, *Physical Review B* **2018**, 97, 155120.

6. "Planar Hall effect in the type-II Dirac semimetal VAl_3", **Ratnadwip Singha**, Shubhankar Roy, Arnab Pariari, Biswarup Satpati, and Prabhat Mandal, *Physical Review B (Rapid Communication)* **2018**, 98, 081103(R).

(Not included in the thesis)

7. "Tuning the scattering mechanism in the three-dimensional Dirac semimetal Cd_3As_2", Arnab Pariari, Nazir Khan, **Ratnadwip Singha**, Biswarup Satpati, and Prabhat Mandal, *Physical Review B* **2016**, 94, 165139.

8. "Magnetic ordering induced ferroelectricity in α-$Cu_2V_2O_7$ studied through non-magnetic Zn doping", Bidisa Chattopadhyay, Md A. Ahmed, S. Bandyopadhyay, **Ratnadwip Singha**, and Prabhat Mandal, *Journal of Applied Physics* **2017**, 121, 094103.

9. "Magneto-transport properties of proposed triply degenerate topological semimetal $Pd_3Bi_2S_2$", Shubhankar Roy, Arnab Pariari, **Ratnadwip Singha**, Biswarup Satpati, and Prabhat Mandal, *Applied Physics Letters* **2018**, 112, 162402.

10. "Anisotropic transverse magnetoresistance and Fermi surface in $TaSb_2$", Arnab Pariari, **Ratnadwip Singha**, Shubhankar Roy, Biswarup Satpati, and Prabhat Mandal, *Scientific Reports* **2018**, 8, 10527.

11. "Magnetotransport properties and giant anomalous Hall angle in the half-Heusler compound TbPtBi", **Ratnadwip Singha**, Shubhankar Roy, Arnab Pariari, Biswarup Satpati, and Prabhat Mandal, *Physical Review B* **2019**, 99, 035110.

12. "Effect of hydrostatic pressure on ferromagnetism in two-dimensional CrI_3", Suchanda Mondal, Murugesan Kannan, Moumita Das, Linganan Govindaraj, **Ratnadwip Singha**, Biswarup Satpati, Sonachalam Arumugam and Prabhat Mandal, *Physical Review B (Rapid Communication)* **2019**, 99, 180407(R).

13. "Magnetotransport properties of the correlated topological nodal-line semimetal YbCdGe", Antu Laha, Sudip Malick, **Ratnadwip Singha**, Prabhat Mandal, P. Rambabu, V. Kanchana, and Z. Hossain, *Physical Review B (Rapid Communication)* **2019**, 99, 241102(R).

14. "Complex exchange mechanism driven ferromagnetism in half-metallic Heusler Co_2TiGe: Evidence from critical behavior", Shubhankar Roy, Nazir Khan, **Ratnadwip Singha**, Arnab Pariari, and Prabhat Mandal, *Physical Review B* **2019**, 99, 214414.

B. Communicated

1. "Tip-induced superconductivity coexisting with preserved topological properties in line-nodal semimetal ZrSiS", Leena Aggarwal, Chandan K. Singh, Mohammad Aslam, **Ratnadwip Singha**, Arnab Pariari, Sirshendu Gayen, Mukul Kabir, Prabhat Mandal, and Goutam Sheet, *arXiv:1802.07993*.

2. "Fascinating interplay between Charge Density Wave Order and magnetic field in Non-magnetic Rare-Earth Tritelluride $LaTe_3$", Arnab Pariari, Sudipta Koley, Shubhankar Roy, **Ratnadwip Singha**, Mukul S. Laad, A. Taraphder, and Prabhat Mandal, *arXiv:1901.08267*.

C. Conference papers/presentations

1. "Single crystal growth and magnetotransport properties of new topological Dirac semimetal ZrSiS", **Ratnadwip Singha**, Arnab Kumar Pariari, Biswarup Satpati, and Prabhat Mandal, presented at **Condensed Matter Days (CMDAYS) - 2017**.

2. "Fermi surface properties of $NbAs_2$ studied by de Haas-van Alphen oscillation", **Ratnadwip Singha**, and Prabhat Mandal, *AIP Conference Proceedings* **2018**, 1942, 110017, presented at **DAE Solid State Physics Symposium (SSPS) - 2017**.

3. "Probing the large magnetoresistance and non-degenerate Dirac nodes in Zr-

SiS", **Ratnadwip Singha**, Arnab Kumar Pariari, Biswarup Satpati, and Prabhat Mandal, **Young Physicists Colloquium (YPC) - 2018** (organized by Indian Physical Society).

4. "Probing lattice dynamics and electron-phonon coupling in topological nodal-line semimetal ZrSiS", **Ratnadwip Singha**, Sudeshna Samanta, Swastika Chatterjee, Arnab Pariari, Dipanwita Majumdar, Biswarup Satpati, Lin Wang, Achintya Singha, and Prabhat Mandal, presented at **International conference on complex and functional materials (ICCFM) - 2018**.

Ratnadwip Singha

Ratnadwip Singha

Contents

SYNOPSIS

Introduction: The emergence of topological materials in condensed matter physics has introduced a completely new perspective in which the materials are characterized in terms of the topology of their electronic band structure and the physics is dictated by the inherent symmetries of the system. These materials are the subject of extensive theoretical and experimental studies and continue to reveal new exotic phases of matter. While the discovery of topological insulators (TIs) marks the beginning of this field [1, 2], subsequent realizations of Dirac, Weyl, and nodal line semimetals [3, 4, 5, 6, 7] have further enriched this field of research. Conducting surface and insulating bulk states are the distinctive features of TIs, whereas the bulk conduction band and valence band cross at either fourfold/twofold-degenerate discrete points (Dirac/Weyl points) or along an one-dimensional line (the nodal line) in topological semimetals (TSMs). In the vicinity of these band crossings, the dynamics of the quasiparticle excitations is described by the relativistic equations of motion. Apart from the opportunity to explore the novel physics of relativistic particles, topological systems have also caught researchers' attention due to their unique transport properties [8, 9, 10], which can have a huge impact on technological applications [11, 12]. In the thesis work, our goal is twofold. Firstly, experimentally confirm the novel topological quantum states in new materials and try to understand the crystallographic symmetries, which protect such band structure. Secondly, we have analyzed the electronic transport properties in these systems to reveal the exciting features, relevant for fundamental physics as well as technological applications. To explain these phenomena, particular emphasis has been given on the Fermi surface properties, which govern the scattering mechanisms in a material.

Experimental details: The materials studied in this thesis were grown in single crystalline form using either chemical vapor transport or flux growth technique. The as-grown single crystals were characterized using x-ray diffraction and high-resolution transmission electron microscopy. The transport measurements were performed in a cryogen-free measurement system (CFMS, Cryogenic Ltd.) and a physical property measurement system (PPMS, Quantum Design) via four-probe method. The dc magnetization measurements were done in a SQUID-VSM (MPMS3, Quantum Design). Raman spectroscopy measurements were performed in a LABRAM HR 800 system coupled to a liquid nitrogen cryostat and an in-Via Renishaw Raman spectrometer. We put the sample under pressure using a diamond-anvil-cell.

Large nonsaturating magnetoresistance and signature of non-degenerate Dirac nodes in ZrSiS: First-principle calculations [13] and angle-resolved photo emission spectroscopy (ARPES) measurement [14] have revealed the existence of multiple Dirac crossings along with unconventional hybridization of surface and bulk states in ZrSiS, which represents a large family of compounds (WHM with W=Zr, Hf, La; H=Si, Ge, Sn; M=O, S, Se, Te) with identical band topology. This material also hosts the highest reported energy range ($\sim$2 eV) of linearly dispersing bands, making it a sturdy topological system, which can be used for industrial applications. In this work, we have presented the magnetotransport properties of single crystalline ZrSiS. As shown in Figure 1(a), ZrSiS shows very large and non-saturating transverse magneoresistance (MR) $\sim 1.4\times10^5$ % at 2 K and 9 T magnetic field with the field applied along crystallographic c-axis. Interestingly, the MR is highly anisotropic, which is a signature of the quasi two-dimensional nature of the Fermi surface. With magnetic field applied parallel to b-axis and

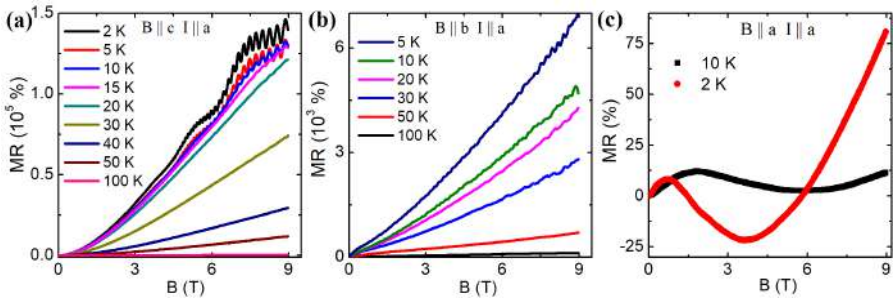

Figure 1: Transverse magnetoresistance in ZrSiS with current along a-axis and magnetic field parallel to (a) c-axis and (b) b-axis, measured at different temperatures, up to 9 T. (c) Longitudinal magnetoresistance with current and field along a-axis.

keeping the current direction unchanged, the MR at 9 T has been seen to reduce to ∼7000 % at 5 K [Figure 1(b)]. On the other hand, with parallel electric and magnetic field, ZrSiS shows negative MR [Figure 1(c)] originated from Adler-Bell-Jackiw (ABJ) chiral anomaly, a long-sought relativistic phenomenon of massless Dirac fermions [15, 16]. It is clear from Figure 1(a) that the resistivity (ρ) shows Shubnikov-de Haas (SdH) oscillations with two distinct frequencies. By analyzing the quantum oscillation, we have calculated several Fermi surface related parameters, including the Fermi surface cross-sections, Fermi momentum, and effective mass of the charge carriers. From the oscillation data, we have confirmed the non-trivial Berry phase and hence the Dirac fermionic nature of the charge carriers. Hall resistivity measurements reveal the presence of both electron and hole-type carriers with very large mobility. By combing the quantum oscillation and Hall effect results, we show that ZrSiS hosts multiple Dirac nodes at different energy values, which is in accordance to the band structure calculations [13].

Probing lattice dynamics and electron-phonon coupling in the topological nodal-line semimetal ZrSiS: It is well established that the structural symmetries play a key role in protecting the accidental degeneracies and non-trivial

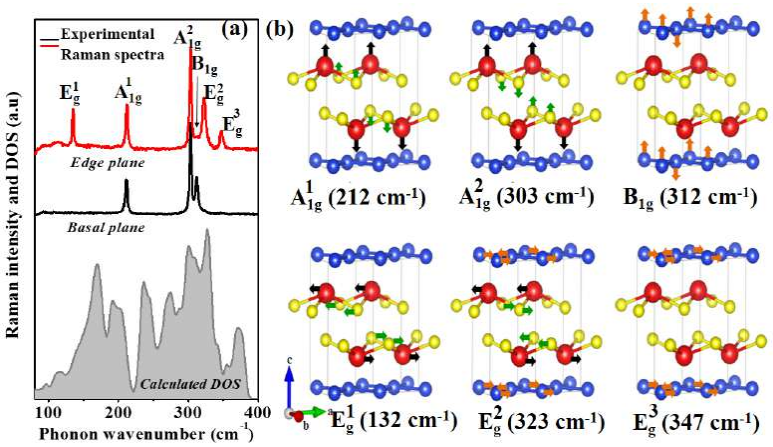

Figure 2: (a) Room temperature Raman spectra for *basal plane* (black curve) and *edge plane* (red curve) configurations. The shaded region in the lower panel represents the calculated phonon density of states for ZrSiS. (b) Vibration patterns corresponding to the Raman active modes.

topological electronic bands in a material. In ZrSiS, the square Si atom sublattice essentially controls the topological properties [14]. Therefore, a systematic study on the phonon subsystem can shed some light in understanding the topological nodal-line phase in this family of materials. We have investigated the lattice dynamics and electron-phonon interaction in ZrSiS using Raman spectroscopy. In Figure 2(a), the results of Raman measurements at room temperature for two different configurations of the ZrSiS crystal are presented along with the calculated phonon density of states (PDOS), shown by the filled area. The Raman modes have been identified from theoretically calculated atomic vibrational patterns [Figure 2(b)] along with phonon dispersion spectra. The polarization and crystal-angle-resolved Raman measurement results have been analyzed using crystal symmetries. Wavelength and temperature-dependent measurements show the complex interplay of electron and phonon degrees of freedom, resulting in resonant phonon and quasielastic electron scattering through interband transition. The high-pressure Raman studies reveal vibrational anomalies, which are the signature

of structural phase transitions. From high-pressure synchrotron x-ray diffraction measurements, we have observed pressure-induced structural transitions and co-existence of multiple phases, which also indicate possible electronic topological transitions in ZrSiS.

Magnetotransport properties and evidence of topological insulating state in LaSbTe: The single layer of the members of *WHM* family, is an ideal candidate to realize a two-dimensional TI with global band gap, which is induced by spin-orbit coupling (SOC) [13]. We have presented the magnetotransport and magnetization properties of LaSbTe, a member of the *WHM* family. This compound shows magnetic-field-induced turn-on behavior and low-temperature resistivity plateau. By adopting both metal-semiconductor crossover and Kohler scaling analysis, we have discussed the possible origin of the temperature and magnetic field dependence of resistivity. At 5 K and 9 T, a large, nonsaturating transverse MR $\sim 4\times10^3$ % has been obtained. The nonlinear field dependence of the Hall resistivity confirms the presence of two types of charge carriers. From the semiclassical two-band fitting of Hall conductivity and longitudinal conductivity, very high carrier mobilities and almost equal electron and hole densities are deduced, which result in large MR. We have observed prominent de Haas-van Alphen (dHvA) oscillation in the magnetization measurements. By direction dependent measurements, the oscillation has been confirmed to be generated from bulk Fermi pocket and analyzed to calculate the Fermi surface properties. Furthermore, the Landau level index plot from dHvA oscillation confirms a trivial bulk band structure. Figure 3(a) shows the electron-spin texture of the surface state in a TI; right handed spin texture for upper surface and left handed spin texture for lower surface. As a consequence of opposite spin helicity for the upper and lower Dirac cones, the electronic states

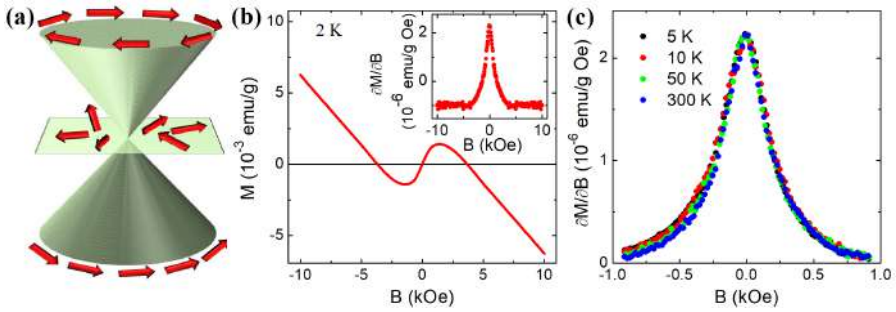

Figure 3: (a) Schematic representing the spin-texture of the surface state in a 3D topological insulator. The arrows indicate the direction of the electron spins. (b) Low field region of the magnetization data at 2 K for LaSbTe. Insets shows the corresponding magnetic susceptibility χ ($=\partial M/\partial B$). (c) Magnetic susceptibility at different temperatures, indicating the robustness of the signal.

close to the Dirac point face singularity in their spin orientation, provided the Dirac spectrum is not gapped. This small number of electrons does not have any preferable spin alignment but the spins are randomly oriented. An external magnetic field can align the spins along its direction. As a result, a paramagnetic contribution is observed in the total magnetic moment [17]. The corresponding magnetic susceptibility shows a cusp in the $\chi(B)$ plot. In Figure 3(b), the low-field region of the magnetization curve is shown for LaSbTe, at a representative temperature 2 K. Although, diamagnetic behavior is observed at higher field, a clear paramagnetic signal appears in the low-filed region. The susceptibility (shown in the inset) exhibits a cusp at $B = 0$, as expected for a TI [17]. As shown in Figure 3(c), the susceptibility cusp exists even at room temperature and the peak height along with its sharpness are independent of the temperature. The observed paramagnetic singularity originates from the non-trivial surface bands near the band crossing points and confirms that LaSbTe is a topological insulator, consistent with the earlier first-principles calculations.

Fermi surface topology and signature of surface Dirac nodes in LaBi: Ex-

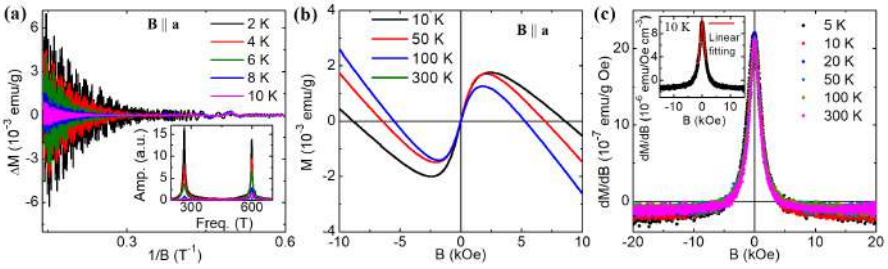

Figure 4: (a) de Haas-van Alphen oscillation obtained after background subtraction for LaBi. Inset shows the corresponding fast Fourier transform result. (b) Low field region of the magnetic moment vs. B curves at different temperatures. (c) Magnetic susceptibility χ $(= dM/dB)$, calculated by taking first order derivative of magnetic moment, plotted as a function of magnetic field. Inset shows the linear field decay of χ.

treme MR and ultrahigh carrier mobility are two major hallmarks of topological materials and often used as primary criteria for identifying new compounds belonging to this class. While LaBi exhibits these properties, the topological nature of its band structure remains unresolved. From theoretical calculations [18], the members of the family of rare earth monopnictides LaX (X=N, P, As, Sb, Bi) have been predicted to be potential candidates for either topological semimetal (TSM) or TI. Contradicting reports exist in literature claiming both trivial and non-trivial topological states in LaSb [19, 20], whereas ARPES studies have demonstrated multiple Dirac nodes at the surface of LaBi [21, 22]. Furthermore, in several earlier studies on LaBi, the number of Fermi pockets reported from the SdH oscillation do not converge [23, 24]. This discrepancy in reported results may be the inherent problem of this technique. Using the magnetotransport and magnetization measurements, we have probed the bulk and surface states of LaBi. Extremely large MR and high carrier mobility have been observed with compensated electron and hole density. The Fermi surface properties have been analyzed from both SdH and dHvA oscillation techniques. In Figure 4(a), we have plotted the oscillatory com-

ponent (ΔM) of the magnetization data after subtracting a smooth background. In the inset, the fast Fourier transform (FFT) spectrum is shown, which clearly reveals two oscillation frequencies. From the quantum oscillation data, we have determined the Fermi surface related parameters and non-trivial Berry phase for both Fermi pockets. As shown in Figure 4(b), the magnetization data for LaBi predominantly demonstrate diamagnetic behavior throughout the measured field range, a clear paramagnetic contribution is observed in the vicinity of zero field. In Figure 4(c), the corresponding susceptibility plots are shown at different representative temperatures. As predicted theoretically for TIs [17], robust cusps have been observed at B=0, which persist up to room temperature. Therefore, LaBi certainly hosts topological Dirac fermions at the surface state, which is in accordance with the ARPES reports [21, 22]. Thus, our study unambiguously confirms that LaBi is a three-dimensional topological insulator with possible linear dispersion in the gapped bulk band structure.

Probing the Fermi surface and magnetotransport properties of $MoAs_2$: The family of transition metal dipnictides (TMDs) [XPn_2 (X = Ta, Nb; Pn = P, As, Sb)], has been theoretically proposed as ideal candidates for investigating the topology protected electronic systems [25]. These materials possess identical electronic band structure and host multiple band anticrossings near the Fermi level. In absence of SOC, these anticrossings form a nodal-line in the $\boldsymbol{k}$-space. However, with the inclusion of SOC, the nodal line is gapped out, leading to only isolated electron and hole pockets. The unusual magnetotransport properties in TMSs are often attributed to the compensated electron-hole density rather than any non-trivial band topology [26, 27, 28]. We have investigated the magnetotransport and Fermi surface properties of $MoAs_2$, another member of this group

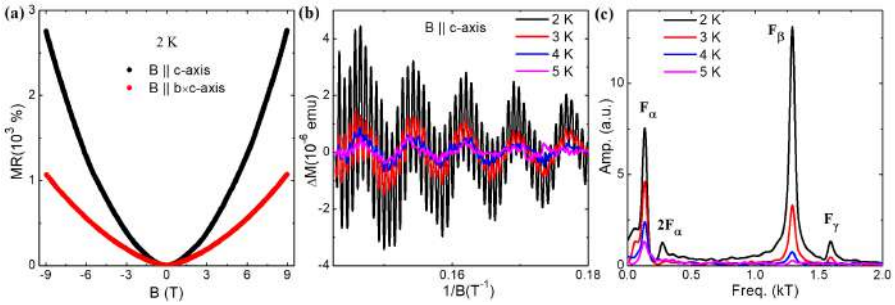

Figure 5: (a) Transverse magnetoresistance of $MoAs_2$ at 2 K, when current is along b-axis and magnetic filed is applied along two mutually perpendicular crystallographic directions, c-axis and $b\times c$-axis. (b) The dHvA oscillation in the magnetization measurement for magnetic field along c-axis at different representative temperatures. (c) The FFT spectra of the dHvA oscillation.

of compounds. Similar to several TSMs, field-induced metal-semiconductor-like crossover and resistivity plateau have been observed. As shown in Figure 5(a), $MoAs_2$ shows large, non-saturating MR, which is highly anisotropic in nature. By performing directional dependent measurements, we have observed a butterfly-like angle dependence. From the Hall resistivity, we found that in contrast to other isostructural materials, the carrier density in $MoAs_2$ is quite high and shows single-band-dominated transport. A prominent dHvA oscillation has been observed, which is plotted in Figure 5(b) after background subtraction. The corresponding FFT spectra in Figure 5(c) show that the Fermi pockets are the largest among the members of this group. By analyzing the dHvA oscillation along three mutually perpendicular directions, we confirm that the Fermi pockets are anisotropic in nature. Our first-principles calculations reveal a substantial difference between the band structures of $MoAs_2$ and that of other TMDs. The calculated Fermi surface consists of one electron pocket and another 'open-orbit' hole pocket, which has not been observed in TMDs so far and likely to be the origin of large MR in $MoAs_2$.

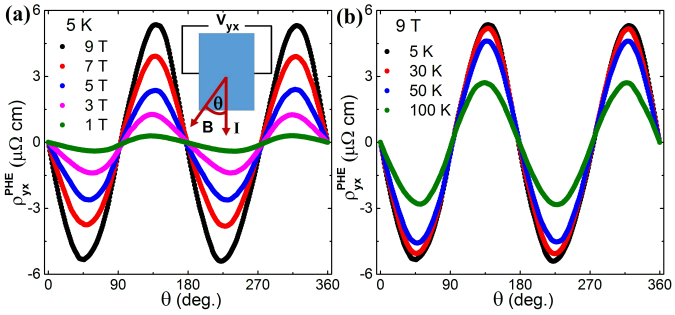

Figure 6: (a) Angle dependence of the planar Hall resistivity (ρ_{yx}^{PHE}) at 5 K for different magnetic field strength. Inset shows the schematic for experimental set-up. (b) Angle dependence of ρ_{yx}^{PHE} at 9 T for different temperatures.

Planar Hall effect in type II Dirac semimetal VAl_3: Type II TSMs host the Lorentz-violating Dirac and Weyl fermions, which are impossible to realize in relativistic particle physics. Although type II Weyl fermions have been probed in few systems [29, 30, 31], the candidates for type II Dirac semimetals are rather limited [32]. Recently, from band structure calculations, the members of the family MA_3 (M=V, Nb, Ta; A=Al, Ga, In) are proposed to be type II Dirac semimetals [33]. The ABJ chiral anomaly is widely regarded as a direct evidence of the Dirac/Weyl cones in the band structure. However, this effect can be easily suppressed by small misalignment between electric and magnetic field. Moreover, other mechanisms such as current jetting, weak localization can also produce negative longitudinal MR (LMR). Therefore, it is very difficult to distinguish the negative MR induced by chiral anomaly from others. From theoretical calculations, recently, a planar Hall effect (PHE) has been predicted in TSMs, which originates from the ABJ chiral anomaly and non-trivial Berry curvature [34, 35]. As PHE is completely different from usual Hall effect, both in experimental configuration and angle dependence, this phenomenon is easier to identify and unambiguously confirms the

Dirac/Weyl type excitations in the system. We present a detailed analysis on the magnetotransport properties of VAl_3. A large, nonsaturating MR has been observed. Hall resistivity reveals the presence of two types of charge carriers with high mobility. As shown in Figures 6(a) and (b), our measurements show a large PHE in this material, which is robust and can be easily detectable up to high temperature. This phenomenon validates the theoretical prediction of the Dirac semimetal phase in VAl_3.

Bibliography

[1] M. Z. Hasan *et al.*, Rev. Mod. Phys. **82**, 3045 (2010).

[2] X.-L. Qi *et al.*, Rev. Mod. Phys. **83**, 1057 (2011).

[3] Z. K. Liu *et al.*, Nat. Mater. **13**, 677 (2014).

[4] Z. K. Liu *et al.*, Science **343**, 864 (2014).

[5] B. Q. Lv *et al.*, Nat. Phys. **11**, 724 (2015).

[6] S.-Y. Xu *et al.*, Science **349**, 613 (2015).

[7] G. Bian *et al.*, Nat. Commun. **7**, 10556 (2016).

[8] M. N. Ali *et al.*, Nature **514**, 205 (2014).

[9] T. Liang *et al.*, Nat. Mater. **14**, 280 (2015).

[10] C. Shekhar *et al.*, Nat. Phys. **11**, 645 (2015).

[11] S. A. Wolf *et al.*, Science **294**, 1488 (2001).

[12] J. E. Lenz, Proc. IEEE **78**, 973 (1990).

[13] Q. Xu *et al.*, Phys. Rev. B **92**, 205310 (2015).

[14] L. M. Schoop *et al.*, Nat. Commun. **7**, 11696 (2016).

[15] S. Adler, Phys. Rev. **177**, 2426 (1969).

[16] J. S. Bell *et al.*, Il Nuovo Cimento A. **60**, 47 (1969).

[17] L. Zhao *et al.*, Nat. Mater. **13**, 580 (2014).

[18] M. Zeng *et al.*, arxiv:1504.03492v1 (2015).

[19] L.-K. Zeng *et al.* Phys. Rev. Lett. **117**, 127204 (2016).

[20] X. H. Niu *et al.* Phys. Rev. B **94**, 165163 (2016).

[21] J. Nayak *et al.* Nat. Commun. **8**, 13942 (2017).

[22] R. Lou *et al.*, Phys. Rev. B **95**, 115140 (2017).

[23] S. Sun *et al.*, New J. Phys. **18**, 082002 (2016).

[24] F. F. Tafti *et al.*, Proc. Natl. Acad. Sci. USA **113**, E3475 (2016).

[25] C. Xu *et al.*, Phys. Rev. B **93**, 195106 (2016).

[26] K. Wang *et al.*, Sci. Rep. **4**, 7328 (2014).

[27] Y.-Y. Wang *et al.*, Phys. Rev. B **94**, 041103(R) (2016).

[28] B. Shen *et al.*, Phys. Rev. B **93**, 195119 (2016).

[29] A. A. Soluyanov *et al.*, Nature **527**, 495 (2015).

[30] K. Deng *et al.*, Nat. Phy. **12**, 1105 (2016).

[31] K. Koepernik *et al.*, Phys. Rev. B **93**, 201101(R) (2016).

[32] M. Yan *et al.*, Nat. Commun. **8**, 257 (2017).

[33] T-R. Chang *et al.*, Phys. Rev. Lett. **119**, 026404 (2017).

[34] A. A. Burkov, Phys. Rev. B **96**, 041110(R) (2017).

[35] S. Nandy *et al.*, Phys. Rev. Lett. **119**, 176804 (2017).

List of Figures

List of Tables

1

Introduction

In this chapter, we have revisited the theoretical and experimental developments that lead to the present understanding of the topological band theory. These discoveries span over decades and each of them proved to be a massive stepping stone in condensed matter physics. We start with the concept of band theory of solids, which essentially shapes our idea of material properties. This is followed by the observation of integer quantum Hall effect and the introduction of topological order in real systems. Subsequently, we have described the intriguing features of quantum Hall insulator, three-dimensional topological insulators and semimetals in chronological order. Finally, we have discussed how these works motivated us to explore such novel quantum phases of matter and summarized the major findings of this thesis.

1.1 Band theory

The band theory of solids is one of the fundamental concepts in condensed matter physics and provides us a tool to classify different states of matter. The development of this theory is rooted into the quantized energy levels of electrons in a single atom. In a solid, however, a large number of atoms are arranged in periodic structure. The motion of the electrons is then not dictated by the individual atom, but all the neighboring atoms combined. As a result, instead of discrete levels, the energy states of electrons form continuous bands, separated by an energy gap (E_g). The electronic motion is described by Bloch Hamiltonian $H_m(\boldsymbol{k})$ and Bloch wave function $|u_m(\boldsymbol{k})>$, where $\boldsymbol{k}$ is the crystal momentum. The outermost completely electron filled band is called valence band, whereas the next partially occupied or completely empty band is the conduction band. As the name suggests, only the electrons from the conduction band are responsible for the charge conduction in a solid. Adopting this simplified picture, we can put different materials in few groups as shown in the Figure 1.1. For example, in insulators, the empty conduction band is separated from the valence band by a large energy gap. Therefore, in order to have a charge flow, one needs to excite some electrons from valence to conduction band. As E_g is too large to overcome at room temperature, insulators can not conduct current. On the other hand, conduction and valence bands overlap in metals, providing ample conducting electrons. Semiconductors belong in between, with small enough band gap ($E_g \lesssim 1$ eV), so that significant number of electrons can reach the conduction band at finite temperature. Similar to metals, semimetals can also conduct current. But, in this case, these two bands just touch each other and contribute only a small number of electrons in conduction band.

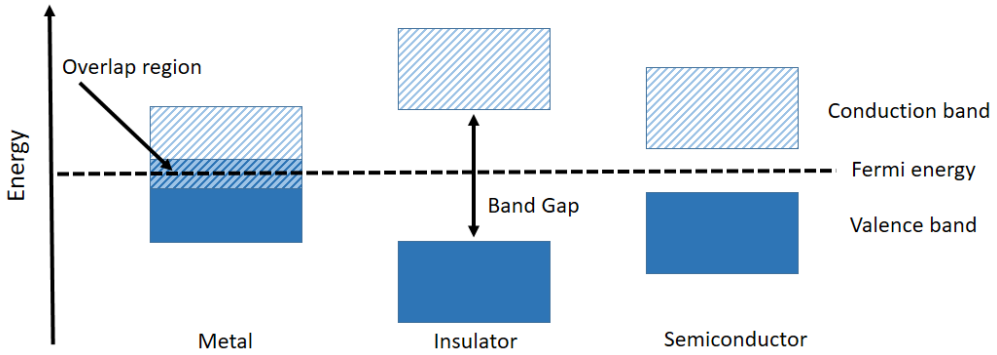

Figure 1.1: Classification of crystalline solids according to band theory.

For decades, band theory proved to be extremely successful and remained the sole mechanism needed to explain the physical properties of crystalline solids. However, the whole scenario changed drastically with the discovery of integer quantum Hall effect, which demanded a completely new perspective.

1.2 Integer quantum Hall effect

K. von Klitzing, G. Dorda and M. Pepper, in 1980, discovered the integer quantum Hall effect (IQHE) [1]. This phenomenon appears in two-dimensional (2D) electron gas, when put under a strong magnetic field. The Hall conductivity (σ_{xy}) is observed to be highly quantized (accurate down to 1 part in billion) and insensitive to the geometry of the electron gas [1, 2]. As shown in Figure 1.2, IQHE can be explained semiclassically. Under applied magnetic field, electrons move in cyclotron orbits with their energy quantized as $\epsilon_m = \hbar\omega_c(m+1/2)$, where ω_c is the cyclotron frequency and m is an integer. These discrete energy levels, called Landau levels, have degeneracy directly proportional to the magnetic field strength. Therefore, with increasing magnetic field, each Landau level can accommodate more electrons. To minimize the energy, electrons are then forced to move from

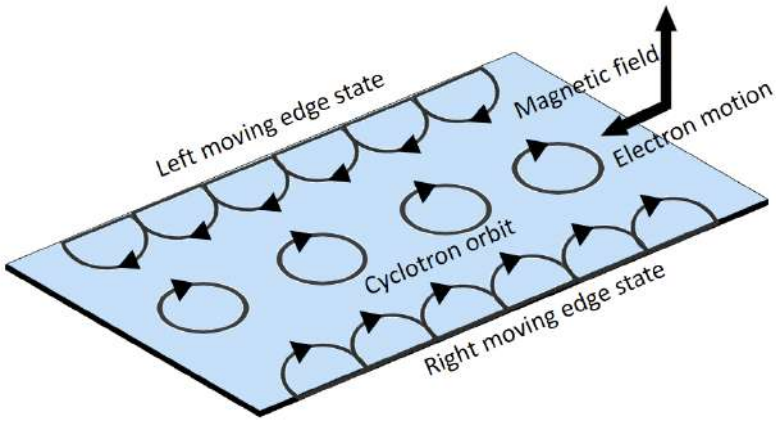

Figure 1.2: Semiclassical description of integer quantum Hall state.

higher to lower Landau level. If electrons occupy up to N^{th} Landau level, while the rest are empty, we observe a Hall conductivity,

$$\sigma_{xy} = Ne^2/h. \tag{1.1}$$

In this configuration, Landau levels can be treated to be the energy bands as in band theory. So, with filled N^{th} Landau level separated from the empty $(N+1)^{th}$ level by a constant energy gap $\hbar\omega_c$, integer quantum Hall state (IQHS) should behave like an ordinary insulator. Unlike an insulator, IQHS shows quantized Hall conductivity under an electric field. Another striking feature of IQHS is the presence of conducting edge states. They appear at the boundary of the 2D electron gas due to the skipping motion of electrons as their cyclotron orbits bounce off the edge. These states are called 'chiral' as they propagate to only one direction without backscattering irrespective of any disorder in the system. IQHE does not fit in the description of the conventional band theory of solids and paved the pathway to introduce the topological order in condensed matter physics.

1.3 Topology in geometry

Topology is a mathematical formalism used to categorize different geometrical objects [3]. In this framework, two objects belong to the same topological class, provided that we can get to one of them by continuously deforming the other, i.e., by stretching or bending but not tearing or gluing. For example, a solid sphere can be turned into a disc by compressing along a diagonal axis. However, from topological perspective, they are not distinct. But if we poke a hole to make an annular shape, it is no longer a member of this group. In fact, counting the number of holes in objects to classify them, is one of the basic idea in topology. To construct more formal definition, we use the value of genus (g) given by the Gauss-Bonnet theorem,

$$\int_{surface} K dS = 4\pi(1-g), \tag{1.2}$$

where K is the Gaussian curvature. For a sphere with radius r, $K = \frac{1}{r^2}$ and Equation 1.2 leads to $g = 0$. In Figure 1.3, we have shown objects with different values of genus (same as the number of holes), representing different topological classes.

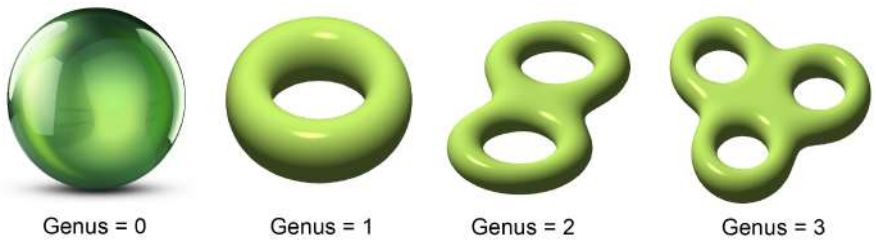

Figure 1.3: Geometrical objects representing different topological classes and identified by the values of genus.

1.4 Topology in band theory

Similar to geometry, the idea of topology can be used in band theory to classify different electronic states [4, 5]. By smoothly varying the Bloch Hamiltonian $H_m(\boldsymbol{k})$, one can tune the energy gap between the conduction and valence bands in a system. As long as these two bands do not touch each other, i.e., the band gap is finite, the material remains in same topological class. Therefore, an ordinary insulator and semiconductor are both topologically equivalent to vacuum, which has a band gap $\sim 10^6$ eV (for pair production). In band theory, however, instead of genus, we have a new topological invariant called Chern invariant (n_m). n_m is insensitive to smooth variation of $H_m(\boldsymbol{k})$, but changes when we go to a different topological class. Chern invariant can be mathematically formulated from the Berry phase associated with the Bloch wave function $|u_m(\boldsymbol{k})>$. Berry phase is given by the line integral of $A_m = i < u_m|\nabla_k|u_m >$ around a closed path. The Berry connection (A_m) is analogous to an electromagnetic vector potential. Hence, one can introduce a Berry flux $F_m = \nabla_k \times A_m$. Chern invariant is defined as the total Berry flux in the Brillouin zone,

$$n_m = \frac{1}{2\pi} \int F_m d^2k. \tag{1.3}$$

1.5 The concept of topology in integer quantum Hall effect

D. J. Thouless, M. Kohmoto, M. P. Nightingale, and M. den Nijs, in 1982, adopted the idea of Berry connection to derive the Hall conductivity in IQHE [6]. Using

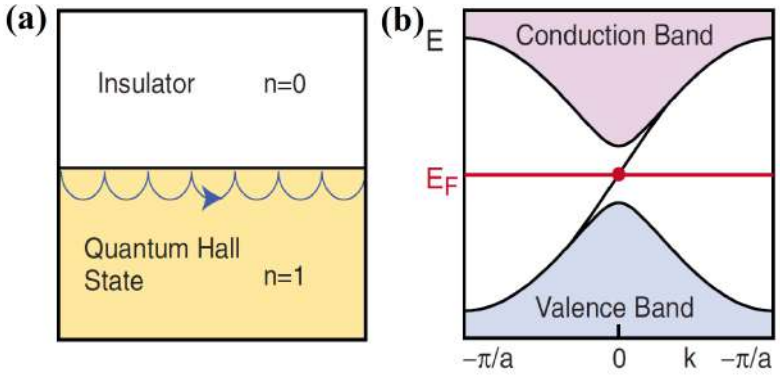

Figure 1.4: (a) Appearance of chiral edge state at the interface of trivial insulator (vacuum) and quantum Hall state. (b) The edge state is represented by an one-dimensional band dispersion, which connects the conduction and valence band. Reproduced from Ref. [4].

Kubo formula, they found the relation,

$$\sigma_{xy} = ne^2/h, \tag{1.4}$$

where n is an integer called total Chern number or TKNN invariant, which is the Chern invariant summed over all occupied bands ($n = \sum_{m=1}^{N} n_m$). This relation is identical to Equation 1.1 and explains the robust quantization of the Hall conductivity [4]. As n is a topological invariant, σ_{xy} changes only when we go to a new topological class. For a trivial insulator (such as vacuum) $n = 0$, whereas IQHS is represented by $n = 1$. Therefore, one can not obtain an IQHS from a trivial insulator by smoothly varying the Hamiltonian. At some point, the band gap has to close, i.e., pass through zero to change the topological invariant. At this interface of trivial insulator (vacuum) and IQHS, the conducting chiral edge state appears as shown in Figure 1.4(a) [4]. The edge state is protected by the fundamental concept of topology and gives rise to an one-dimensional (1D) band dispersion in the bulk band gap [Figure 1.4(b)] [4]. By changing the Hamiltonian

near the surface, we can modify the dispersion of this 1D band. However, the difference between the number of left and right moving channels (band dispersions that intersect Fermi level with positive or negative group velocity) is fixed and determined by the 'bulk-boundary correspondence' [4].

1.6 Quantum spin Hall insulator

IQHE is the first experimentally observed topologically non-trivial electronic state. However, it only exists under magnetic field in absence of time reversal symmetry (TRS). This leads to a question, whether such states can be realized in a material without applying magnetic field. This issue was first addressed by F. D. M. Haldane in 1988 by constructing a 2D honeycomb lattice model [7]. Haldane model exhibits non-zero quantized Hall conductivity in absence of an external magnetic field, but still requires local magnetic fields pointing up and down at different lattice sites. Following the fundamental idea of this model, in 2006, B. A. Bernevig and S.-C. Zhang predicted that spin-orbit coupling (SOC) can play the role of the local magnetic field in a material [8]. Subsequently, they (B. A. Bernevig, T. L. Hughes, S.-C. Zhang) also predicted that such state can be observed in HgTe/CdTe quantum well [9], which was experimentally realized by L. W. Molenkamp and his collaborators in 2007 [10]. This is the first discovery of a 2D topological insulator (TI) or quantum spin Hall insulator (QSHI). As shown in Figure 1.5 (a), in a simplified picture, QSHI can be described as a superposition of two IQHSs with counter-propagating chiral edge channels [11]. Each edge channel is associated with one spin state, either spin-up or spin-down and propagates anti-clockwise or clockwise depending on the direction of the intrinsic magnetic field generated by the SOC. So, in QSHI, there is no net charge flow but spin-current persists at

the boundary. If we start with spin-up channel with charge conduction in anti-clockwise direction under magnetic field pointing upwards and perform the time reversal operation, we get the other state, i.e., both spin and magnetic field pointing downwards with clockwise charge conduction. So, these two states are time-reversal partner of each other. Therefore, the new state obtained by combining them, preserves the TRS. From band dispersion point of view, these edge states represent two 1D bands in the bulk band gap intersecting the Fermi energy, one with positive and another with negative group velocity [Figure 1.5(b)] [12]. These two bands merge at TRS invariant momenta $\boldsymbol{k} = 0$ and π/a (same as -π/a; a is the lattice parameter) [4]. In general, band crossing leads to hybridization and opening of gap at the crossing point. However, in this case, two bands can not hybridize as they are protected by the very nature of TRS operation. According to the Kramer's theorem, the band crossing points must be doubly degenerate under TRS. These edge states are very robust, insensitive to disorder and can not be removed unless we break the TRS. So, in a 2D TI, we observe an insulating bulk state along with conducting boundary. However, it is topologically distinct from both conventional insulator and IQHS, which requires external magnetic field, and is characterized by a new topological invariant ν, known as $\mathbb{Z}_2$ invariant [13]. ν can have values 0 or 1 for topologically trivial or non-trivial states, respectively. $\mathbb{Z}_2$ invariant can be mathematically expressed as,

$$(-1)^{\nu} = \prod_{i=1}^{4} \frac{Pf[\omega(\Gamma_i)]}{\sqrt{Det[\omega(\Gamma_i)]}}, \tag{1.5}$$

where Γ_i are the four high symmetry points in the 2D Brillouin zone, $\omega_{mn}(\boldsymbol{k})$ $= < u_m(\boldsymbol{k})|\Theta|u_n(-\boldsymbol{k}) >$ is a unitary matrix defined by the Bloch states and $Pf[\omega(\Gamma_i)]$ is the Pfaffian, i.e., the square root of the determinant (Det) of the

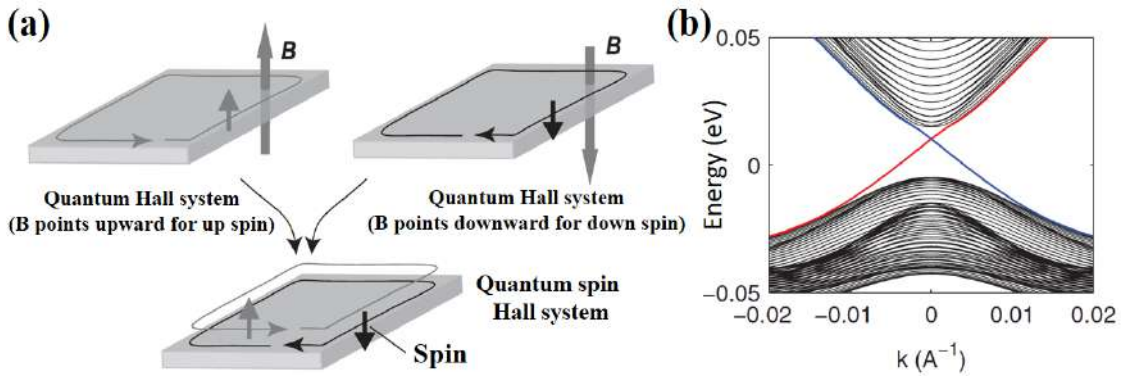

Figure 1.5: (a) A schematic representation of QSHI, which can be described as a superposition of two integer quantum Hall states with counter-propagating chiral edge channels. Reproduced from Ref. [11]. (b) Energy spectrum of QSHI, showing two one-dimensional bands due to the edge states. Reproduced from Ref. [12].

matrix $\omega(\Gamma_i)$. So, $\delta_i = \frac{Pf[\omega(\Gamma_i)]}{\sqrt{Det[\omega(\Gamma_i)]}} = \pm 1$. The antiunitary operator Θ represents the TRS operation, where Θ^2 = -1.

1.7 Three-dimensional topological insulator

In 2007, Liang Fu, C. L. Kane, and E. J. Mele showed that the concept of 2D TI can also be generalized to three-dimensions (3D) [14]. For 3D TI, however, instead of one, there are four $\mathbb{Z}_2$ topological invariants (ν_0; ν_1, ν_2, ν_3) [14, 15, 16]. ν_0 is defined by extending Equation 1.5 to eight high symmetry points in 3D Brillouin zone,

$$(-1)^{\nu_0} = \prod_{i=1}^{8} \delta_i. \tag{1.6}$$

The other three invariants are given by the product of δ_i's, for which Γ_i reside in the same plane. For trivial insulator, (ν_0; ν_1, ν_2, ν_3) = (0; 0, 0, 0).

1.7.1 Weak topological insulator

One of the simplest ways to construct a 3D TI is to stack layers of 2D TIs with weak interlayer coupling along one axis [4]. The 1D edge states of the layers then combine to form the 2D conducting surface state. This surface state is not protected by TRS and can be removed by introducing strong disorder. Such structure is called weak TI and represented by $\nu_0 = 0$ and at least one of the other three invariants is 1 [14, 15]. However, in 2012, Z. Ringel *et al.* showed that the surface state along certain cleavage planes in weak TI, is indeed immune to random perturbation and preserve the TRS [17].

1.7.2 Strong topological insulator

A strong TI is characterized by $\nu_0 = 1$ and has insulating bulk coexisting with robust metallic 2D surface states along any cleavage plane [14, 15]. One of the unique features of this TRS protected surface state is 'spin-momentum locking', i.e., the spin of the charge carriers is always perpendicular to both its momentum and surface normal vector [4, 5]. Therefore, the carriers can not be backscattered by non-magnetic impurity, resulting in almost dissipationless charge conduction. Strong TI is further distinguished by odd number of TRS invariant Kramers degenerate points enclosed by surface Fermi energy contour [4, 5]. But most interestingly, the dynamics of the surface charge carriers are governed by a Dirac-type effective Hamiltonian [4, 5],

$$H_{Surface}(k_x, k_y) = \hbar v_F \hat{z} \times \vec{\sigma}.\vec{k}, \tag{1.7}$$

where $\bar{\sigma}$ is the Pauli spin vector. As a result, surface state in 3D TI is represented by linearly dispersing bands, which cross each other at Kramers degenerate Dirac

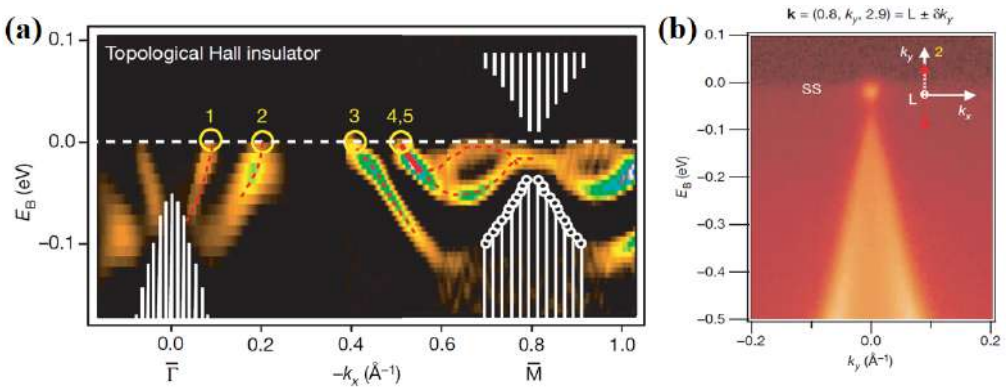

Figure 1.6: (a) The second-derivative ARPES image of the surface band in $Bi_{0.9}Sb_{0.1}$ along $\bar{\Gamma}$-$\bar{M}$. The white shaded area represents the bulk band projection. The yellow circles show the odd number of Fermi energy crossings of the surface state (SS). (b) Dirac-like dispersion of the SS near the L-point in the bulk Brillouin zone. Reproduced from Ref. [18].

points. This is in sharp contrast to the conventional electronic systems, where energy bands follow quadratic dispersion relation.

Following the theoretical prediction by L. Fu and C. L. Kane [15], the strong 3D TI state was first observed in $Bi_{1-x}Sb_x$ by M. Z. Hasan and his collaborators using angle-resolved photoemission spectroscopy (ARPES) [18]. Their experimental results have been shown in Figure 1.6 [18]. The linearly dispersing surface states have been clearly observed along with five surface band crossings. While the surface band structure of $Bi_{1-x}Sb_x$ is quite complicated, the bulk band structure has very small energy gap and hence some bulk carriers do contribute in electronic transport at room temperature. Later on, H. Zhang *et al.* have theoretically proposed a new series of compounds, Bi_2Se_3, Bi_2Te_3 and Sb_2Te_3, all with single Dirac node at surface and sufficiently large bulk band gap [Figure 1.7] [19]. Their predictions have been subsequently confirmed by various experimental groups [20, 21, 22].

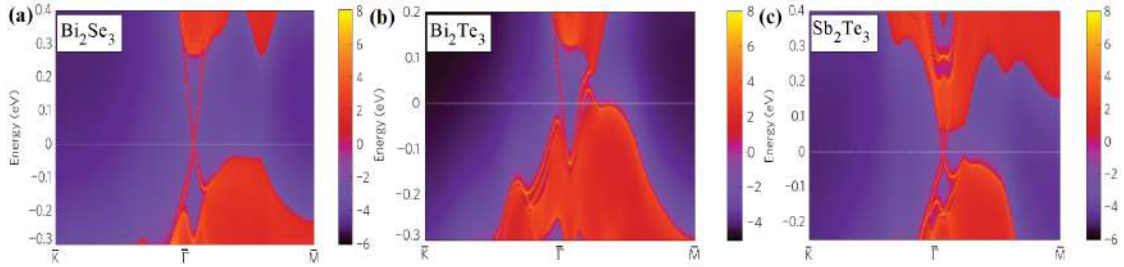

Figure 1.7: Energy and momentum dependence of the local density of states for (a) Bi_2Se_3, (b) Bi_2Te_3, and (c) Sb_2Te_3 on the [111] surface. The red and blue regions indicate bulk energy bands and bulk band gaps, respectively. The red lines, dispersing in the bulk gap around the Γ point, are the surface states. Reproduced from Ref. [19].

1.8 Three-dimensional topological semimetal

The surface electronic band structure of a 3D TI follows linear dispersion relation along two momentum directions and forms 2D Dirac cone similar to graphene. The discovery of Dirac fermions as low energy excitations in condensed matter systems is a breakthrough, which enables us to explore the dynamics of relativistic particles in table-top experiments. This has also encouraged the search for new materials, where such quasiparticles can be realized in 3D. In recent times, topological band theory has successfully led to a wide pool of fundamental particles, some of which can not be predicted from quantum field theory.

1.8.1 Topological Dirac semimetal

It has been theoretically proposed that a 3D Dirac cone can be realized at the critical point of phase transition from trivial to topological insulator in an inversion symmetric crystal [15]. Such phase transition can be induced by tuning the SOC or lattice parameters through chemical doping or external pressure. The mecha-

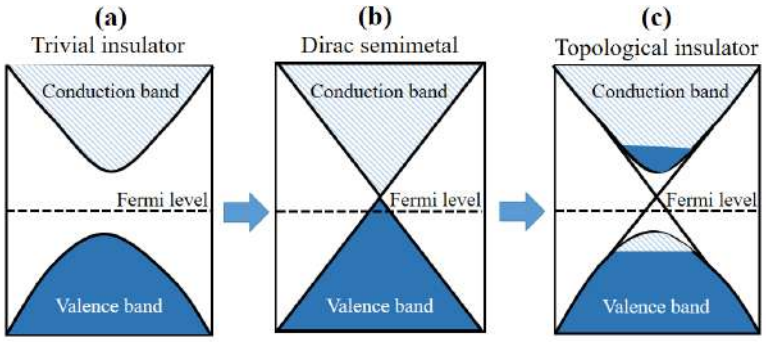

Figure 1.8: Schematic diagram illustrating the appearance of 3D Dirac cone at the critical point of phase transition from trivial to topological insulator due to band inversion.

nism has been explained schematically in Figure 1.8. In topological insulator, the bulk band structure undergoes band inversion, where the SOC opens a band gap. Starting from a trivial insulator, in order to have a band inversion, the bulk bands has to pass through a gapless state, where the conduction and valence bands touch at a single point forming a semimetallic bulk state. In the vicinity of this point (Dirac point), the electronic bands obey linear dispersion relation along all three momentum directions and the dynamics of the quasiparticles are described by a massless 3D Dirac-type Hamiltonian,

$$H = \hbar v_F \begin{bmatrix} \overrightarrow{\sigma}.\overrightarrow{k} & 0 \\ 0 & -\overrightarrow{\sigma}.\overrightarrow{k} \end{bmatrix}. \tag{1.8}$$

As Pauli spin matrices (σ_x, σ_y, and σ_z) are 2×2, this Hamiltonian has four components. 3D Dirac cone was first experimentally observed in $Bi_{1-x}Sb_x$ [18] and later in $BiTl(S_{1-\delta}Se_\delta)_2$ [23] by ARPES. As shown in Figure 1.9 [23], in $BiTl(S_{1-\delta}Se_\delta)_2$, upon increasing the Se concentration, the compound changes from direct to inverted indirect band gap system with gapless state appearing at $\delta = 0.6$. However, these materials have certain disadvantages. First of all, the Dirac cone only emerges

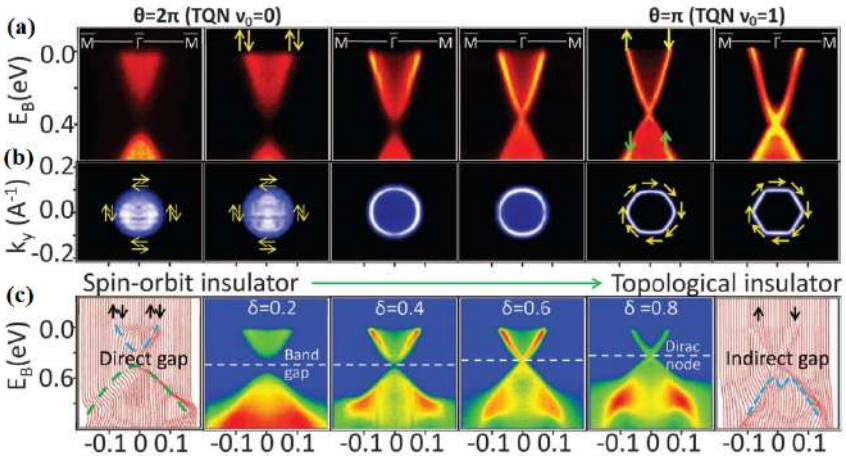

Figure 1.9: Topological phase transition in $BiTl(S_{1-\delta}Se_{\delta})_2$. (a) ARPES dispersion maps from (left panel) a spin-orbit band insulator to (right panel) a topological insulator. (b) ARPES-mapped native Fermi surfaces and their spin-texture for different chemical compositions (from left to right, $\delta = 0$ to $\delta = 1$). (c) Left and right panels: Energy distribution curves for compositions with $\delta = 0$ and $\delta = 1$, respectively. Center panels: ARPES spectra showing band gap and Dirac node for compositions $\delta = 0.2$ to $\delta = 0.8$. Reproduced from Ref. [23].

at a particular concentration of chemical doping. Therefore, this state is not robust against any possible impurity. Besides, it is almost impossible to experimentally control the doping concentration, while synthesizing the compounds.

These problems can be tackled by considering additional crystalline space group symmetries. New materials were theoretically proposed [24, 25, 26], where strong SOC leads to inversion of the conduction and valence bands. These two bands hybridize and open a band gap except at some special momentum points, where the band crossings are protected by crystalline symmetries. As both TRS and inversion symmetry (IS) are preserved in these materials, these crossing points are four-fold degenerate. The electronic bands in the vicinity follow linear dispersion relation and form 3D Dirac cones in the bulk state [24, 25, 26]. On the other hand, the surface state in topological Dirac semimetal (TDS) hosts spin-polarized Fermi arcs, connecting two surface projections of the bulk Dirac points [Figure 1.10]

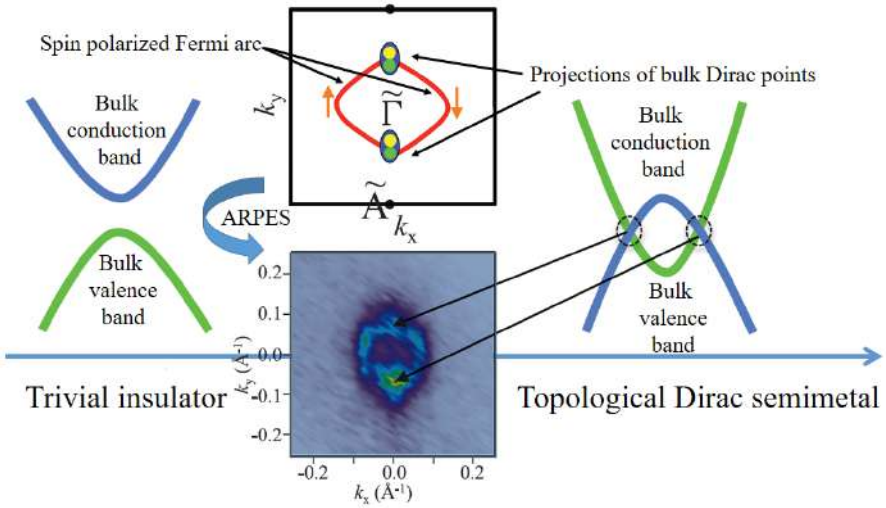

Figure 1.10: Schematic diagrams representing the bulk and surface states of a 3D topological Dirac semimetal. The lower center panel shows the ARPES data of the surface state of Na_3Bi. Reproduced from Ref. [27].

[27]. Unlike 3D TI, where spin projection perpendicular to momentum direction is constant along the closed Fermi contour, in TDS it gradually vanishes as we approach these points. Na_3Bi and Cd_3As_2 are two of the first predicted TDS candidates, where the bulk Dirac points are protected by C_3 and C_4 crystalline rotational symmetries, respectively [25, 26]. As shown in Figure 1.11, in 2014, the bulk Dirac cones in these compounds were experimentally observed by Z. K. Liu *et al.* [28, 29], whereas the surface Fermi arcs were later confirmed by S.-Y. Xu *et al.* [27] and H, Yi *et al.* [30]

1.8.2 Topological Weyl semimetal

In 1929, H. Weyl showed that for massless spin 1/2 particles, the four-component Dirac Hamiltonian (same as Equation 1.8 with v_F and k replaced by velocity of light c and momentum p, respectively) can be split into a couple of two-component

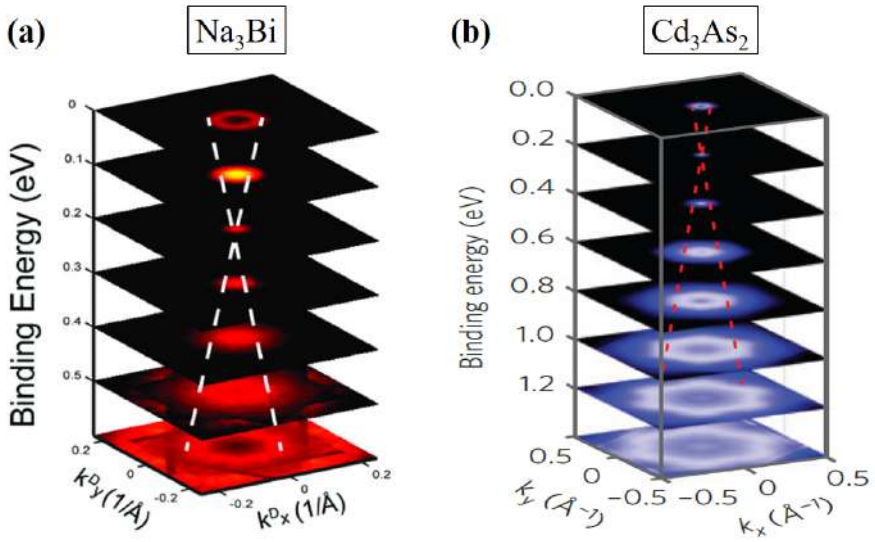

Figure 1.11: 3D Dirac cone observed in ARPES measurements for (a) Na_3Bi (Reproduced from Ref. [28]) and (b) Cd_3As_2 (Reproduced from Ref. [29]).

Weyl Hamiltonian [31],

$$H = \pm c\,\overrightarrow{\sigma}.\overrightarrow{p}. \tag{1.9}$$

The particles, whose motion is described by this Hamiltonian, are called Weyl fermions. Each Weyl fermion has specific helicity (same as chirality for massless particles) or handedness. If its spin is parallel (antiparallel) to its momentum, it is right-handed (left-handed) Weyl fermion. Although theoretically predicted long ago, Weyl fermions have never been experimentally observed. However, with the introduction of topological order in condensed matter physics, it has become apparent that such particles can be realized in crystalline solids. In electronic band structure, a Weyl node appears at the two-fold degenerate crossing point of two linearly dispersing bulk bands. Near this crossing point, the quasi-particle excitations are governed by a Weyl-type Hamiltonian (Equation 1.9 with c replaced by v_F). As shown schematically in Figure 1.12 [32], Weyl node always comes in pairs, i.e., one with right-handed and another with left-handed chirality. Depending on

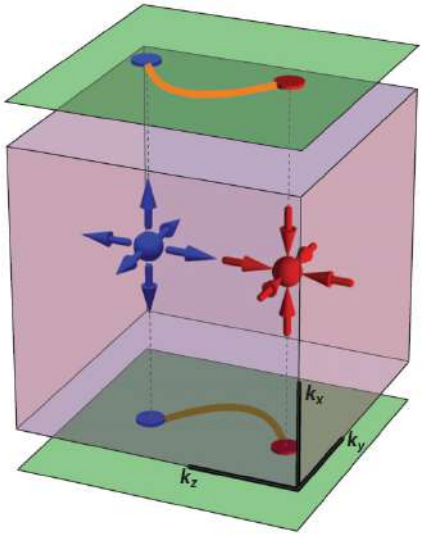

Figure 1.12: A schematic representation of two Weyl points with opposite chirality in the 3D Brillouin zone and the spin-polarized Fermi arc surface states. The red and blue arrows show the direction of the spin vectors. The green sheets correspond to the top and bottom surfaces. Reproduced from Ref. [32].

the chirality, in momentum space, the spin vectors point either towards or away from the Weyl node, forming hedgehog patterns. Hence, these two Weyl points behave like magnetic monopole source and sink. In fact, by breaking either TRS or IS, a bulk Dirac point can be split into two Weyl points with opposite chirality. Another interesting feature of the topological Weyl semimetal (TWS) is the open Fermi arc surface state (Figure 1.12) [33]. A single spin-polarized Fermi arc connects the surface projections of the bulk Weyl points and then continue on the opposite surface. In 2015, TWS state was first predicted in TX (T = Ta, Nb; X = As, P) family of materials [34, 35] and subsequently experimentally verified by several groups [36, 37, 38, 39].

1.8.3 Topological nodal-line semimetal

In TDS and TWS, Dirac and Weyl nodes emerge as discrete band crossing points. This idea can be further extended to topological nodal-line semimetal (TNLS), where the linearly dispersing conduction and valence band cross each other along an one-dimensional closed line in momentum space [40, 41]. Besides the symmetries required for Dirac/Weyl points, this nodal-line is protected by additional symmetries such as mirror reflection. TNLS state was first experimentally observed in $PbTaSe_2$ by G. Bian *et al.* [42].

1.8.4 Type-II Dirac/Weyl semimetal

While preserving the Lorentz symmetry is one of the fundamental requirements in quantum field theory, condensed-matter systems do not possess this constraint. Therefore, for crystalline solids, the Dirac/Weyl-type equation can be generalized, which introduce an additional kinetic term in the energy spectrum [43]. This additional component tilts the Dirac/Weyl cone in momentum space and violates the Lorentz symmetry. Such Dirac/Weyl semimetals are identified as type-II to distinguish from the materials discussed before. Type-II Dirac/Weyl node appears at the contact point of electron and hole pocket, providing the sole opportunity to study Lorentz-violating Dirac/Weyl fermions. Type-II Dirac and Weyl fermions were first observed in $PtTe_2$ [44] and WTe_2 [43], respectively.

1.9 Motivation and organization of the thesis

The emergence of topological materials has introduced a whole new perspective in condensed matter physics, in which the compounds are now characterized in terms

of the topology of their electronic band structure and the physics is governed by the inherent symmetries of the system. These materials are the focus of extensive theoretical and experimental investigations and continue to reveal new exotic topological phases of matter. While topological semimetals (TSMs) present an exclusive opportunity to explore the fundamental physics of relativistic particles in low-energy systems, they are equally compelling due to their unique transport properties. Large magnetoresistance (MR), small effective mass and ultrahigh carrier mobility are some of the characteristic features of these systems, which are highly desirable in magnetic memory, magnetic sensor and spintronics technology. Therefore, at present, one of the major goals is to find suitable materials, which host such quasiparticle excitations and are robust enough for technological applications.

In this thesis, we have investigated the topological nature, Fermi surface properties, structural symmetries and electronic transport properties of several compounds (ZrSiS, LaSbTe, LaBi, $MoAs_2$, VAl_3), which are either theoretically proposed and or confirmed from ARPES measurements to be topologically non-trivial. Each of the systems we studied, represents a large family of isostructural compounds with similar electronic band structure. Hence, our results have encouraged numerous subsequent reports on other members of the groups. The motivation behind each work has been elaborated in the respective chapters. In Chapter 2, we have briefly discussed about the experimental techniques including the single crystal growth methods, which we have used throughout this thesis work. In Chapter 3, the magnetotransport properties of ZrSiS have been presented. In addition to large MR and high mobility, we have probed multiple Dirac nodes at different energy values by combining quantum oscillation and Hall measurements. We have

also observed the signature of chiral anomaly, a relativistic phenomenon proposed in quantum field theory. In Chapter 4, we have analyzed the structural symmetries in ZrSiS using Raman spectroscopy. By combining low temperature and high pressure techniques we have observed possible electronic topological transition in this material. Chapter 5, describes the magnetotransport properties of LaSbTe as well as confirms the theoretical prediction about the topological nature of this material. In Chapter 6, we have resolved the debate over the topological state and Fermi surface properties of LaBi. In Chapter 7, we have studied the Fermi surface properties of $MoAs_2$. An open-orbit Fermi pocket has been observed, which results in unconventional electronic transport properties in this material. Chapter 8 confirms the theoretical prediction of type-II Dirac semimetal state in VAl_3. This chapter also presents one of the first experimental reports of chiral anomaly induced planar Hall effect in TSMs. Finally, in Chapter 9, we have presented the summary of the thesis and discussed about the future scope of work.

2

Experimental details

2.1 Single crystal growth

In order to study the novel phenomena in topological systems, one of the primary requirements is to synthesize the materials in high quality single crystalline form. In polycrystalline samples, grain boundary effects contribute significantly, which often smears the delicate features. Moreover, in topological insulators and semimetals, the surface and bulk electronic states have distinct properties. As large number of grains are randomly oriented in polycrystalline samples, it is impossible to distinguish the surface and bulk effects. Single crystal is the purest state of any compound and possesses very long range atomic ordering. It is not only free from these limitations, but also the well defined crystallographic axes provide the opportunity to investigate the directional dependent physical properties both in real and momentum space. Furthermore, in clean materials with almost no disorder, the mean free path of the charge carriers is very long. This is the essential criterion to observe the quantum oscillations (to be discussed later on), which enable

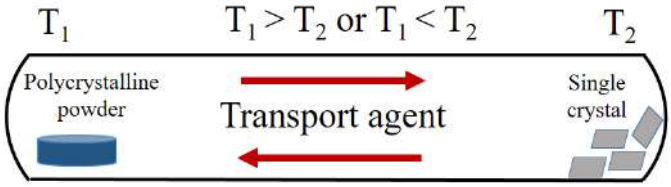

Figure 2.1: A schematic diagram illustrating the chemical vapor transport technique.

us to experimentally probe the Fermi surface of the system. For this thesis work, we have grown the single crystals using two techniques - chemical vapor transport and flux growth. The high purity (99.9% or higher) elements and compounds have been acquired from reputed commercial companies.

2.1.1 Chemical vapor transport technique

Chemical vapor transport technique is used to grow single crystals of those materials, which have insufficient vapor pressure for volatilization. Such materials can be volatilized in presence of a gaseous reactant also known as transport agent. If we apply required external conditions for chemical equilibrium, the transport agent deposits the material in single crystalline form. In general, a temperature gradient is used to stimulate the crystal growth. The process has been shown schematically in Figure 2.1. An endothermic transport agent carries the polycrystalline material from the high temperature end (source) and deposits at low temperature end (sink) as single crystals. For successful crystal growth, one has to optimize several parameters such as the temperature gradient, rate of mass transport, choice and mass of transport agent, etc. The most commonly used transport agents are halogens and halogen compounds. In order to avoid any possible impurity phase and maintain the vapor pressure, the polycrystalline powder and transport agent are

sealed in a quartz tube under vacuum ($\sim 10^{-5}$ Torr). The temperature gradient is created using a two-zone tube furnace.

2.1.2 Flux growth method

The fundamental concept of flux growth method is identical to that of solution growth technique, where single crystals are grown by introducing a nucleation point in supersaturated solution. In flux growth, instead of aqueous solution, we use high purity elements or compounds with low melting point as solvent or flux [45]. The flux and reactants are taken in a cylindrical alumina crucible and vacuum ($\sim 10^{-5}$ Torr) sealed inside a quartz tube to exclude the possibility of any oxidation. Above its melting point, the liquid solvent triggers the chemical reaction even if the reactants have much higher melting point. As we slowly cooled down the solution ($\sim$3°-5°C/h), nucleation points are formed, which start the crystallization (Figure 2.2). In this method, the crystals are surrounded by the liquid flux, which solidifies with decreasing temperature and is difficult to separate. To address this issue, the excess flux is decanted at a temperature above its melting point using a centrifuge. Alternatively, few flux materials can be chemically removed provided the used chemical does not react with the single crystals.

2.2 Sample characterization

The as-grown single crystals were characterized by powder x-ray diffraction (XRD) method as well as high-resolution transmission electron microscopy (HRTEM). We confirmed the phase purity of the sample and extracted the structural parameters from XRD and selected area electron diffraction (SAED) pattern in HRTEM. The

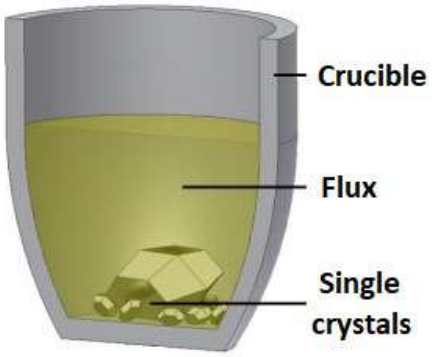

Figure 2.2: Schematic showing the single crystal growth in flux method.

elemental composition of the crystals was checked by energy dispersive x-ray (EDX) spectra obtained through HRTEM.

2.2.1 Powder x-ray diffraction method

XRD is a versatile tool, which is extensively used to determine the structural properties of a material. Powder XRD is performed on polycrystalline samples, where the crystallographic planes of different grains are randomly oriented. In this technique, the sample is exposed to parallel beams of monochromatic x-ray. As x-ray is an electromagnetic wave, it is scattered mainly by the atomic electrons. If the wavelength (λ) of the incident and scattered beams remains same, the scattering is purely elastic. In XRD measurements, we use these elastic scattering events, which contain the information of electronic distribution in the material. For a periodic atomic arrangement [Figure 2.3(a)] as in crystal lattice, each atom scatters the x-rays in all possible directions. The scattered beams interfere with each other either constructively or destructively. Constructive interference results in large enhancement of intensity and is observed at certain angles determined by the

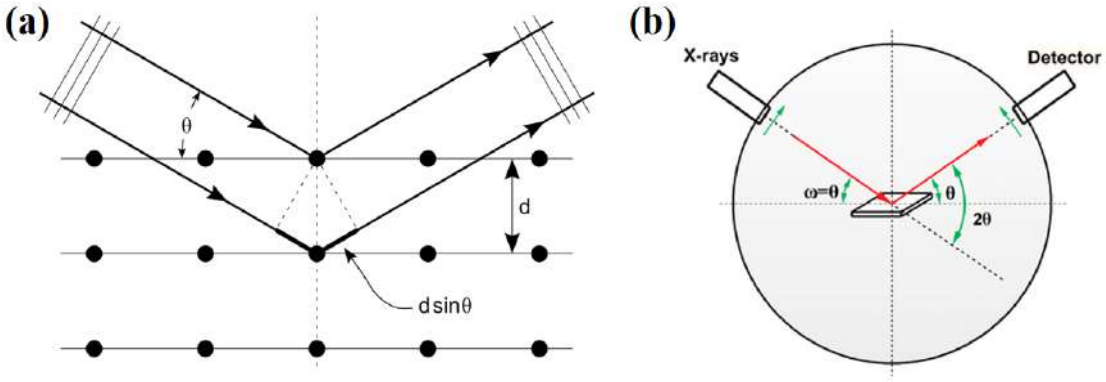

Figure 2.3: (a) Schematic diagram showing the x-ray diffraction by crystallographic planes. (b) Schematic of a x-ray diffractometer operating in Bragg-Brentano geometry.

Bragg's law,

$$2d\sin\theta = n\lambda, \tag{2.1}$$

where d is the interplanar distance, θ is the angle between incident x-ray beam and lattice plane, and n is an integer. At present, most x-ray diffractometers operate in Bragg-Brentano geometry as shown in Figure 2.3(b). In this set-up, the x-ray source and detector move towards each other in a circle around the sample so that if the sample is at an angle θ, the detector is always at 2θ with respect to the incident beam. By scanning the 2θ values continuously, one can obtain all possible Bragg peaks from randomly oriented grains.

For this thesis work, laboratory XRD measurements were performed in a Rigaku x-ray diffractometer (TTRAX III), which operates up to 18 kW and uses Cu $K\alpha$ radiation. The data have been collected by varying 2θ in the range 10° to 90° at intervals of 0.02°. The samples were prepared by crushing and grinding the single crystals. To extract the space group symmetry and lattice parameters, the experimental data have been analyzed by Rietveld structural refinement [46] using the FULLPROF software package [47]. The synchrotron powder XRD experiments

were carried out at Advanced Photon Source, GSECARS, 13IDD beamline with x-ray wavelength 0.3344 Å. We integrated the 2D diffraction images with FIT2D software [48] and analyzed the obtained intensity-2θ patterns using GSAS software [49] to extract the information about the phases and lattice parameters.

2.2.2 High-resolution transmission electron microscopy

The use of different types of microscopes is determined by the resolution power, i.e., the minimum distance required between two adjacent points so that they can be distinctly identified by the microscope. Smaller this distance, the microscope has higher resolution power. This minimum distance (δ) is determined by Rayleigh criterion, $\delta = \frac{0.61\lambda}{\mu \sin\beta}$, where μ is the refractive index of the viewing medium, and β represents the semi-angle of collection of the magnifying lens [50]. The quantity $\mu \sin\beta$, known as numerical aperture, can be approximated as unity. Hence, δ depends solely on the wavelength (λ) of the radiation used. So, for optical microscopes, which use visible spectrum (390 to 700 nm), δ varies between ∼238 to 427 nm. Although these values are quite small compared to macroscopic objects, they are enormous in atomic scale. To get an atomic level picture, we need a new technique and that is where electron microscopes come into play [50].

The working principle of electron microscopy is based on the de Broglie hypothesis, which states that a particle with mass m and velocity v can also behave like a wave with wavelength $\lambda = h/mv$. In non-relativistic limit, this expression becomes $\lambda = h/\sqrt{2mE}$, where E is the kinetic energy of the particle. So, by increasing the energy, we can easily reduce the wavelength. For a free electron with 100 keV energy, this leads to λ ∼4 pm, which is much smaller than atomic radii. This idea was used by M. Kroll and E. Ruska in 1931 to develop the first electron

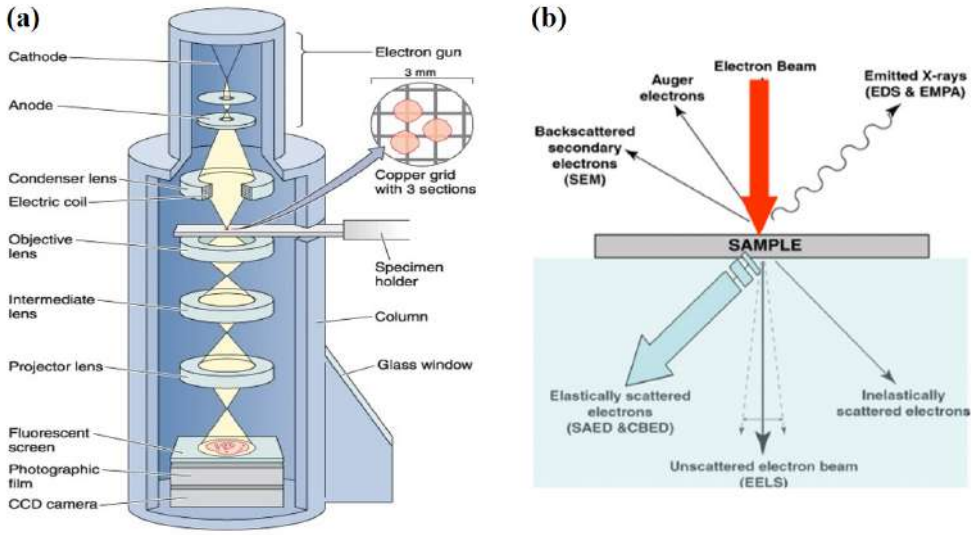

Figure 2.4: (a) Simplified diagram of the major components of a transmission electron microscope. (b) All possible mechanisms by which the electrons interact with the sample.

microscope. In Figure 2.4(a), the major components of a modern transmission electron microscope (TEM) are shown schematically. Note that the arrangements of these components are similar to optical microscope except for the visible light source, which is now replaced by an electron gun. The filament in the electron gun emits stream of electrons, which are accelerated using electrical potential. To focus the electron beam, a series of electromagnetic condenser lenses are used. For TEM, the beam falls on a sufficiently thinned sample so that some electrons can transmit through the material. Other electrons are either scattered or absorbed. In Figure 2.4(b), we have illustrated all possible mechanisms by which the electrons interact with the sample. The intensity of the transmitted beam depends on the atomic number of the element and produces an image on the florescent screen or CCD camera after passing through some electromagnetic lenses. This atomic level image has high spatial contrast, where heavier elements appear darker due to

lower electron transmission, i.e., higher scattering rate. For crystalline solids, the elastically scattered electrons follows the Bragg's law (Equation 2.1) and generate periodic diffraction patterns. By rotating the sample with respect to the electron beam, we can access different crystal planes. The chemical composition of the sample is checked by EDX spectra, which are generated by the inelastically scattered and or absorbed electrons. In both of these events, the atomic electrons in the sample acquire some energy and go to higher energy state. When they return to the ground state, the excess energy is emitted as x-rays with characteristic energy of that particular element. By detecting this x-ray, we can identify individual atom and hence can construct the elemental map of the sample. In EDX, the spatial resolution increases with increasing penetration depth and spreading of the electron beam in the sample. The interaction volume, i.e., the region from which the characteristic x-rays are generated, is large for samples with lower density and higher energy beam. However, in this technique, it is difficult to reliably detect elements with lower atomic number. With reducing atomic number, not only it becomes increasingly difficult to ionize an atom, but also the generated weaker x-ray signals with longer wavelengths are more likely to be absorbed within the sample. Therefore, the detected x-rays from lighter elements mainly come from near the surface of the sample, making them highly sensitive to surface contamination. This problem becomes particularly significant while detecting oxygen and carbon contamination in a sample.

In this thesis work, the high-resolution transmission electron microscopy of the grown crystals has been done in a FEI, TECNAI G^2 F30, S-TWIN 300 kV microscope, equipped with a GATAN Orius SC1000B CCD camera. The EDX spectrum has been collected using the same microscope with additional scanning unit and

high-angle annular dark-field scanning (HAADF) detector (Fischione model 3000).

2.3 Electronic transport and magnetic properties measurements

2.3.1 Electrical resistivity

The electrical resistivity of the samples was measured in either dc or ac mode by four-probe technique [51]. Four ohmic contacts were made on plate- or needle-like single crystals using high-purity gold wires (diameter 25 or 50 μm) and conducting silver paint (Leitsilber 200N). The contact regions were thoroughly covered by the paint. The current (I) was flown between two outer terminals, whereas the voltage (V) was measured between two inner contacts. In Figure 2.5, we have shown a typical single crystal with four electrical terminals. The value of the resistance ($R = V/I$) is recorded within the temperature range 2-300 K in the variable temperature insert of a cryogen free measurement system (CFMS, Cryogenic Ltd.) and a physical property measurement system (PPMS, Quantum Design). Both experimental set-ups are equipped with 9 T superconducting magnet.

For dc transport measurements in CFMS, a Keithley 224 current source and a Keithley 2182A nanovoltmeter were used. The voltage was measured for current flowing in forward and reverse directions, and an average was taken to eliminate the contributions of any thermoelectric effect or offset voltage of the nanovoltmeter. To measure and control the sample temperature, a calibrated Cernox (ceramic-oxynitride) sensor and a LakeShore temperature controller (Model 340) were used. All the data from the electronic meters and temperature controller were recorded

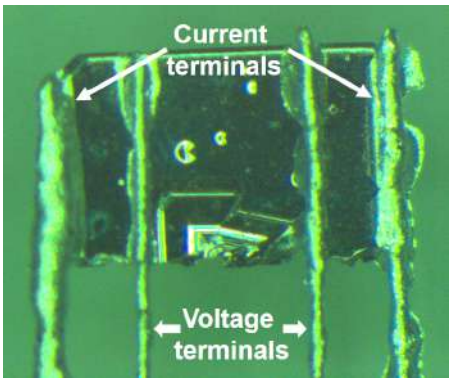

Figure 2.5: A typical single crystal with four electrical terminals.

by Labview software program. The ac resistance was measured using the ac transport option in PPMS [52]. A sinusoidal current of appropriate amplitude and of frequency 13.7 Hz was applied along outer two terminals and the ac voltage was measured between the voltage probes by a lock-in amplifier. The resistance was recorded as a function of temperature and magnetic field by PPMS Multiview software program. The angle dependent measurements were performed using either a home-built (for CFMS) or commercial (for PPMS) sample rotator option. The resistivity (ρ) was calculated using the expression,

$$\rho = \frac{RA}{l}, \tag{2.2}$$

where A is the cross-sectional area perpendicular to the current path and l is the distance between the two voltage terminals.

2.3.2 DC magnetization

The dc magnetization measurements were carried out in a superconducting quantum interference device (SQUID) - vibrating sample magnetometer (VSM) (MPMS3, Quantum Design) [53]. This instrument operates in the temperature range 1.8-400

K with maximum sweep rate 50 K/min and under a magnetic field up to 7 T, which can be varied at a rate up to 700 Oe/sec. The minimum magnetic moment that can be accurately measured is as small as 5×10^{-8} emu. In Figure 2.6 [53], we have shown a simplified schematic of the experimental set-up. The superconducting detection coils function as a second order gradiometer, where the counter wound outer loops ensure that the set of coils are non-responsive to uniform magnetic fields or linear magnetic field gradients. The detection coils produce a current due to local magnetic field disturbances generated by the vibrating sample. If the sample dimensions are much smaller than those of the detection coils, then the current is a function of the position of the sample. This current in the detection coils is inductively coupled to the SQUID, which serves as an ultra-sensitive current to voltage converter. The basic function of SQUID is governed by two phenomena, flux quantization in a superconducting ring and Josephson effect. The Josephson effect describes the current flow across a Josephson junction, i.e., two weakly coupled superconductors separated by a thin insulating barrier. SQUID feedback nulls the current in the detection coils so no current actually flows in them, and the feedback current yields the actual SQUID voltage that gives the sample magnetization value. The VSM vibrates the sample at a frequency ω about the centre of the detection coils. The signal received by the detection coil varies as a function of the sample position (z). Then, at time t, the generated signal by the SQUID is

$$V(t) = AB^2 \sin^2(\omega t), \tag{2.3}$$

as $V(z) = Az^2$ for small vibration amplitudes and $z(t) = B\sin(\omega t)$. A is a scaling factor relating to the magnetic moment of the sample, whereas B is the amplitude of sample vibration. As $\sin^2(\omega t) = \frac{1}{2}$[1-cos(2$\omega t$)], a lock-in amplifier is used to

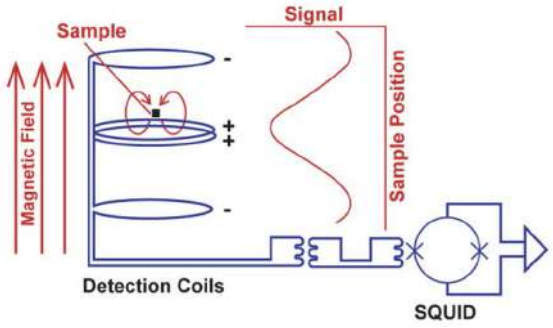

Figure 2.6: Simplified schematic of the SQUID-VSM detection system. Reproduced from Ref. [53].

isolate the signal occurring at frequency 2ω, which is generated exclusively by the sample, provided the vibration frequency is selected properly. This is achieved by multiplying the measured signal with a phase-corrected reference signal at 2ω and then extracting the dc component of the result. The dc component is proportional to the 2ω component of the measured signal. This technique precisely isolates the sample signal from other noise sources, including drifting SQUID signal and mechanical noise sources synchronized to the sample vibration. The lock-in amplification of the SQUID signal is performed by digital electronics in the control module.

2.3.3 Quantum oscillations

As previously discussed in Section 1.2, electrons moving in a strong transverse magnetic field, undergo cyclotron motion. Their energy states then become quantized and form Landau levels. With increasing magnetic field strength, the degeneracy of each Landau level increases and electrons are pushed to lower Landau levels to minimize the energy. When an upper Landau level becomes empty, i.e., Fermi energy of the system passes through the Landau level, it is reflected as oscillation

of the physical quantities such as resistivity (Shubnikov-de Haas effect), magnetization (de Haas-van Alphen effect), thermoelectric power, etc. The frequency of these oscillations, also known as quantum oscillations, is proportional to the extremal Fermi surface cross-sectional area perpendicular to the direction of the applied magnetic field. Hence, by probing the quantum oscillation along different crystallographic directions, we can construct the complete Fermi surface of any material. In addition, from the magnetic field and temperature dependence of the oscillation amplitude, several Fermi surface related parameters can be calculated.

2.4 Raman spectroscopy

In 1928, C. V. Raman discovered the Raman effect, which describes the inelastic light scattering by a material [54, 55]. When a sample is illuminated by light, majority of the photons scatter elastically (Rayleigh scattering), whereas a very small fraction scatter inelastically (Raman scattering). These inelastically scattered photons carry the energy of the characteristic molecular vibrations in the sample, resulting the shift of their frequency. The theory of the microscopic origin for Raman effect can be constructed as follows [56]. An incident photon of angular frequency ω_i can interact with a material by creating or destroying one or more lattice vibration quanta (phonon). In this process, the energy $\hbar\omega$ lost or gained by the lattice is compensated by the increase (anti-Stokes component) or decrease (Stokes component) in the frequency (ω_s) of the scattered photon ($\omega_s = \omega_i \pm \omega$). Let us discuss the first-order Raman effect, i.e., where a single phonon is created or destroyed in the scattering process. Figure 2.7(a) illustrates the process for generating the Stokes component [56]. Note that three steps are involved, a photon (ω_i) is absorbed, an optic phonon (ω) is created and a photon (ω_s) is emitted.

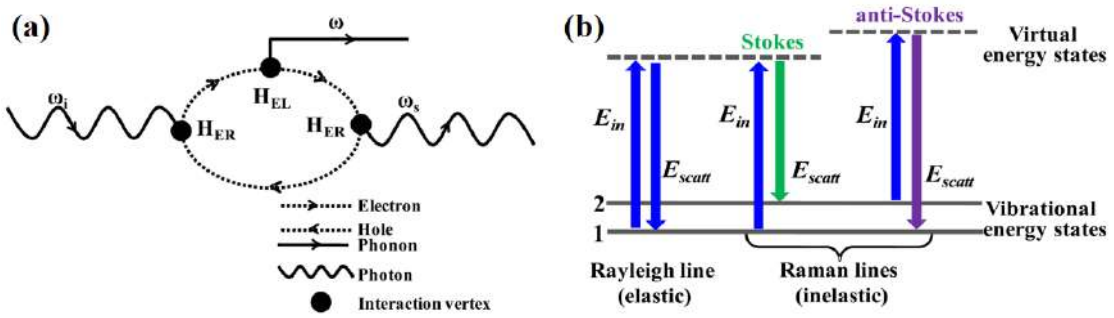

Figure 2.7: (a) Elementary Raman scattering process. Reproduced from Ref. [56]. (b) Energy-level diagram showing the states involved in Raman scattering process.

At the start of the scattering process, the scattering material is generally in its electronic ground state with filled valance bands and empty conduction bands. It again returns to its ground state at the end of the scattering event. The virtual intermediate states involve the excitation of electron-hole pairs. Depending on whether the incident photons interact with a molecule in its vibrational ground state or excited state, the scattering signals appear either at the low energy or high energy side, respectively. As shown in Figure 2.7(b), the Stokes scattering excites the scatterer to an upper energy state. On the other hand, anti-Stokes emission occurs only if the scatterer, which is already at an upper energy state, decays to a lower state. The Stokes and anti-Stokes Raman modes reside symmetrically around the Rayleigh line as they are generated by same upper and lower energy states. However, anti-Stokes lines have lower intensity compared to the Stokes lines, because the number of molecules in an excited vibrational state is very small.

Nowadays, Raman spectroscopy has become a popular, non-destructive and powerful technique to investigate the lattice dynamics and structural symmetries of a system. For this thesis work, the measurements were done in two different

Raman spectrometers, a LABRAM HR 800 system coupled to a liquid nitrogen cryostat to perform experiments at low temperature and an inVia Renishaw Raman spectrometer.

2.5 High pressure measurement techniques

High pressure is an external parameter used to create extreme environment for a material, where new quantum phenomena can emerge. Instead of the complex chemical doping, this technique provides us an effective and clean way to tune the crystal structure as well as chemical potential of a material. We put the sample under pressure up to 57 GPa using a diamond-anvil-cell (DAC). Using diamonds to generate high pressure has certain advantages [57]. In addition to

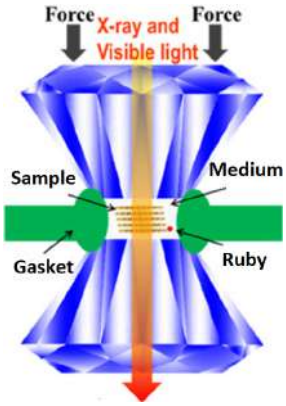

Figure 2.8: Schematic of a diamond-anvil-cell used for generating high pressure. Reproduced from Ref. [58].

be the hardest material known to us, diamond is transparent to infrared, visible, ultraviolet (< 5 eV), and x ray (> 10 keV) radiations, making it suitable for optical spectroscopy and x-ray diffraction experiments. Moreover, it is chemically inert and compatible to electrical and magnetic transport measurements. In Figure 2.8 [58], the schematic of a DAC is shown. Two opposing diamond anvils with small

culets point to each other such that the tips of the anvils generate pressure on the sample, floating in a pressure transmitting medium. We used either silicone oil or Ne gas as the transmitting medium, which ensures good hydrostatic condition at the sample space. Stainless steel or rhenium gaskets were used. The pressure was calibrated using either fluorescence of ruby or equation of state of gold and platinum, which were loaded in the DAC along with the sample.

3

Large nonsaturating magnetoresistance and signature of non-degenerate Dirac nodes in ZrSiS

3.1 Introduction

First-principle calculations [59] and ARPES measurement [60] have shown multiple Dirac crossings as well as unconventional hybridization of surface and bulk states in ZrSiS. This material represents a large family of isostructural compounds (WHM with W=Zr, Hf, La; H=Si, Ge, Sn, Sb; M=O, S, Se, Te) with identical electronic band structure. In this system, the Dirac nodes are protected by non-symmorphic symmetry and they reside at different energy values of band structure, forming a diamond shaped Fermi surface [60]. Another interesting feature of ZrSiS is the energy range of the linear band dispersion. Most of the compounds observed so far, have linear band dispersion up to a few hundred meV, whereas in ZrSiS, the range is

as high as 2 eV at some regions of the Brillouin zone [59, 60]. To observe and exploit the interesting features of Dirac/Weyl fermions, the primary criterion is that the Fermi energy must remain within the linear dispersion region. In reality, materials often undergo uncontrolled doping or their stoichiometry deviates from the ideal value. Therefore, very careful and delicate experimental procedures are required to fulfill this major requirement. In ZrSiS, very large energy range of linear band dispersion ensures that this criterion is satisfied even if the crystals encounter certain amount of carrier doping or non-stoichiometry. So, ZrSiS is a robust topological system and can be used in technological applications. In this chapter, we studied the magnetotransport properties of single crystalline ZrSiS. In addition to the extremely large and non-saturating MR, this compound shows strong anisotropy, when the magnetic field is applied along different crystallographic directions. By analyzing the results of quantum oscillation and Hall effect measurement, we have shown the presence of large hole and small electron Fermi pockets. The observed non-trivial π Berry phase confirms the Dirac fermionic nature for both electron and hole types of carriers. We have also observed the Adler-Bell-Jackiw chiral anomaly, a long-sought relativistic phenomenon of massless Dirac fermions.

3.2 Sample preparation, characterization, and experimental details

We have grown the single crystals of ZrSiS via iodine vapor transport method [61]. First, we synthesized the polycrystalline powder by solid-state reaction in two steps from elemental Zr (Alfa Aesar 99.9%), Si (Strem Chem. 99.999%) and S (Alfa Aesar 99.9995%). Si and S were taken in stoichiometric ratio 1:1 and sealed

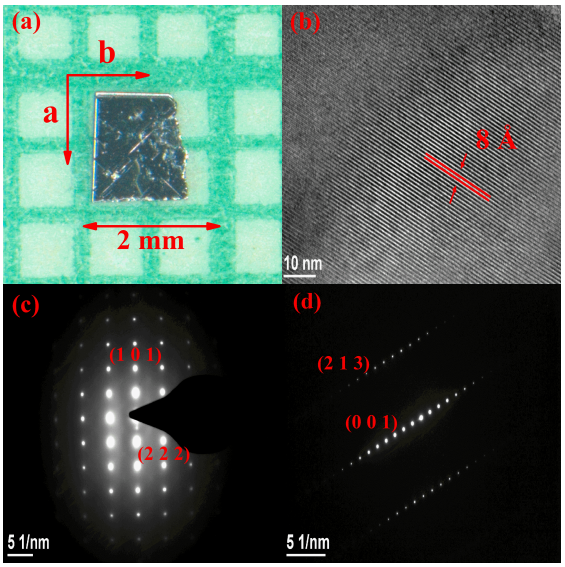

Figure 3.1: (a) A typical ZrSiS single crystal with different crystallographic directions. (b) HRTEM image along the crystallographic *ac*-plane. (c) and (d) SAED pattern obtained from HRTEM measurement with corresponding Miller indices of the crystal planes.

in a quartz tube under vacuum. The tube was then heated at 1000°C for 48 h. The obtained powder was mixed with elemental Zr and sealed in another quartz tube under vacuum. This tube was heated at 1100°C for 48 h. Next, we sealed this polycrystalline powder along with iodine in a concentration of 5 mg/cm^3 in a 20 cm long evacuated quartz tube. We kept the quartz tube in a gradient furnace with the powder at 1100°C, whereas the cooler end at 1000°C. After 72 h, shinny rectangular plate-like crystals were obtained at the cooler end. The single crystals were characterized by HRTEM and EDX spectroscopy. Transport measurements were done via four-probe technique in a 9 T PPMS using the ac transport option as well as in a CFMS employing Keithley nanovoltmeter. Magnetic measurements were performed in a 7 T SQUID-VSM MPMS3. In Figure 3.1(a), we have shown a typical ZrSiS single crystal with dimensions 1.8 mm×1 mm×0.14 mm along with different crystallographic axes. As described in earlier report [60], the crystals

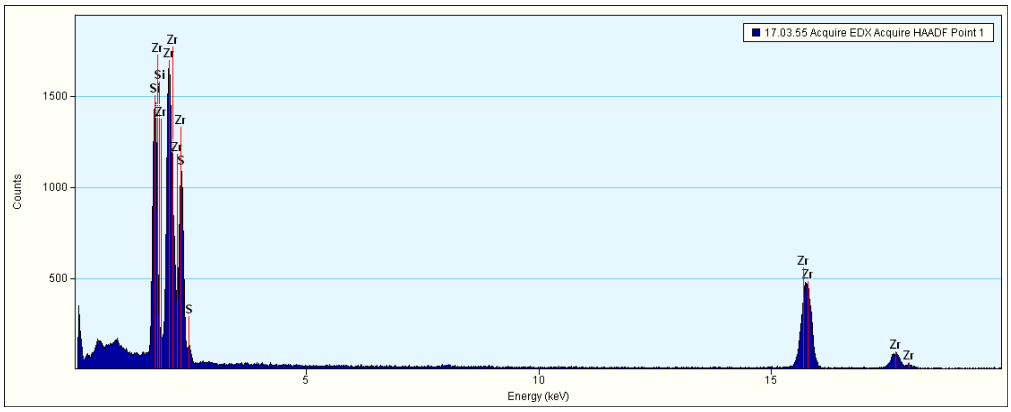

Figure 3.2: EDX spectroscopy data of the as grown single crystal.

cleave perpendicular to c-axis. In Figure 3.1(b), the HRTEM image of the crystal along ac-plane, reveals the high quality crystalline nature and the layered structure of the material with interlayer distance ∼8 Å. In Figures 3.1(c) and (d), we have shown the electron diffraction patterns with corresponding Miller indices of the lattice planes. EDX (Figure 3.2) confirms almost perfect stoichiometry and absence of any impurity in as-grown crystals. We have done the magnetotransport measurements on several crystals from the same batch, which reproduced similar results.

3.3 Results and discussions

3.3.1 Temperature dependence of resistivity

As shown in Figure 3.3(a), the temperature dependence of zero-field resistivity is metallic in nature for ZrSiS. ρ decreases monotonically from room temperature down to 2 K. The value of resistivity becomes as low as ∼52 nΩ cm at 2 K and is comparable to that observed for Cd_3As_2 [62]. Below 10 K, ρ shows some fluctuations within the instrument resolution. We can explain this feature in terms

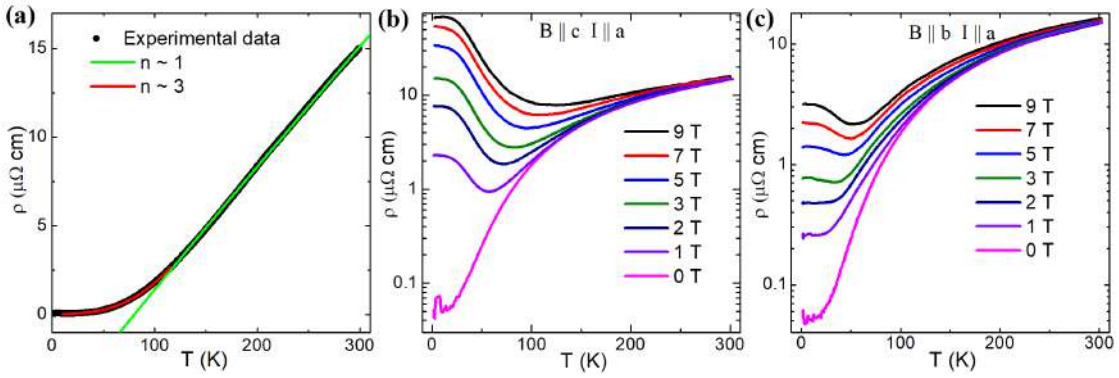

Figure 3.3: (a) The zero-field resistivity of ZrSiS as a function of temperature. The experimental data are fitted using the relation $\rho(T) = \rho_0 + AT^n$. Temperature dependence of resistivity measured with different transverse magnetic field strengths for (b) $\boldsymbol{B} \| c$-axis and (c) $\boldsymbol{B} \| b$-axis configurations.

of the quantum ballistic transport [63]. The ultralow value of residual resistivity and signature of quantum ballistic transport indicate that the mean free path of the charge carriers is very large. So, the impurity effect is almost negligible in ZrSiS. The obtained residual resistivity ratio $\rho(300\ \mathrm{K})/\rho(2\ \mathrm{K})$ is 288, which is quite large and reveals the good metallicity and high crystalline quality of the samples. In the temperature range 10 to 115 K, the resistivity data can be fitted with the expression $\rho(T)=\rho_0+AT^n$ with $n\sim3$. Such behavior suggests a deviation from pure electronic correlation governed scattering mechanism (n=2) [64]. Similar type of temperature dependence of resistivity has also been reported in unconventional semimetals LaSb (n=4) [65], LaBi (n=3) [66], elemental yttrium [67], and transition metal carbide [68] and can be attributed to interband electron-phonon scattering. The resistivity shows linear temperature dependence above 115 K.

As shown in Figure 3.3(b), when the magnetic field is applied, the resistivity enhances drastically in the low temperature region, resulting in a metal-semiconductor-like crossover even at a field of only 1 T. Such magnetic field-induced crossover in TSMs, is often described from the perspective of gap opening at the

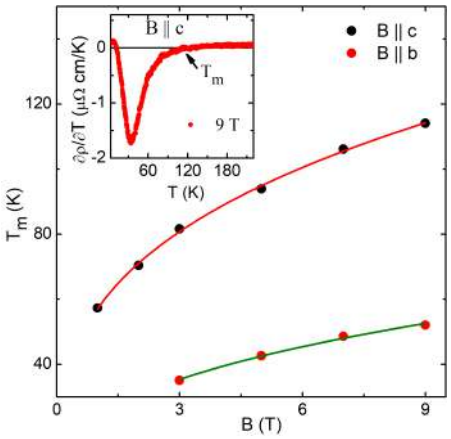

Figure 3.4: Magnetic field dependence of the metal-semiconductor-like crossover temperature for two applied field directions. Inset shows the variation of $\partial\rho/\partial$T as a function of temperature at a field of 9 T, applied along crystallographic c-axis. The point, where the curve crosses the x-axis, represents T_m.

band touching points [65, 66, 69, 70, 71]. It can be clearly seen from Figure 3.3(c) that this metal-semiconductor-like crossover is particularly sensitive to the direction of the applied magnetic field. With current parallel to a- and magnetic field along c-axis, we have observed a strong crossover. On the other hand, when the magnetic field is rotated by 90°, i.e., parallel to b-axis, much weaker crossover is observed. Moreover, this crossover now occurs at higher field strength. The crossover temperature (T_m) can be defined as the temperature, where the resistivity shows minimum, i.e., $\partial\rho/\partial$T becomes zero. In Figure 3.4, we have shown the magnetic field dependence of T_m. For both the magnetic directions, T_m increases monotonically with field and follows $T_m \propto (B - B_0)^{1/\nu}$ type relation. The value of ν is $\sim$3 for both measurement configurations and deviates from the value ν=2, observed for compensated semimetals Bi, WTe_2 and graphite [72, 73].

In Figures 3.5(a) and (b), we have shown the logarithmic behavior of resistivity with inverse temperature, when the magnetic field is applied along two different crystallographic axis. The sign of the slope changes at the point of metal-

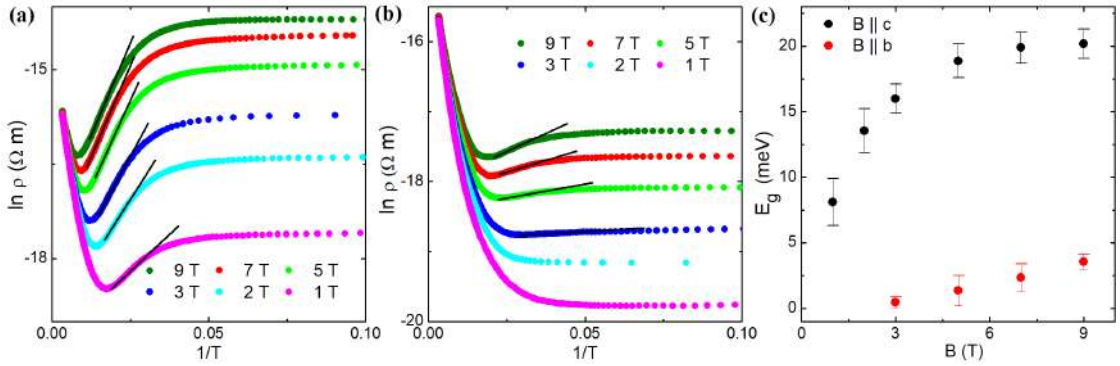

Figure 3.5: $\ln(\rho)$ is plotted as a function of T^{-1} at several transverse magnetic field strengths for (a) $\boldsymbol{B} \| c$-axis, (b) $\boldsymbol{B} \| b$-axis configurations. (c) Magnetic field dependence of the energy gap for two different applied field directions. Error bars indicate the maximum change in E_g, when we change the region of the linear fitting.

semiconductor-like crossover. Using the thermal activated transport model similar to intrinsic semiconductors [74], $\rho(T)=\rho_0 \exp(E_g/2k_BT)$, we have estimated the thermal activation energy gaps ∼20.2 meV and ∼3.7 meV at 9 T, for magnetic field applied along c- and b-axis, respectively. The obtained energy gap E_g exhibits strong magnetic field dependence [Figure 3.5(c)]. As the curves in Figures 3.5(a) and (b) are linear over a very small range of temperature, the value of E_g depends on the linear fitting region and thus, becomes a function of temperature. Following the method by Tafti *et al.* [75], we have determined the energy gap for different temperature regions. In Figure 3.5(c), the error bar shows the maximum change in E_g, when we vary the linear fitting range. For both applied field directions, ρ exhibits an inflection followed by a plateau region below T_m. Similar resistivity plateau in the low temperature region has been observed in several other TSMs and is independent of the sample quality [65, 66, 69, 70, 71]. Hence, this low-temperature resistivity saturation is a generic property of TSMs. However, the origin of this behavior is yet to be settled [65].

3.3.2 Extreme transverse magnetoresistance

We have measured the transverse magnetoresistance (TMR), i.e., the change in resistance upon the application of magnetic field perpendicular to the current direction. As shown in Figure 3.6(a), with current along a- and magnetic field parallel to c-axis, we have obtained an extremely large and non saturating MR. At 2 K and 9 T, TMR is 1.4×10^5 %, which is comparable to that observed in several TSMs [62, 70, 71, 69, 76]. With increasing temperature, this TMR decreases dramatically and becomes just ∼14 % at 300 K and 9 T. In low-field region, TMR manifests a quadratic magnetic field dependence ($\propto B^2$), followed by almost linear behavior at higher field region. As shown in Figure 3.6(b), the MR at 9 T reduces to ∼7000 % at 5 K, when we apply the field along b-axis and keep the current direction unaltered. The calculated anisotropic ratio $\rho(\boldsymbol{B}\|c)/\rho(\boldsymbol{B}\|b)$ at 3 K and 9 T, is 21, which is large and comparable to what has been observed in $NbSb_2$ [71]. This reveals strong anisotropy in electronic structure, which is associated to the quasi two-dimensional nature of the Fermi surface in ZrSiS as observed from ARPES [60]. For a two-dimensional system, where the charge carriers are confined within the plane, the motion of the electrons remains unaffected by a magnetic field applied parallel to the plane, i.e., the anisotropy in MR would be extremely large. As shown in Figure 3.6(c), we can not rescale the MR data for different temperatures to a single curve using the Kohler's rule MR=$\alpha(\mu_0 H/\rho_0)^m$. The violation of Kohler's rule suggests the presence of more than one type of charge carrier and or the different temperature dependencies of their mobilities [73, 77].

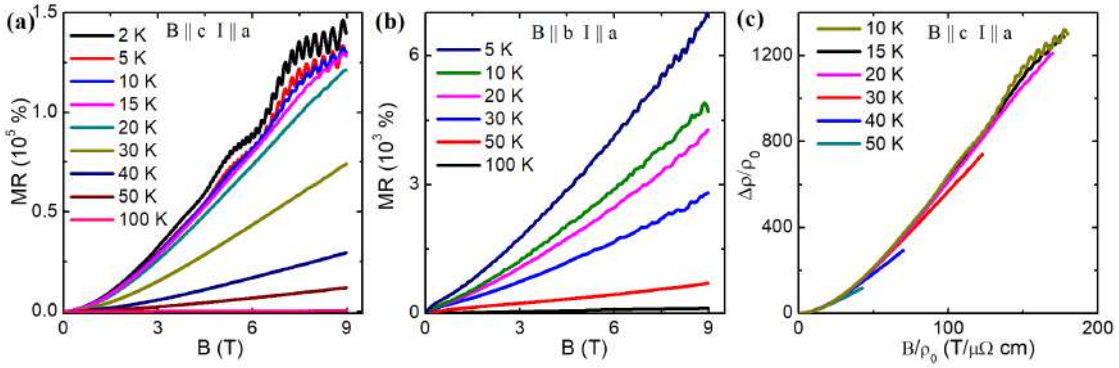

Figure 3.6: Transverse magnetoresistance as a function of magnetic field with current along a-axis and field applied along (a) c-axis and (b) b-axis, measured at different representative temperatures. (c) Scaling of MR data using the Kohler's rule with field parallel to c-axis.

3.3.3 Longitudinal magnetoresistance and chiral anomaly

We have measured the longitudinal MR (LMR) with both the current and magnetic fields applied along a-axis. As shown in Figure 3.7(a), negative MR has been observed in the low field region. With the increasing temperature, the negative MR progressively weakens. This negative LMR can be ascribed to Adler-Bell-Jackiw (ABJ) chiral anomaly. This is a relativistic phenomenon, which was first proposed in quantum field theory in 1969 [78, 79] and later generalized in the context of condensed matter physics [80]. In Dirac systems, a Dirac node splits into two opposite chirality Weyl nodes due to broken TRS under the application of magnetic field. Parallel electric ($\boldsymbol{E}$) and magnetic field ($\boldsymbol{B}$) act as a non-trivial gauge field ($\boldsymbol{E}.\boldsymbol{B}$), inducing the chiral anomaly, i.e., charge imbalance between the two Weyl nodes of opposite chirality. This generates an extra flow of current along the direction of the applied electric field and hence, results in the negative LMR. The chiral magnetic effect, which is a long sought phenomenon in particle physics, has been observed in several 3D Dirac and Weyl semimetals such as Cd_3As_2

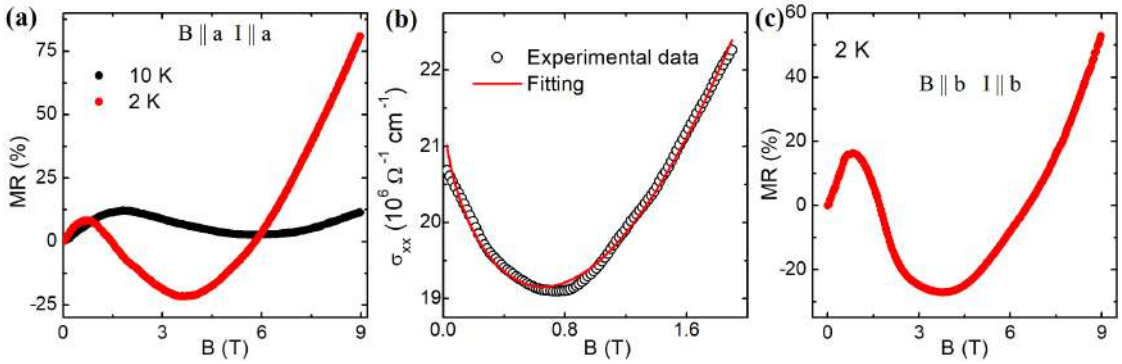

Figure 3.7: (a) LMR with both current and magnetic field parallel to a-axis. (b) Fitting of the longitudinal magnetoconductivity data at 2 K using semiclassical formula. (c) LMR at 2 K with both current and field along b-axis.

[81], Na_3Bi [82] and TaAs [76]. The field dependence of longitudinal conductivity $[\sigma_{xx}(B_x)]$ at a particular temperature, follows the semiclassical relation [76],

$$\sigma_{xx}(B_x) = (1 + C_w B_x^2)(\sigma_0 + a\sqrt{B_x}) + (\rho_0 + AB_x^2)^{-1}, \tag{3.1}$$

where σ_0 and ρ_0 are the zero-field conductivity and resistivity at that temperature, respectively. C_w is a temperature dependent parameter, which originates from chiral anomaly. $(\sigma_0 + a\sqrt{B_x})$ describes the low-field minima in the conductivity, which is generally attributed to the weak anti-localization effect in Dirac systems [76, 82]. On the other hand, the last term on the right-hand side corresponds to the contribution from any non-linear bands near the Fermi level. Figure 3.7(b) shows the good agreement between the theoretical relation and experimental results. From Figure 3.7(a), we see that the MR becomes positive at higher magnetic fields, which occurs due to the small unavoidable misalignment between $\boldsymbol{E}$ and $\boldsymbol{B}$. Hence, there is a competition between the negative LMR and positive TMR components. The temperature dependence of these two components is different and the TMR diminishes more rapidly with increase in temperature.

Therefore, the minimum in MR shifts towards higher field with increasing temperature. We determined a small misalignment angle $\sim 2^{\circ}$ by fitting the high-field region of MR for all the temperatures. The LMR has also been measured with $\boldsymbol{E} \| \boldsymbol{B}$ along different crystallographic directions as well as on several crystals. For all the cases, we have observed similar negative MR, which confirms that negative LMR is associated with $\boldsymbol{E} \| \boldsymbol{B}$ configuration rather than any particular crystallographic axis. In Figure 3.7(c), we have shown the measured LMR for $\boldsymbol{E} \| \boldsymbol{B} \| b$-axis, as a representative. In addition to the Dirac and Weyl semimetals, a few ultra-clean layered materials such as $PdCoO_2$, $PtCoO_2$ and Sr_2RuO_4 also show negative LMR [83]. However, the nature of the reported negative MR in these materials is completely different from that originated from the chiral anomaly. In these layered compounds, negative MR appears, when $\boldsymbol{E}$ and $\boldsymbol{B}$ are applied along certain crystallographic direction. For other directions, MR is positive, even under parallel $\boldsymbol{E}$ and $\boldsymbol{B}$ configuration, unlike Dirac or Weyl semimetals. For example, the negative MR is observed in $PdCoO_2$ and $PtCoO_2$ only for $\mathbf{E} \| \mathbf{B} \| c$-axis configuration or when $\boldsymbol{B}$ is close to an Yamaji angle and in Sr_2RuO_4 only if $\boldsymbol{E}$ and $\boldsymbol{B}$ are within 10° of the crystallographic c-axis. Furthermore, in these materials, the MR decreases linearly with increasing magnetic field from its zero-field value. On the other hand, in 3D Dirac/Weyl semimetals, the chiral anomaly induced negative MR shows quadratic field dependence as described by Equation 3.1.

3.3.4 Shubnikov-de Haas oscillation and Fermi surface properties

Another prominent feature, which emerges from our transport measurement, is the presence of Shubnikov-de Haas (SdH) oscillation traceable at magnetic field

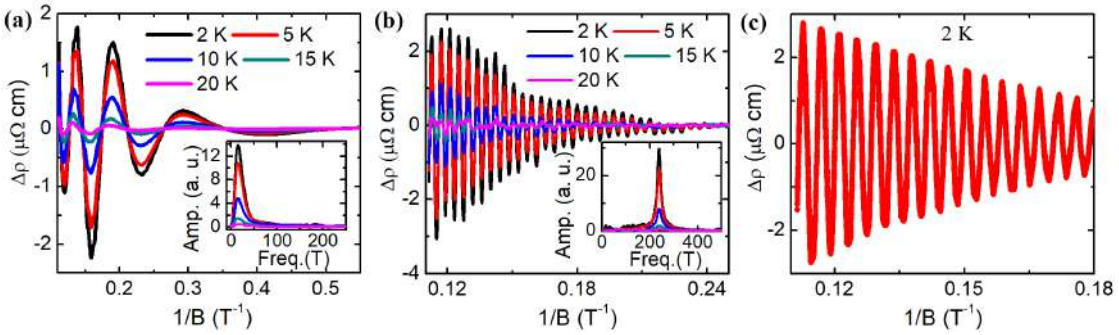

Figure 3.8: (a) & (b) SdH oscillation extracted by subtracting smooth background from the magnetoresistance data, plotted as a function of inverse magnetic field $(1/B)$ at different representative temperatures for the two deconvoluted components. The corresponding FFT results are shown in the insets of both figures. (c) The SdH oscillation for 238 T frequency, measured with very small field interval at 2 K.

even below 2 T and temperature as high as 20 K. This gives an insight into the nature of the Fermi surface as well as provides an evidence of very high mobility of the carriers. From the TMR data, it is evident that there are more than one frequency. To extract the oscillatory component $\Delta\rho(B)$, we have subtracted a smooth background from $\rho(B)$. The background subtraction has been done in two steps to deconvolute the two components of oscillation. In Figures 3.8(a) and (b), $\Delta\rho(B)$ is plotted as a function of $1/B$ at several representative temperatures for two different components. As the oscillation peaks are extremely sharp and the magnetic field interval used for the measurements is not too small in comparison to the peak width, we have observed some fluctuations in the intensity as shown in Figure 3.8(b). When we use a much smaller field interval, the peak intensity becomes systematic [Figure 3.8(c)]. The fast Fourier transform (FFT) analysis of the oscillatory components shows oscillation frequencies 14 T and 238 T. The obtained frequencies reveal the presence of a very large and another small Fermi surface cross-sections perpendicular to the crystallographic c-axis. Using the On-

sager relation, $F = (\varphi_0/2\pi^2)A_F$, where φ_0 is the single magnetic flux quantum and A_F is the Fermi surface cross-section perpendicular to the applied magnetic field, we have obtained cross-sections 1.4×10^{-3} Å^{-2} and 22.7×10^{-3} Å^{-2} for 14 T and 238 T frequencies, respectively. The oscillation amplitude for both the frequency components is shown in Figure 3.9(a) as a function of temperature. The experimental data have been fitted using the thermal damping factor of Lifshitz-Kosevich formula, $R_T = (2\pi^2 k_B T/\beta)/\sinh(2\pi^2 k_B T/\beta)$, where $\beta = e\hbar B/m^*$. From the fitting parameters, the cyclotron effective masses (m^*) of the charge carriers are calculated to be $\sim$0.14 m_0 and $\sim$0.1 m_0 for 238 T and 14 T frequencies, respectively. Here, m_0 is the rest mass of the free electron. To estimate the approximate value of the carrier density, we have used the relation [84], $\Delta\left(\frac{1}{B}\right) = \frac{2e}{\hbar}\left(\frac{g_s g_v}{6\pi^2 n_{3D}}\right)^{2/3}$, where g_s and g_v are the spin degeneracy and valley degeneracy, respectively. We have determined the carrier densities (n_{3D}) to be 2×10^{19} cm^{-3} and 3×10^{17} cm^{-3} corresponding to the large and small Fermi pockets, respectively. From the magnetic field-induced damping of the oscillation amplitude, $\Delta\rho \propto exp(-2\pi^2 k_B m^* T_D/\hbar eB)$, the Dingle temperatures (T_D) at 2 K are calculated to be 11.2 K and 3.4 K for the large and small Fermi pockets, respectively. We have also calculated the quantum mobility, $\mu_q = (e\hbar/2\pi k_B m^* T_D)$ to get a quantitative estimate about the mobility of the charge carriers. The obtained values $\sim1.3\times10^3$ cm^2 V^{-1} s^{-1} and $\sim6.2\times$ 10^3 cm^2 V^{-1} s^{-1} corresponding to the large and small frequencies, respectively, show the significant difference between the mobilities of the associated charge carriers. It is expected as the carriers associated with the Fermi pockets have different effective masses (mobility$\propto \frac{1}{m^*}$). We note that the quantum mobility is always lower than the classical Drude mobility (μ_c) in a system, as μ_q is sensitive to both large and small angle scattering, whereas μ_c is sensitive to only large angle scattering

Table 3.1: Parameters extracted from the Shubnikov-de Haas oscillation for two Fermi pockets in ZrSiS. Here, k_F, v_F, l are the Fermi momentum, Fermi velocity and mean free path of the charge carriers, respectively.

F	k_F	m^*	v_F	l	μ_q	n_q
T	10^{-2}Å^{-1}	m_0	10^5m/s	nm	10^3cm^2/Vs	10^{17}cm^{-3}
238	8.5	0.14	2.4	25.7	1.3	200
14	2	0.1	6.9	247.4	6.2	3

[85]. We have summarized all the extracted parameters from SdH oscillation in Table 3.1. With magnetic field along b-axis, we have not observed any clear oscillation up to 9 T applied field. This can be due to heavier effective mass and low mobility of the carriers along that direction and/or quasi two-dimensional nature of the Fermi surface in ZrSiS.

3.3.5 Angle dependence of oscillation frequencies

We have performed angle resolved TMR measurements and SdH oscillation analysis for deeper understanding of the Fermi surface geometry. The FFT spectra for different applied field directions, are shown in Figure 3.9(b). The inset illustrates the experimental set-up with current along crystallographic a-axis and magnetic field rotated in the bc-plane. As evident from the FFT spectra, the low-frequency component F_α (14 T) remains unaffected with increasing angle up to 20°, after which it splits into two closely spaced frequency branches. However, with further increase in angle, these two peaks come close to each other and merge to become a single component. On the other hand, the high-frequency branch F_β (238 T) bifurcates into two components, (F_δ and F_ε), which are well apart in the frequency spectra. The higher one (F_ε) among the two, disappears above a certain angle, whereas F_δ is seen to shift towards lower value and then bifurcates into F_ω and F_ϕ.

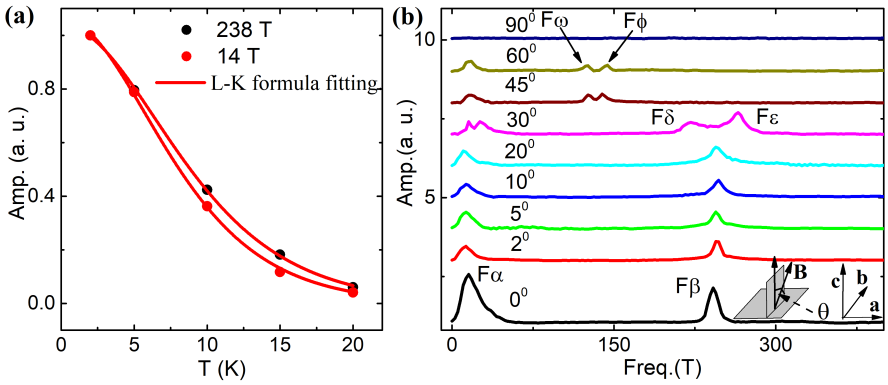

Figure 3.9: (a) Variation of the relative amplitude of SdH oscillation with temperature for both the Fermi pockets. (b) The angle dependence of oscillation frequencies. FFT results for different angles are shifted vertically for clarity. Inset shows the schematic of the experimental setup.

As we have already discussed, with current along a- and magnetic field parallel to $\boldsymbol{b}$-axis (θ=90°), no clear oscillatory component has been observed.

3.3.6 Berry phase and Zeeman splitting

Under an applied magnetic field, a closed orbit is quantized according to the Lifshitz-Onsager quantization rule [86],

$$A_F \frac{\hbar}{eB} = 2\pi(n + \frac{1}{2} - \beta - \delta) = 2\pi(n + \gamma - \delta), \tag{3.2}$$

where $2\pi\beta$ is the Berry phase and δ is a phase shift, which is determined by the dimensionality. δ have value 0 and $\pm 1/8$ for 2D and 3D cases, respectively. The value of the Berry phase determines the nature of the electronic band dispersion. It is 0 for the conventional parabolic band dispersion and π for the Dirac or Weyl type electronic systems, which host linear band dispersion. The quantity $\gamma - \delta = \frac{1}{2} - \beta - \delta$, can be obtained from the x-axis (along which we have plotted the Landau level index n) intercept in the Landau level index plot and takes a value either -1/8

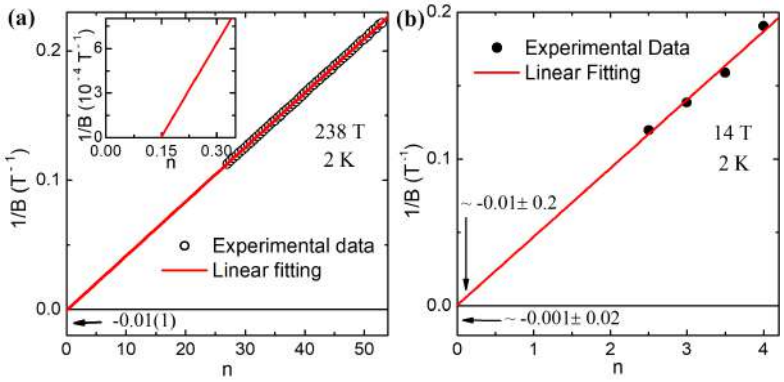

Figure 3.10: (a) Landau level fan diagram for 238 T frequency oscillation. The x-axis intercept by extrapolated linear fitting is shown in the inset. The arrow shows the value of y-axis intercept. (b) Landau level index plot for 14 T frequency. The arrows show the value of x- and y-axis intercepts.

or +1/8 for 3D Dirac fermions [86]. In Figure 3.10(a), we have plotted the Landau level fan diagram for the larger frequency component in ZrSiS, assigning maxima of the SdH oscillation as integers (n) and minima as half-integers (n+1/2). The extrapolated linear fitting leads to an intercept of 0.15(3) (shown in the inset). The sharp, symmetric and well-separated oscillation maxima/minima over a wide range (n=27 to 53) and traceable down to ∼4 T, ensure no significant error in estimating the value of the intercept from the linear n vs. $1/B$ fit. On the other hand, to achieve lower Landau level, higher applied magnetic field may cause non-linearity in the index plot from the Zeeman splitting of oscillation peaks as has been seen for 14 T frequency and discussed below. Similar to what observed for 238 T frequency, we have obtained a small intercept ∼ -0.01 for 14 T frequency [Figure 3.10(b)]. The intercepts are very close to the theoretical value ±1/8 for both the Fermi pockets. As the index plot for 14 T frequency shows weak non-linearity, the intercept has been obtained from the best linear fit. Though this method can introduce some error in the estimated intercept, even with maximum error (±0.18), which has been determined from the linear fitting of the first three

and last three points, the obtained intercept is very close to the earlier mentioned theoretical value for linear band dispersion and far from that expected (0.5) for conventional quadratic band structure. For the smaller Fermi pocket, the deviation of the peak positions from a straight line is due to the Zeeman splitting of the Landau levels [85, 87]. While the Zeeman splitting is not clearly visible in the SdH oscillation, the spin-split peaks are easily distinguishable in the de Haas-van Alphen (dHvA) oscillation in the magnetization measurements [Figures 3.11(a)]. In Figure 3.11(b), we have plotted the oscillatory part of magnetic susceptibility $\Delta\chi$=dM/dB after subtracting the background. In order to construct the Landau level fan diagram, if we assign integer indices n for maxima in ΔM, the maxima in $\Delta\chi$ should correspond to n+1/4 [88]. Therefore, in Figure 3.11(c), we have plotted the Landau level index n+1/4 for smaller frequency, using the peak and valley positions of the oscillations at low field region, which is almost free from any Zeeman splitting. The linear nature of the index plot suggests almost no error in the obtained intercept. We have obtained a small intercept 0.05(2), which confirms the Dirac fermionic nature of the carriers associated to the small Fermi pocket. In addition, we have also calculated the Berry phase from the SdH oscillations, measured at different angles (up to 20°), and observed no significant change. Due to the presence of multiple oscillation frequencies, it is much more complicated to determine reasonably accurate value of Berry phase for higher angles.

3.3.7 Hall measurement and signature of non-degenerate Dirac nodes

We have also performed the Hall effect measurement to reveal the nature of the charge carriers associated with the two Fermi pockets. At 300 K, the Hall resistivity

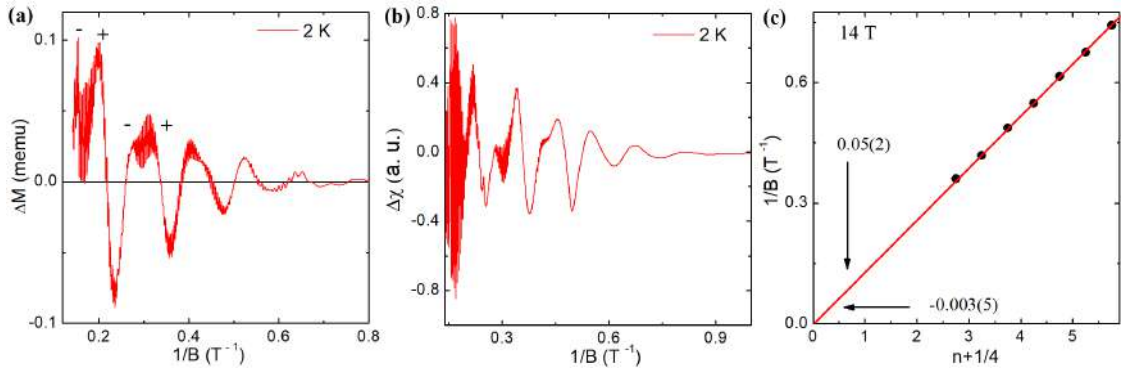

Figure 3.11: (a) The de Haas-van Alphen oscillation at 2 K, extracted after background subtraction. (b) The oscillatory component ($\Delta\chi$) of the magnetic susceptibility data for the smaller frequency. (c) The Landau level index n+1/4 plotted against $1/B$ for the smaller frequency. The arrows show the value of x- and y-axis intercepts.

(ρ_{xy}) is positive and almost linear in magnetic field [Figure 3.12(a)], which imply that holes are majority carriers, consistent with the earlier ARPES report [60]. The Hall resistivity develops a sublinear character with decreasing temperature. At around 50 K, ρ_{xy} changes its sign from positive to negative in high magnetic field region, thus confirming the presence of more than one type of carrier. The overall behavior can be explained by considering low-mobility holes and higher-mobility electrons, which are associated with large and small Fermi pockets, respectively. Using the classical two-band model in the low-field limit [89, 90],

$$\rho_{xy} = \frac{B}{e}\frac{(n_h\mu_h^2 - n_e\mu_e^2)}{(n_h\mu_h + n_e\mu_e)^2}, \tag{3.3}$$

we have fitted the Hall resistivity in Figure 3.12(b). n_h (n_e) and μ_h (μ_e) are the hole (electron) densities and mobilities, respectively. Obtained values of electron and hole densities, 1.6×10^{17} cm^{-3} and 6×10^{19} cm^{-3}, respectively, are in good agreement with those calculated from SdH oscillation. As expected, from the fitted parameters, large electron mobility $\sim 2\times10^4$ cm^2 V^{-1} s^{-1} and hole mobility

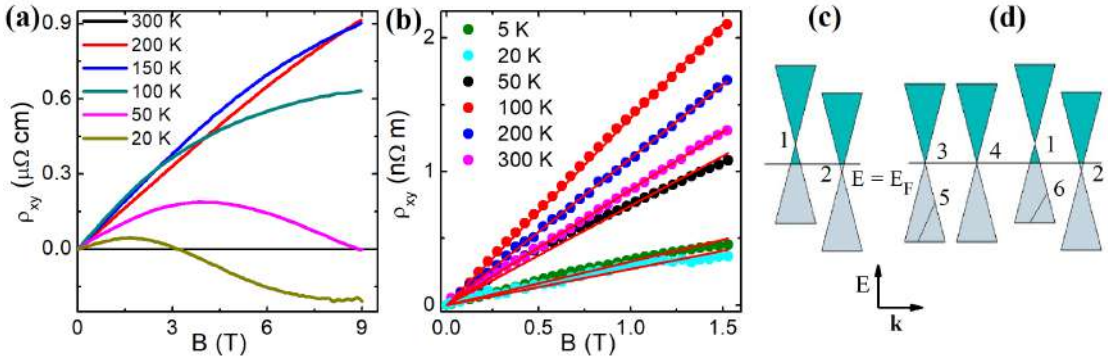

Figure 3.12: (a) Magnetic field dependence of the Hall resistivity in ZrSiS, measured at several representative temperatures. (b) Classical two-band model fitting of the Hall resistivity data. (c) Schematic describing the magneto-transport measurement results. (d) Schematic illustrating multiple Dirac cones at different energy values as reported in earlier studies [59, 60].

$\sim 2.8\times10^3$ cm^2 V^{-1} s^{-1} have been obtained at 5 K. From the Hall measurements, it is clear that at least two band crossings exist in the electronic band structure of ZrSiS at different energy values, as illustrated schematically in Figure 3.12(c). The earlier studies on ARPES measurements and electronic band structure calculations suggest that there are multiple Dirac crossings at different energy values as shown in the schematic Figure 3.12(d). The Dirac cones 1 and 2 cross the Fermi energy with corresponding Dirac points at two different energy values. Among the others, 3 and 4 have their Dirac points almost at the chemical potential with negligible Fermi surface volume, whereas 5 and 6 are well below the Fermi energy. Thus in this scenario, it is expected that only Dirac cones 1 and 2 will participate in the transport properties of ZrSiS, which is consistent with the results of our magneto-transport measurements.

3.4 Summary and conclusions

In summary, we present the systematic study of the magneto-transport properties on single crystalline ZrSiS. We have observed magnetic field-induced metal-semiconductor-like crossover as well as strongly anisotropic transport properties in this material. The anisotropic MR along different crystallographic directions is in excellent agreement with the quasi two-dimensional nature of the Fermi surface reported in ARPES. Transverse MR shows an extremely large value $\sim 1.4\times10^5$ % at 2 K and 9 T, without any indication of saturation. Under parallel $\boldsymbol{E}$ and $\boldsymbol{B}$ configuration, negative MR is observed, which originates from Adler-Bell-Jackiw chiral anomaly of three-dimensional Dirac fermions. The SdH oscillation shows two inequivalent Fermi pockets perpendicular to crystallographic c-axis. The Dirac fermionic nature of the carriers is confirmed from the non-trivial π Berry phase for both the Fermi pockets as determined from the Landau level fan diagram. Non-linear magnetic field dependence of Hall resistivity implies the presence of both electron and hole type charge carriers. The theoretical fitting of Hall resistivity using classical two-band model, reveals very high mobilities for both types of charge carrier. SdH oscillation along with Hall measurement reflect multiple band crossings at different energy values of the electronic band structure.

4

Probing the lattice dynamics and electron-phonon coupling in topological nodal-line semimetal ZrSiS

4.1 Introduction

Except for ZrSnTe [91], ARPES and transport measurements have revealed topological nodal-line semimetal phase in several members of *WHM* family [60, 92, 93, 94]. In these materials, the bulk valence band and conduction band cross each other along an one-dimensional line in momentum space instead of discrete Dirac points, thus making them even more fascinating from the perspective of fundamental physics. ZrSiS is the starting member of this family, which hosts multiple linear band crossings at different energy values of bulk band structure, forming a nodal-line and with highest reported energy range of linear band dispersion [60]. Furthermore, the quasi two-dimensional Fermi surface, extremely large magnetore-

sistance and multi-band dominated quantum oscillations, have been the focus of a number of recent studies in ZrSiS [60, 92, 93]. These reports inferred that the layered structure along with square Si atom sublattice, essentially controls the novel topological properties in ZrSiS and other isostructural materials. In fact, it is well established that the structural symmetries play a pivotal role in protecting the accidental degeneracies and non-trivial topological bands in a compound. On the other hand, by breaking the symmetries, we can drive the system to electronic topological transitions. Raman scattering is a powerful nondestructive tool to study the structural symmetries of a material and to probe the impact of phonon on electronic energy bands [95, 96, 97]. Together with low-temperature measurements and high-pressure technique, this method enables us to draw a detailed picture of the phonon dynamics, electron-phonon interaction as well as possible structural and topological phase transitions. These information are crucial for understanding the structural, thermal, and electronic properties, and may also help to comprehend the underlying mechanism of the observed topological nodal-line semimetal phase in ZrSiS and in other members of the *WHM* family.

In this chapter, we shall discuss the Raman spectroscopy measurements on ZrSiS single crystals. We have probed the Raman modes in the *basal plane* (crystallographic c-axis is along the wave vector k_i of the incident laser) and *edge plane* (k_i is perpendicular to the crystallographic c-axis) configurations. All the Raman active modes at the Brillouin zone center and their corresponding vibrational patterns have been identified from the first-principles calculations and crystal symmetry analysis. We have also analyzed the polarization-resolved as well as crystal-angle-resolved Raman measurement data in detail. From the wavelength and temperature dependent Raman studies, the complex interplay of phonons with electronic

degree of freedom has been identified. To further explore the phonon dynamics, Raman scattering experiments have been performed under high-pressure. Pressure is a clean and effective way to tune the lattice along with the electronic states and is expected to have a substantial impact on the layered structure of ZrSiS. In addition to the softening of the phonon modes, pressure-induced vibrational anomalies have been observed in the Raman spectra. To correlate the obtained results, we have performed high-pressure synchrotron x-ray diffraction (HPXRD) measurements. HPXRD spectra reveal structural phase transitions together with the coexistence of multiple phases and also likely to be accompanied by the electronic topological transition in ZrSiS.

4.2 Experimental and computational details

The details of crystal growth and characterization are provided in the previous chapter. The ambient pressure and low-temperature Raman measurements were performed in a LABRAM HR 800 system. This set-up is equipped with a spectrometer of 80 cm focal length, 1800 lines/mm grating and a Peltier cooled CCD. To excite the sample, lasers of wavelength 488, 633 and 785 nm were used. The laser beam was focused on the crystal using 100X objective with numerical aperture 0.9. We prepared a symmetric DAC with culet size 300 μm to apply high pressure on the crystal. Stainless steel or rhenium gaskets were pre-indented with 36 μm thickness. Next, we made a 170 μm-diameter hole at the central part of the gaskets by laser-drilling. To avoid any damage of the crystal and to maintain a good hydrostatic condition, we ensured that the sample thickness is about one-third of the gasket thickness. Silicone oil was used as a pressure transmitting medium. The pressure calibration was done by ruby fluorescence method [98]. Raman spectra up

to 57 GPa were recorded using an inVia Renishaw Raman spectrometer operating with a 532 nm exciting laser and 2400 lines/mm grating. For HPXRD experiments, same DAC was used but with Ne gas as the pressure-transmitting medium. In this case, pressure was calibrated through the equation of state of gold and platinum, which were also loaded inside the DAC along with the sample.

All first-principles density functional theory (DFT) [99, 100] based calculations have been performed using the *Vienna Ab-initio Simulation Package* (VASP) [101, 102, 103]. We have used projector-augmented wave (PAW) potentials [104, 105], and expanded the wave functions in the plane-wave basis with a kinetic energy cut-off at 350 eV. The exchange-correlation function was chosen to be Perdew-Burke-Ernzerhof (PBE) [106] implementation of the generalized gradient approximation (GGA). In our simulations, total energies were converged to less than 10^{-6} eV. For structural relaxation, the positions of the ions were relaxed towards the equilibrium using conjugate gradient algorithm, till the Hellman-Feynman forces became less that 0.001 eV/Å. The phonon band structure has been calculated using the finite difference method [107, 108], as realized in the PHONOPY code [109, 110] in conjugation with DFT as executed in the VASP code. We have also calculated the zone center phonon frequencies using density functional perturbation theory (DFPT) [111] as implemented in the VASP code to further check our results.

4.3 Results and discussions

4.3.1 Crystal structure and experimental setup

ZrSiS crystallizes in tetragonal structure with space group $P4/nmm$ (129) and point group D_{4h} [61, 112]. Figure 4.1(a) shows the crystal structure of ZrSiS with

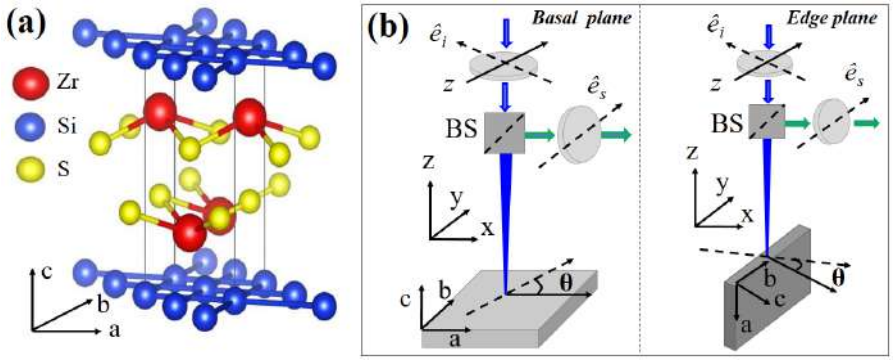

Figure 4.1: (a) Crystal structure of ZrSiS. (b) Schematic representation of the Raman measurement set-ups for *basal plane* and *edge plane* configurations.

crystallographic axes a, b, and c. Layers of Zr and S atoms are sandwiched between the square nets of Si, which are located in the ab-plane. The neighboring S atoms reside between two layers of Zr. We have performed the XRD experiments on the powdered crystals (discussed later) and analyzed the data by Rietveld structural refinement using FULLPROF software package. The refined lattice constants are a=b=3.546(2) and c=8.055(4) Å. The obtained lattice parameter along c-axis is in excellent agreement with the inter-layer spacing as determined from the HRTEM image (See Section 3.2). For theoretical calculations of the Raman modes, the lattice constants have been optimized. The calculated lattice parameters, a=b=3.677 and c=7.947 Å, are consistent with those obtained from the XRD measurements. The small difference between the theoretical and experimental values can occur due to the GGA in the first-principles calculations, which often overestimates the lattice parameters [113]. Figure 4.1(b) schematically illustrates the measurement set-ups for *basal plane* and *edge plane* configurations, where θ is the angle of rotation for the polarization vector as has been discussed later.

4.3.2 Room temperature Raman spectra and mode identification

From the group symmetry analysis, we can express the zone center optical phonon modes of ZrSiS as $\Gamma_{ZrSiS} = 2E_u + 2A_{1g} + 2A_{2u} + 3E_g + B_{1g}$ [114]. Among them, A_{2u} and E_u are IR active, whereas the other six modes ($2A_{1g}$, B_{1g} and $3E_g$) are Raman active. In Figure 4.2(a), the results of Raman measurements at room temperature (297±1 K) are presented for the two configurations of the ZrSiS crystal. The filled area in the figure illustrates the calculated phonon density of states (PDOS). In the *basal plane* measurements, the incident laser beam excites crystallographic *ab*-plane and shows three Raman active phonon modes. On the other hand, to achieve the *edge plane* configuration, we have rotated the crystal by 90° around *b*-axis so that the laser now falls on the crystallographic *bc*-plane. In this set-up, all the six Raman modes have been observed. A comparison between the theoretically calculated PDOS and experimental Raman spectra demonstrates that not all the peaks in PDOS appear in the experimental results, as rest of the calculated modes do not satisfy the selection rules for Raman scattering. To identify the experimentally observed modes, we have theoretically calculated the phonon dispersion for ZrSiS and estimated all the Raman active frequencies at the Brillouin zone center. As shown in Table 4.1, the calculated frequencies are in excellent agreement with the experimentally observed modes. Note that in the *basal plane* configuration, the E_g modes are absent, which can be explained from the lattice symmetry analysis, discussed later. In Figure 4.2(b), we have shown the vibrational patterns corresponding to all six Raman active modes. The A_{1g} modes at 212 and 303 cm^{-1} belong to the anti-symmetric vibration of Zr and S atoms along

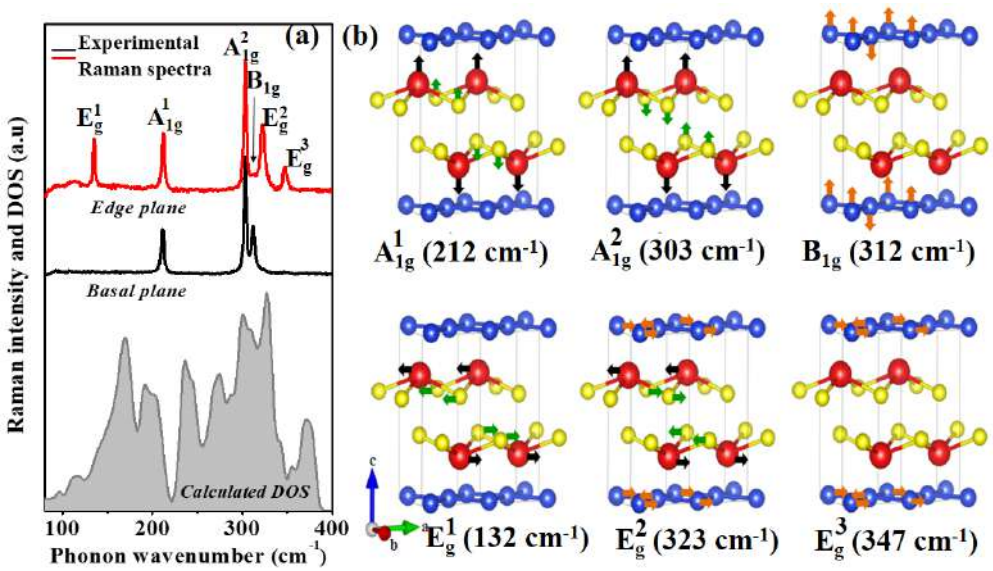

Figure 4.2: (a) Raman spectra of ZrSiS at room temperature for *basal plane* (black curve) and *edge plane* (red curve) configurations. In the lower panel, the shaded region represents the theoretically calculated phonon density of states. (b) Atomic vibration patterns associated to the Raman active modes.

crystallographic c-axis. The vibration of Si atoms along c-axis with frequency 312 cm^{-1} corresponds to B_{1g}. The E_g modes at 132, 323 and 347 cm^{-1} originate from the in plane vibrations of Zr, Si and S atoms.

4.3.3 Polarization and angle-resolved measurements

The polarized Raman spectra have been measured in the backscattering configurations with light polarization along certain crystallographic directions to verify the symmetry of the observed modes. We have used Porto's notation for parallel $[z(xx)\bar{z}$ and $z(yy)\bar{z}]$ and perpendicular $[z(xy)\bar{z}$ and $z(yx)\bar{z}]$ measurement set-ups. Here, z-axis is parallel to the crystallographic c-axis for *basal plane* configuration and antiparallel to crystallographic a-axis for *edge plane* configuration [see Figure 4.1(b)]. The observed polarized Raman spectra of ZrSiS for both configurations

Table 4.1: Comparison of the theoretically calculated and experimentally observed Raman active phonon frequencies for ZrSiS at room temperature (297±1 K)
.

Mode	Calc. Freq. (cm^{-1})	Expt. Freq. (cm^{-1})
A^1_{1g}	212	210±0.5
A^2_{1g}	303	303±0.5
B_{1g}	312	312±0.7
E^1_g	132	134±0.5
E^2_g	323	321±0.5
E^3_g	347	347±0.5

are shown in Figure 4.3. We have detected only the A_{1g} modes, when the measurement was performed in the parallel channels, i.e., $z(xx)\bar{z}$ or $z(yy)\bar{z}$. Whereas, B_{1g} and E_g modes appear for $z(xy)\bar{z}$ or $z(yx)\bar{z}$ polarization configurations. For a particular configuration, the observed small intensity of the forbidden modes is due to the small unavoidable misalignment of the laser polarization vector with crystallographic axis.

The intensity (I) of different Raman modes follows a fundamental relation [115],

$$I \propto | \hat{e_i}.\Re.\hat{e_s} |^2, \tag{4.1}$$

where $\hat{e_i}$ and $\hat{e_s}$ represent the unit polarization vectors of the incident and the scattered light, respectively. $\Re$ is the rank 2 Raman scattering tensor for a particular mode and is obtained from the point group symmetry of the compound. For ZrSiS, with respect to the principal crystallographic axes, the scattering tensors in

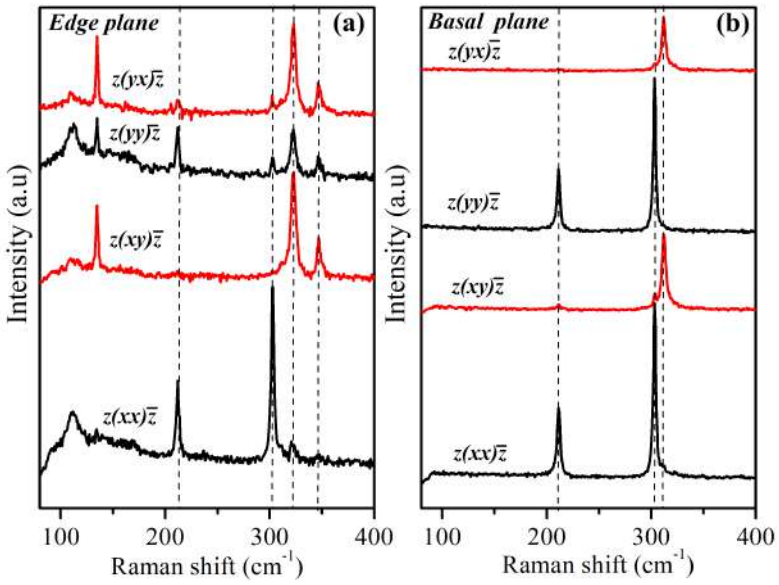

Figure 4.3: Polarized Raman spectra of ZrSiS for (a) *edge plane* and (b) *basal plane* configurations.

bc-plane are as follows,

$$\Re(A_{1g}) = \begin{bmatrix} \alpha & 0 & 0 \\ 0 & \alpha & 0 \\ 0 & 0 & \beta \end{bmatrix}, \Re(B_{1g}) = \begin{bmatrix} \delta & 0 & 0 \\ 0 & -\delta & 0 \\ 0 & 0 & 0 \end{bmatrix}, \Re(E_g) = \begin{bmatrix} 0 & 0 & -\rho \\ 0 & 0 & \rho \\ -\rho & \rho & 0 \end{bmatrix}.$$

The Raman scattering components, α, β, δ, and ρ, can be extracted from the fitting of the experimental data. When the polarization vectors of both the incident and scattered light are parallel to, let's say, the y-axis of an orthogonal xyz-coordinate system, the unit polarization vectors are given by,

$$\hat{e}_{i,xyz} = \begin{bmatrix} 0 & 1 & 0 \end{bmatrix}; \hat{e}_{s,xyz} = \begin{bmatrix} 0 \\ 1 \\ 0 \end{bmatrix}.$$

For *basal plane* configuration, we have to rotate the crystal by 90° around crystallographic *b*-axis. This operation introduces a rotational matrix and modifies the scattering tensors to the following forms.

$$\Re(A_{1g})(basal) = \begin{bmatrix} \beta & 0 & 0 \\ 0 & \alpha & 0 \\ 0 & 0 & \alpha \end{bmatrix}, \Re(B_{1g})(basal) = \begin{bmatrix} 0 & 0 & 0 \\ 0 & -\delta & 0 \\ 0 & 0 & \delta \end{bmatrix},$$

$$\Re(E_g)(basal) = \begin{bmatrix} 0 & \rho & \rho \\ \rho & 0 & 0 \\ -\rho & 0 & 0 \end{bmatrix}.$$

Using these matrices in Equation 4.1, one can find that A_{1g} and B_{1g} modes should be present in *basal plane* configuration, whereas the intensity of the E_g modes must be always zero. As evident from Figure 4.2(a), our experimental observations are consistent with the obtained results from crystallographic symmetries.

Next, we have analyzed the crystal orientation dependent Raman spectrum for ZrSiS in detail. We chose the *edge plane* configuration, as all the phonon modes can be identified in this set-up. To describe the Raman spectra for different crystal orientations and polarization geometry, let us introduce a new orthogonal Cartesian coordinate system (x′y′z′), where the x′-direction coincides with the crystallographic *a*-axis. But, the y′ and z′-directions are at an arbitrary angle (θ) with respect to the crystallographic *b* and *c*-axis, respectively [Figure 4.4]. In this new representation, the Raman scattering tensors undergo the transformation

$$\Re_{x'y'z'} = \Phi_{x'y'z'} \Re \tilde{\Phi}_{x'y'z'}, \tag{4.2}$$

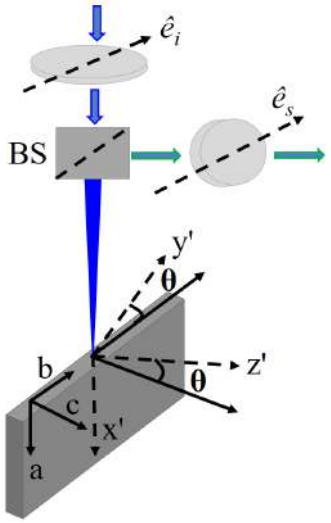

Figure 4.4: Schematic of the measurement set-up for crystal orientation dependent Raman spectroscopy in ZrSiS. The sample is rotated around the crystallographic a-axis, which is equivalent to the rotation of the light polarization vector in the bc-plane.

where $\Phi_{x'y'z'}$ is the orthogonal transformation matrix

$$\Phi_{x'y'z'} = \begin{bmatrix} 1 & 0 & 0 \\ 0 & \cos\theta & \sin\theta \\ 0 & -\sin\theta & \cos\theta \end{bmatrix}$$

and $\tilde{\Phi}_{x'y'z'}$ is its inverse matrix. Inserting these new transformed matrices in Equation 4.1, we have derived the following intensity relations for different Raman active phonon modes.

$$I(A_{1g}) \propto | \, \alpha \cos^2\theta + \beta \sin^2\theta \, |^2 = C_1 + C_2 \cos 2\theta + C_3 \cos 4\theta \tag{4.3}$$

$$I(B_{1g}) \propto | \, -\delta \cos^2\theta \, |^2 = C_4 + C_5 \cos 2\theta + C_6 \cos 4\theta \tag{4.4}$$

$$I(E_g) \propto | \, 2\rho \sin\theta \cos\theta \, |^2 = C_7 - C_8 \cos 4\theta. \tag{4.5}$$

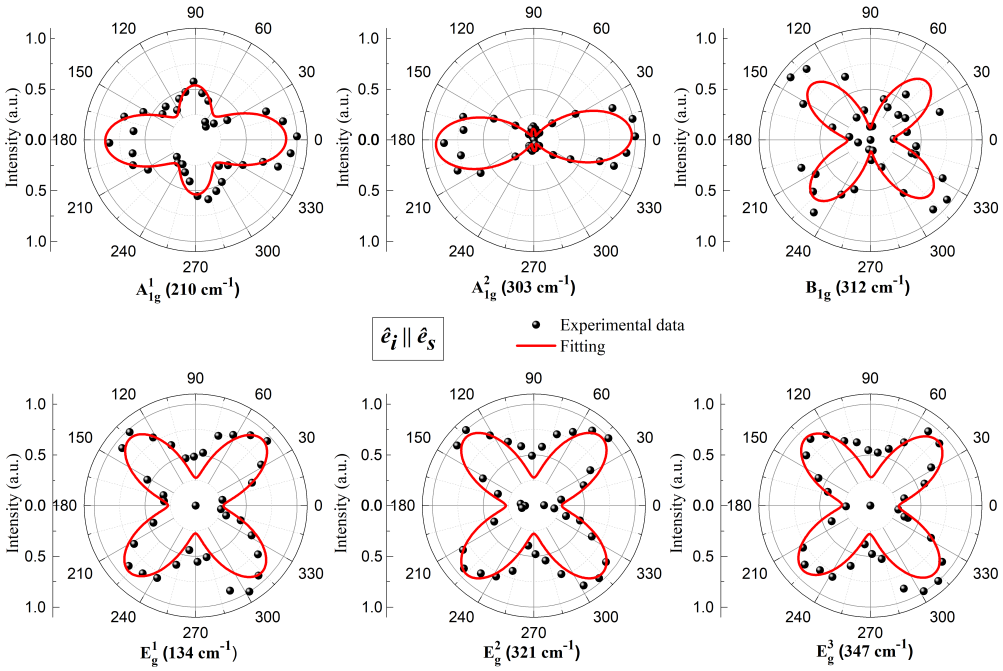

Figure 4.5: Angle dependence of the Raman mode intensities for ZrSiS in parallel configuration ($\hat{e}_i \parallel \hat{e}_s$) on *edge plane*.

Here, the parameters C_i (i=1,2,..8) are the functions of the components of scattering tensors.

To measure the crystal orientation dependent Raman scattering, initially, we have fixed the polarization vectors of both the incident and scattered lights along crystallographic b-axis of ZrSiS. At this point, all the axes of the Cartesian coordinate system coincide with the crystallographic axes, i.e., θ=0. Then, we start to rotate the crystal in the y′z′-plane in small steps and record the intensity variation of different modes. Though this technique is equivalent to the rotation of the polarization vector along crystallographic bc-plane, rotation of the sample has certain advantages. In order to change the direction of the polarization vectors for both incident and scattered lights, we have to use additional optical pieces in the light path and modify their polarization angles at each step. Such measurement

set-up unavoidably introduce experimental uncertainties in the polarization angle and can also modulate the intensity of different Raman modes [116]. In Figure 4.5 (solid points), we have shown the obtained angular dependence of the normalized intensity profile in polar plots for different modes. The experimental data have been fitted well using Equations 4.3, 4.4, and 4.5 (solid red lines in Figure 4.5), which have been derived from the crystal symmetry analysis of ZrSiS.

4.3.4 Wavelength dependent Raman study and signature of electron-phonon coupling

We have also carried out the wavelength dependent Raman measurements in ZrSiS for both *basal plane* and *edge plane* configurations. In Figure 4.6, the result for *basal plane* configuration is shown as a representative. We have observed a definite dependency of the mode intensity on the energy of the incident laser. The integrated intensity of the most intense peak (A_{1g}^2) exhibits the highest value at lowest excitation energy (λ=785 nm, E=1.58 eV) as illustrated in the inset of Figure 4.6. This enhancement originates from the coincidence of the incident laser energy with an intrinsic electronic transition of ZrSiS. The theoretically calculated bulk electronic band structure of ZrSiS [60] reveals that at Γ point, the energy gap is around 1.4 eV, which is also in agreement with the results of reflectivity measurement [117]. Here, with decreasing excitation energy from 2.54 eV to 1.58 eV, the enhancement of the intensity for A_{1g}^2 mode, can be due to the fact that the laser energy is approaching towards the band gap at Γ point. The complex interplay of electronic and phonon degrees of freedom in topological semimetals, results in a quasielastic (QE) scattering [118]. In the excitation energy dependent Raman spectra, instead of the narrow phonon features, we have observed a broad

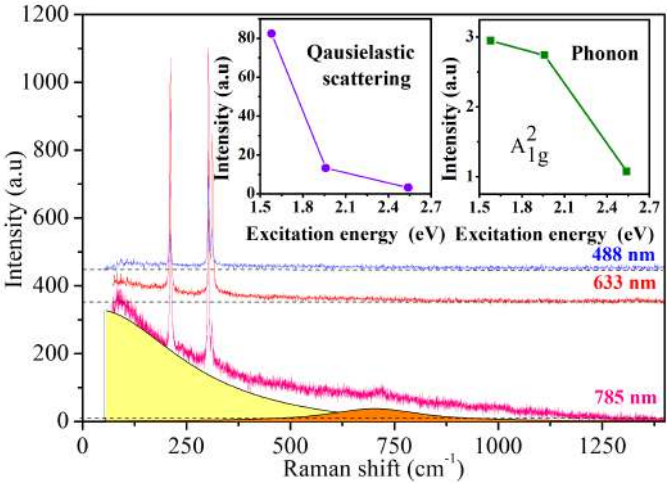

Figure 4.6: Raman spectra of ZrSiS for different incident laser wavelengths in *basal plane* configuration. The background is shown by the black dashed lines. The yellow shaded area corresponds to the fitting of the QE scattering using Lorentzian line shape, whereas the orange shaded Gaussian peak at 703 cm^{-1} for 785 nm laser, is the plasmon maximum. Insets show the excitation energy dependence of the integrated intensity for the QE and phonon scattering (A^2_{1g}).

and well-defined peak in the vicinity of the laser energy (Yellow shaded area in Figure 4.6) in contrast to a flat background. Such feature is reproducible over several measurement cycles on different single crystal of ZrSiS. This peak can be attributed to the QE electronic scattering. Such scattering has also been reported in Dirac semimetal Cd_3As_2 [118]. The line shape of the QE electronic scattering can be fitted well using the Lorentzian function. In semimetals, the electronic energy density fluctuations lead to the Lorentzian shape of QE scattering [119]. As illustrated in the inset of Figure 4.6, the intensity of this QE scattering peak is highly photon energy dependent. We can explain this behavior as a resonant enhancement of the phonon and it occurs, when the scattered photon energy matches with one of the excitonic transition energies [120, 121]. The appearance of resonant enhancement and QE scattering at same excitation energy suggests that both the processes involve same intermediate state. We have also observed a peak with

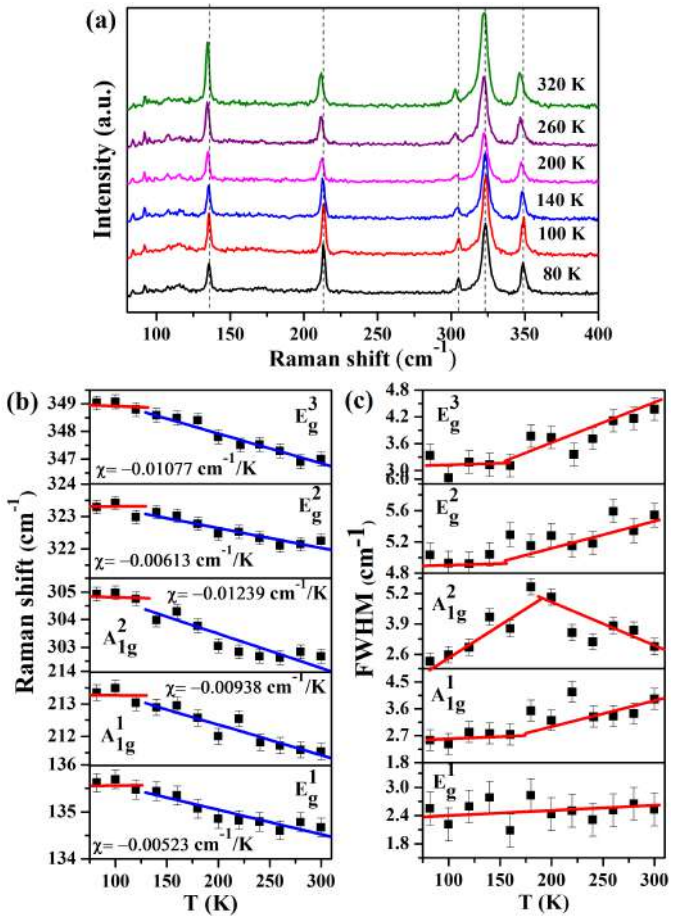

Figure 4.7: (a) Raman spectra of ZrSiS at different temperatures. (b) Frequency and (c) FWHM of characteristic Raman active modes as a function of temperature. The solid lines have been drawn as guide to eyes.

Gaussian line shape (orange shaded area in Figure 4.6) at 703 cm^{-1}, which can be a direct evidence for the single particle or collective (plasmon-like) excitations [118].

4.3.5 Temperature dependent Raman spectroscopy

In Figure 4.7(a), we have presented the temperature dependent Raman spectra for ZrSiS. The obtained results show changes both in frequency and full-width at half-maximum (FWHM) of the phonon modes in the temperature range 80-320 K. All

the Raman spectra have been fitted using Lorentzian functions in order to estimate the frequency shift and line-width of the observed Raman modes in the studied temperature range. Figures 4.7(b) and (c) illustrate the temperature dependence of frequency and line-width of all the modes, except for B_{1g} because the intensity of this mode is very small. The change of peak positions and FWHMs with varying temperature show two different regions roughly below and above 150 K. Though this feature is weak for some phonon modes, it is still detectable and beyond the experimental error. The frequencies of the Raman modes remain almost same in the low-temperature region but monotonically red shifted with increasing temperature. One can not fit such behavior assuming a linear dependence throughout the measured range of temperature. The factors, which cause the temperature dependence of Raman shifts, are thermal expansion and phonon-phonon interaction. Thermal expansion of the material results in the decrease of frequency for the phonon modes. We can express the temperature dependence of ith phonon energy as [122],

$$\omega_{ph,i}(T) = \omega_i(0) + \Delta_i^1(T) + \Delta_i^2(T), \tag{4.6}$$

where $\Delta_i^1(T)$ corresponds to thermal expansion and $\Delta_i^2(T)$ is due to the phonon-phonon interaction. $\omega_i(0)$ is the zero-temperature phonon frequency, which has been obtained by extrapolating the temperature dependent Raman shift. As $\omega_i(0)$ is higher than $\Gamma_i(0)$ (FWHM at zero temperature), the effect of phonon-phonon coupling in ZrSiS must be small in comparison to the shift due to thermal expansion [122]. To analyze the red shift of the phonon modes at higher temperature region, we have taken a linear dependency $\omega_i(T) = \omega_i(0) + \chi_i T$ [blue line in Figure 4.7(b)], where χ_i is the first-order temperature coefficient [123, 124]. Using the extracted χ_i values, the thermal expansion coefficient and isobaric mode-Grüneisen parameter

(γ_{iP}) have been estimated for all the modes and are shown in Table 4.2. The FWHM of the peaks exhibit two different slopes with temperature. Except for A^2_{1g}, all other Raman modes show a constant FWHM at low temperature followed by an abrupt change near 150 K, above which it increases monotonically with increasing temperature. In a perfect crystal, the line-width of the phonon (Γ) is controlled by its interaction with other elementary excitations and can be written as $\Gamma = \Gamma^{an} + \Gamma^{EPC}$. Γ^{an} is the phonon-phonon coupling term, which represents the anharmonic coupling between phonons and Γ^{EPC} corresponds to the electron-phonon coupling [125]. Γ^{an} is always present in a system, whereas Γ^{EPC} comes into play only when the electronic band gap is zero. In ZrSiS, the FWHM values at lower temperatures imply that the contribution from thermal anharmonicity is lower than the resolution of the spectrometer (1 cm^{-1}). The increase in FWHM with temperature can be a signature of increased electron-phonon interaction and thus, an enhancement in phonon energy dissipation [126]. This would lead to increased electron scattering rate and as a result, a change in the nature of temperature dependence of resistivity around 150 K, which we have indeed observed in our transport measurements (See Section 3.3.1). We can also calculate the Fermi velocity of the electrons using the relation [125],

$$v_F = \frac{2Slope(\Gamma)\omega_\Gamma}{\Gamma^{EPC}}. \tag{4.7}$$

Here, $Slope(\Gamma)$ is the slope of phonon dispersion curve, which is extracted from the quadratic fit to the data presented in Figure 4.8 and ω_Γ is the measured phonon frequency at zone center. We have calculated Γ^{EPC} by deducing the maximum possible anharmonicity contribution (spectrometer resolution 1 cm^{-1}) from the obtained FWHM at low temperature. v_F, calculated for all the modes (see Ta-

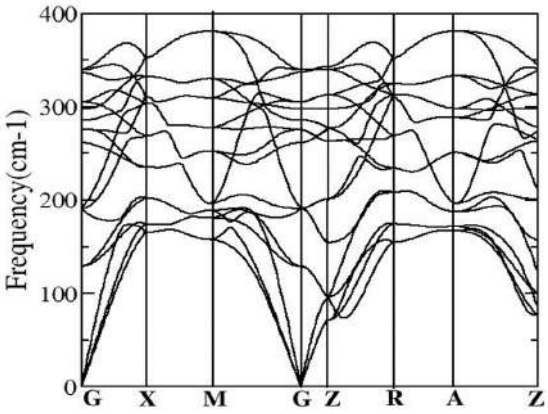

Figure 4.8: Calculated phonon dispersion spectra for ZrSiS.

Table 4.2: Thermal expansion coefficient (α), isobaric (γ_{iP}) and isothermal (γ_{iT}) mode-Grüneisen parameters and Fermi velocity (v_F) for ZrSiS, calculated from the measured Raman spectra.

ω_{ph} cm^{-1}	a_i (cm^{-1}/GPa)	α (10^{-5} K^{-1})	γ_{iP}	γ_{iT}	v_F (10^5 m/s)
134	1.44	1.39 (upto 15 GPa)	2.77	1.23	1.1
210	2.71	1.48	2.96	1.88	0.9
303	2.04	1.43	2.84	0.97	1.7
321	3.36	0.98	1.94	1.51	0.6
347	4.99	1.20	2.48	2.07	2.6

ble 4.2) is in excellent agreement with that estimated from quantum oscillation measurements ($\sim 10^5$ m/s) (See Table 3.1 in Section 3.3.4). From the results of wavelength and temperature dependent Raman measurements, it is evident that in ZrSiS, the lattice dynamics possesses a strong correlation with the changes in the electronic properties.

4.3.6 High-pressure measurements

We have recorded the pressure dependent Raman spectra for the *edge plane* configuration of ZrSiS inside a DAC during the compression as well as decompression cycles up to 57 GPa as shown in Figures 4.9(a) and (b), respectively. During compression, with increasing pressure, all the predominant Raman modes except for E_g^1, have been observed to shift towards higher frequencies as depicted in Figure 4.9(c). E_g^1 mode undergoes a softening ($\sim$1 cm^{-1}) at around $\sim$17 GPa and then begins to harden monotonically with pressure [Figure 4.9(c) inset]. At $\sim$17 GPa, a new band, labeled '1' appears at $\sim$ 148 cm^{-1}. Another two new bands, labeled '2' and '3' emerge by splitting of A_{1g}^1 and E_g^2 at $\sim$5 and $\sim$10 GPa, respectively. Up to the highest applied pressure during compression, the bands '2' and '3' are almost inseparable from the parent modes (A_{1g}^1 and E_g^2). For all the new bands, with increasing pressure, we observed that the frequency increases, intensity reduces and pressure induced broadening occurs. All these observed changes are almost reversible during decompression [Figure 4.9(b)]. The presence of all the parent phase phonon modes along with the newly emerged modes and their smooth pressure dependencies, suggest that the new phase coexists with the parent tetragonal phase. The new high-pressure phases may have been resulted from the lattice distortion and stacking faults, which occur because of the destabilization of the weakly bonded S-bilayers as also reported in layered PbFCl [127] and BaFCl systems [128]. During pressure release, a small peak, marked as '$*$' in Figure 4.9(b), emerges at $\sim$16 GPa. By comparing the peak positions with the ambient condition Raman spectrum, we have concluded that it may correspond to the B_{1g} mode, which is not clearly visible during compression. For the high frequency modes (E_g^2 and E_g^3), the pressure dependencies are almost linear. However, for other modes,

it can be fitted well with quadratic function. We have shown the fitted curves as solid lines in Figure 4.9(c). E_g^1 mode increases monotonically with pressure after softening, whereas above ∼31 GPa, the mode '1' starts to separate faster. We have calculated the pressure derivative (a_i) and the isothermal mode-Grüneisen parameter (γ_{iT}) for all modes using the theoretically estimated bulk-modulus value [114] as shown in Table 4.2. The difference between γ_{iP} and γ_{iT} values is mainly due to the electron-phonon coupling effect, which we did not exclude for the calculation of γ_{iP}. As illustrated in Figure 4.9(d), the FWHM for E_g^1 mode shows an interesting behavior. For E_g^1, FWHM is maximum at ∼15 GPa and it asymmetrically decreases on either side, followed by a steep increment at higher pressure. At around this pressure range, we have observed that (i) a new mode '1' starts to appear (at ∼17 GPa) and (ii) the E_g^1 mode undergoes softening.

To correlate our experimental results, let us discuss the geometric structure of tetragonal ZrSiS, isopuntal with PbFCl [129, 130] and formed by stacking five 4^4 square nets into layers of [..Si_2-Zr-S-S-Zr-Si_2..] along the fourfold axis. Zr atoms build up a part of the double-layer of S atoms and form sheets of square pyramids $[Zr_{5/5}S]_n$, which alternate along crystallographic c-axis with planer Si_{2n} layers [129, 130]. Si atoms are located in layers that are twice denser than S layers, leading to appreciable Si-Si bonding and modest S-S bonding in the unit cell. All the E_g modes correspond to the atomic vibrations, which are confined in ab-plane. Our first-principles calculations reveal that the lowest frequency E_g^1 mode originates from the relative motion of the two adjacent S-layers, while each Zr layer moving in-phase with its nearest-neighbor S layer, i.e., lacks vibrations along c-axis. On the other hand, the A_{1g}^1 mode comes from the asymmetric vibrations related to Zr and S atoms and represents the in-phase motion of S-bilayers with

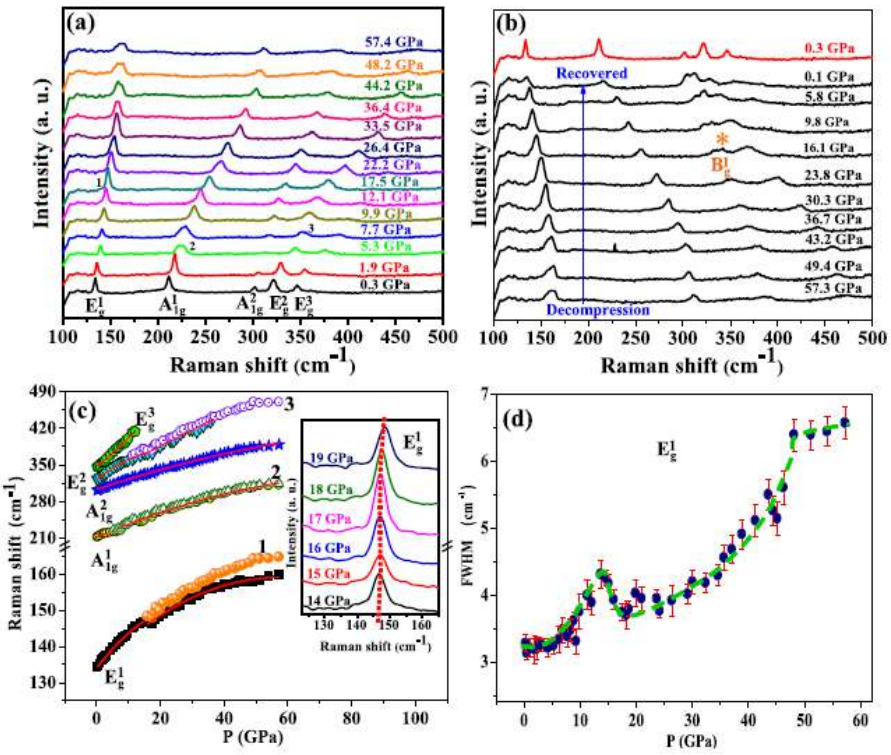

Figure 4.9: Variation of Raman spectrum with pressure up to 57 GPa for ZrSiS during (a) compression and (b) decompression. (c) Pressure dependencies of parent phase modes as well as new modes. Inset shows the softening of E_g^1 mode at around ∼17 GPa. (d) FWHM for E_g^1 mode as a function of pressure during compression. We have drawn the dashed green line as guide to eyes.

Zr-layers on either side. Our calculations on phonon density of states also indicate that only Si and S atoms contribute to the highest optical phonon branches, which are represented by the lowest frequency Raman modes. So, it is expected that E_g^1 and A_{1g}^1 modes (related to S atoms), which correspond to the relative motion between the two weakly bonded Si_2-Zr-S units, would be quite sensitive to inter-layer interactions under an external perturbation such as high pressure. The S-bilayers, involving the stabilizations of the inter-layer arrangements, contribute significantly to E_g^1 and A_{1g}^1 modes in *ab*-plane. We have also observed that under high pressure, low-frequency E_g^1 mode is more susceptible to change than any other

Raman active modes.

The sub-linear pressure dependency of Raman modes indicates that the coupling between the layers increases under external pressure [Figure 4.9(d)]. In contrast to PbFCl, the non-linearity in ZrSiS exists up to the highest applied pressure 57 GPa, suggesting a more rigid structure. This is also supported by their differences in the bulk modulii, 51 and 144 GPa for PbFCl and ZrSiS, respectively [127, 114]. The decrease of FWHM followed by the softening of E_g^1 mode at $\sim$17 GPa is a clear indication of change in the inter-layer bonding nature, i.e., from layer-type to more isotropic structure. Similar asymmetric decrease in FWHM for a low-frequency phonon mode has been reported earlier in a topological insulator system Sb_2Se_3 [131]. The authors have inferred the phenomenon as pressure induced electronic topological transition (ETT) from conventional band to topological insulating state. We note that in ZrSiS, multiple electronic bands are present at the zone center with energy separations comparable to excitations of laser energies to the inter-band transitions. Some topological insulators like BiTeI and Bi_2Se_3 [132, 133] also show similar results. The observed gradual splitting of the A_{1g}^1 mode along with the appearance of modes labeled '1', '2', '3' can be the signature of isostructural symmetry lowering due to the instability occurring in the S-bilayers.

In Figure 4.10, we have shown the synchrotron XRD patterns, recorded as a function of pressure in the range 2.2-30.2 GPa. To index the strongest peaks of the pure tetragonal crystal structure (ICSD File No. 1527641), a theoretically calculated pattern for 1 atm has also been plotted by using the refined lattice parameters, a=b=3.546(2) and c=8.055(4) Å, obtained from our ambient condition XRD data. At 2.2 GPa, the analysis of our HPXRD data, assuming the parent

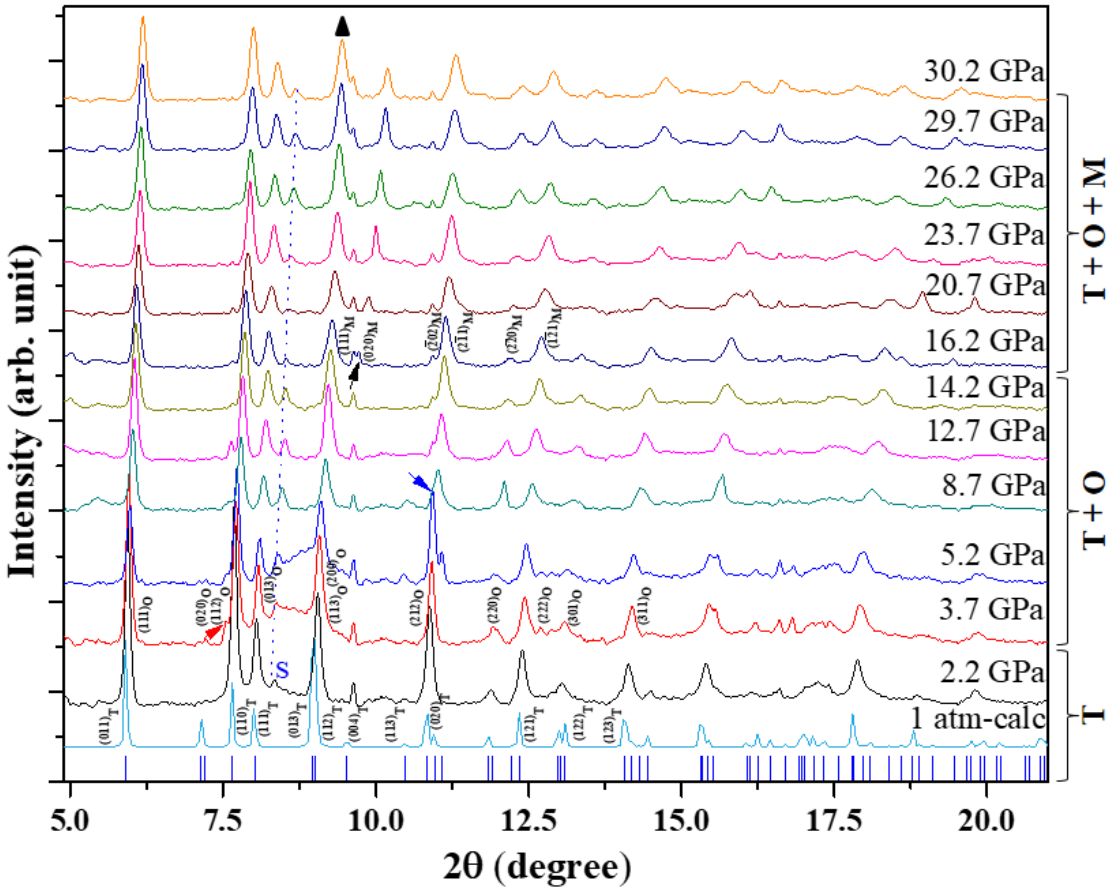

Figure 4.10: The x-ray diffraction patterns with varying pressure. We have plotted the calculated diffraction pattern for the parent tetragonal phase to index the high-pressure phases. The slanted arrows (red, blue, and black) indicate the emergence of new peaks, whereas solid Δ marks the intensity enhancement for a new peak (020) associated with the monoclinic phase. The impurity peak 'S' is from sulfur and tracked throughout the entire pressure region (dashed line). The letters 'T', 'O' and 'M' represent the tetragonal, orthorhombic, and monoclinic phases, respectively. The braces on the right side illustrate approximate phase coexistence of the respective phases during compression.

$P4/nmm$ crystal structure, result in successful indexing of almost all the peaks in the x-ray diffraction pattern except for a weak peak marked as 'S'. We have tracked this peak throughout the measured pressure range (0-30.2 GPa). By careful analysis, we have concluded that the peak-'S' originates from a trace amount of unreacted sulfur on the surface of the ZrSiS crystals, which were crushed to get the powdered sample. Under application pressure, we have observed a number of significant changes, which are marked with arrows in Figure 4.10. Some of these changes can be discernible at and below 5 GPa. Nevertheless, the major parent tetragonal phase is present in significant amount even at highest pressure 30 GPa, as also supported by our pressure-induced Raman spectra. The extensive investigations on the high-pressure structural evolution of the ionic-layered matlokite [127], alkaline-earth halo-fluorides [128, 134], metal-oxide hallides [135] and hydride halides composed of sequence of layers, showed series of symmetry lowering structural transitions from tetragonal to monoclinic phase via the intermediate orthorhombic phase. These results helped us to narrow down the search for the lower symmetry phases in layered structure of ZrSiS. The lattice structure at 3.7 GPa is closely related to tetragonal phase as it can generate all the peaks other than the new peaks. Due to large compressibility along c-axis, the phase must have a smaller c/a ratio than that at ambient conditions and the a or b-axis should be longer than the ambient condition value. Considering these constraints, we have identified the presence of an orthorhombic phase (space group: $Pnma$) with lattice constants a=4.23523, b=4.9869 and c=8.31257 Å at 3.7 GPa, coexisting with the tetragonal lattice a=3.52026 and c=7.97655 Å. In order to index the coexisting phases, we have used LeBail fitting for the XRD patterns at high pressures, considering the refinements of lattice parameters and without any refinements of the

atomic positions. For the orthorhombic phase, we have taken the atom positions of the $BaBr_2$-type structures (ICSD File No. 1527183) as an initial guess considering the fact that ZrSiS crystallizes in this type at high-pressure [136]. The peaks corresponding to the orthorhombic phase are indexed in Figure 4.10, whereas all the other intense peaks have been obtained from the parent $P4/nmm$ structure. The pressure-induced lattice compression as well as the coexistence of phases can be the reasons for the changes in the Raman modes (A^1_{1g} and E^2_g) at around 5 GPa. A small shoulder peak to the left of $(020)_T$ - $(212)_O$ (indicated by the blue arrow in Figure 4.10) appeared at ∼8.7 GPa. With increase in pressure, the peak is clearly visible till 30 GPa. A new peak appeared just right to the $(004)_T$ peak at around 16 GPa. The intensity of this new peak increases with increasing pressure. While all the peaks from the tetragonal and orthorhombic phases are clearly identified, the new peaks can not be indexed by either of these two phases. Our analysis at ∼16 GPa shows the mixture of three phases; a tetragonal parent phase along with coexisting orthorhombic and monoclinic phases. The XRD data analysis confirms that the coexistence of these three phases persists up to the highest applied pressure 30 GPa. We can index the newly emerged peak as $(020)_M$ of monoclinic phase (space group: $P2_1/m$) with lattice parameters a=7.81417, b=3.56305, c=3.56305 Å, and β=107.045°. This monoclinic structure is identical to the one reported for BaFCl [128]. Similar type of gradual increase in intensity with pressure has also been reported for BaFBr and BaFCl systems starting from 22 GPa to 60 GPa [128, 137]. The authors inferred that the phase transition corresponds to the gradual distortion of the tetragonal structure to a monoclinic phase via an intermediate orthorhombic phase. In layered transition-metal dichalcogenides [138, 139], the structural phase transition along with an increase of intensity for a particular

peak can be explained from the changes in Wyckoff's positions of the atoms, related c/a ratio and the variation in chalcogen-metal-chalcogen bond-angles. Our XRD spectra highly correlate the observed softening of the E_g^1 phonon mode at around 17 GPa. As discussed already, the interlayer arrangements of S-bilayers contribute to the E_g^1 phonon mode in ab-plane. We infer that because of the high c-axis compressibility, there can be a large compression of the electron charge density of the S-ions along that axis between the adjacent weakly bonded S-layers. Therefore, the anisotropic distribution of such charge density in the crystallographic ab-plane started to distort the lattice structure during compression. At high pressure above 16 GPa, the tilting of either orthorhombic or tetragonal lattice in the ab-plane with respect to c-axis may cause the orthorhombic to monoclinic phase transition. The consequence of such lattice distortions clearly supports our results of pressure dependent Raman measurements. In Figure 4.11(a), we have shown the variation of the lattice parameter c of the parent tetragonal lattice with applied pressure. The discontinuity of $\sim$0.3 Å at $\sim$18.7 GPa, is a clear evidence of the growing instability in the parent lattice. Though the signature of the monoclinic phase appears below 18.7 GPa, it is possible that we can observe the measurable discontinuity in the lattice parameters, when a sufficient amount of monoclinic phase sets in. As shown in Figures 4.11(b) and (c), we have not found any discontinuity in the pressure dependence of lattice parameter a as well as the calculated normalized unit cell volume (V/V_0) for the tetragonal phase. The unit cell volume gradually decreases with increasing pressure without showing any volume collapse. The observed smooth and sluggish nature of the phase transition is caused by the small difference in the Gibbs free energy among these three phases [127, 140]. Assuming the tetragonal phase for entire pressure range 0-30 GPa, we have used a third order

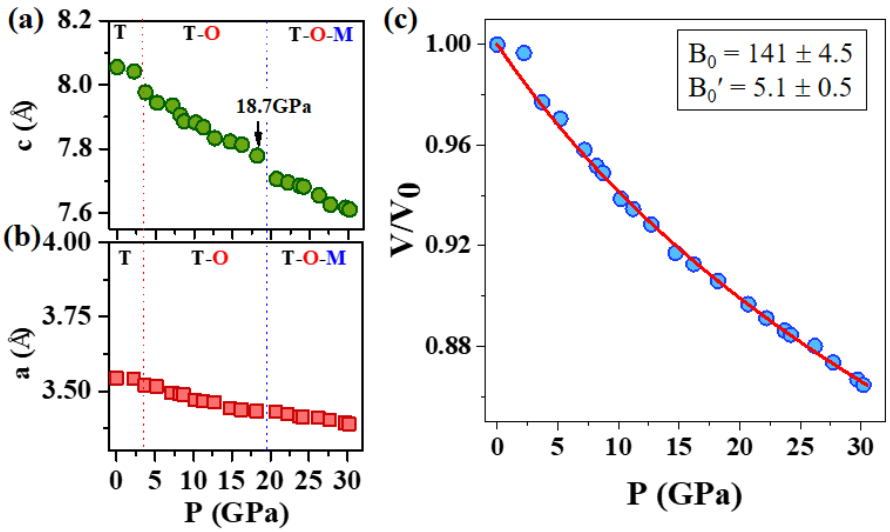

Figure 4.11: (a) Lattice parameter c for the tetragonal phase as a function of pressure. The discontinuity in the same is marked with arrow at 18.7 GPa. Pressure dependence of (b) lattice parameter a and (c) the normalized volume of the tetragonal phase (V/V_0). The solid line in (c) shows EOS, which yields the values B_0=141±4.5 GPa and B_0'=5.1±0.5. The letters 'T', 'O' and 'M' represent the tetragonal, orthorhombic and monoclinic phases, respectively.

Birch-Murnaghan equation of state (EOS) to fit V/V_0 with pressure. The obtained bulk-modulus, B_0=141±4.5 GPa with pressure derivative B_0'=5.1±0.5, agrees very well with the theoretically calculated value 144 GPa [114]. The system appears hard to compress in comparison to ZrSiTe and ZrSiSe [114].

4.4 Summary and conclusions

To summarize, we have carried out a systematic Raman spectroscopy study on single crystalline ZrSiS. To probe all the Raman active phonon modes, the measurements have been performed along two crystallographic planes. We have conducted the first-principles calculations to identify the observed modes and the corresponding atomic vibrational patterns. The results of polarization and crystal rotation

dependent Raman measurements, further verify the mode identification and also provide fundamental information about the structural symmetries of the material. The temperature and excitation energy variation studies reveal resonant enhancement of phonon and quasielastic electronic scatterings, which are the signatures of complex electron-phonon interaction. Furthermore, the high-pressure Raman spectra show vibrational anomalies and the emergence of new modes, suggesting possible structural transitions. From the structural analysis, we infer that such modification in crystal structure may also lead to electronic topological transition, as observed in several topological materials. The high-pressure synchrotron x-ray diffraction data show very interesting pressure-induced structural transition from tetragonal to monoclinic phase through an intermediate orthorhombic phase with the absence of any volume collapse. The coexistence of all three phases up to the highest applied pressure (30 GPa) as well as the structural transformations, are in agreement with the high-pressure Raman spectroscopy results.

5

Magnetotransport properties and evidence of topological insulating state in LaSbTe

5.1 Introduction

Following the theoretical prediction [59] of 2D TI state in *WHM* family, only ZrSnTe has been confirm to host TI surface states [91], whereas TNLS state has been observed in several members of this group [60, 92, 94]. In this chapter, we have investigated the magnetotransport and magnetization properties of single crystalline LaSbTe. Our experimental results reveal compensated electron-hole density with very high carrier mobility in LaSbTe. The observed magnetic field-induced resistivity upturn and large MR are analyzed both from the viewpoints of possible metal-semiconductor-like transition and Kohler scaling. The Fermi surface parameters have been calculated from the de Haas-van Alphen oscillation. In the low-field region of the magnetization measurement data, a robust paramagnetic singularity has been observed, which originates from the spin-polarized non-trivial

surface state. Our results thus confirm a topological insulating phase in LaSbTe, which is in accordance with the theoretical prediction [59].

5.2 Sample preparation, characterization, and experimental details

The single crystals of LaSbTe were grown using the molten-salt flux method [141]. A mixture of LiCl (Alfa Aesar 99.9%) and RbCl (Alfa Aesar 99.8%) in 55:45 molar ratio was used as the flux. The chloride salt mixture along with stoichiometric amount of La (Alfa Aesar 99.9%), Sb (Alfa Aesar 99.9999%) and Te (Alfa Aesar 99.999%) were taken in an alumina crucible which was then sealed in a quartz tube under vacuum. The quartz tube was heated to 700°C and kept at this temperature for 5 days. After that, the furnace was cooled slowly (2°C/h) to room temperature. Shinny single crystals were obtained which were washed with water to remove the chloride salt and cleaned with acetone. The crystals were characterized using XRD and HRTEM. Transport measurements were performed in a 9 T PPMS with ac transport option on several single crystal samples from the same batch, all shaped into thin rectangular bar geometry. Magnetic measurements were done in a 7 T SQUID-VSM MPMS3. Before performing the magnetic measurements on LaSbTe samples, we have measured the empty sample holders to ensure the absence of any contamination. The obtained data are more than two orders of magnitude smaller than that obtained with LaSbTe.

In the inset of Figure 5.1(a), a single crystal of LaSbTe of typical dimensions $2\times1\times0.6$ mm^3 is shown with different crystallographic axes, along which transport and magnetization measurements have been done. The XRD pattern of powdered

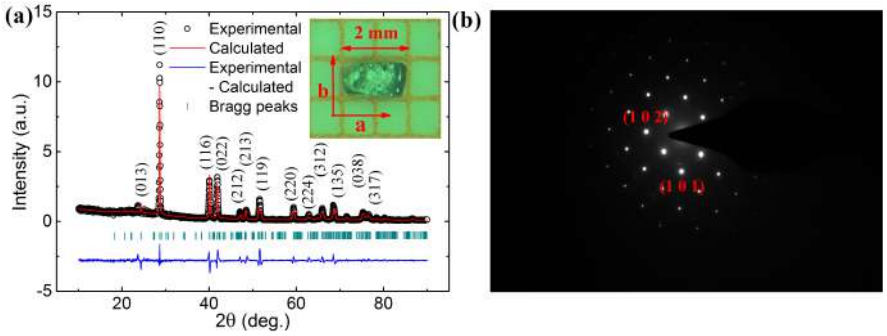

Figure 5.1: (a) Powder XRD pattern of the LaSbTe single crystals. Inset shows a typical single crystal. (b) SAED pattern obtained in HRTEM measurement.

single crystals is illustrated in Figure 5.1(a). The sharp diffraction peaks with small FWHM confirm the high quality of the grown crystals. The XRD pattern has been analyzed by Rietveld structural refinement using FULLPROF software package. LaSbTe crystallizes in a ZrSiS type structure and belongs to orthorhombic space group *Pmcn* [141, 142]. The refined lattice parameters calculated from XRD spectra, **a**=4.3903(2), **b**=4.4293(3) and **c**=19.4858(3) Å, are consistent with previous report [141]. The SAED pattern obtained in HRTEM is shown in Figure 5.1(b) with the Miller indices of the corresponding lattice planes.

5.3 Results and discussions

5.3.1 Temperature dependence of resistivity and low temperature resistivity plateau

In Figure 5.2(a), the resistivity of two samples from the same batch is shown as a function of temperature. Resistivity of both samples exhibits similar temperature dependence, decreasing almost linearly from 300 K down to 125 K and show weak temperature dependence below 30 K. The resistivity at 2 K is as low as ∼9 $\mu\Omega$ cm

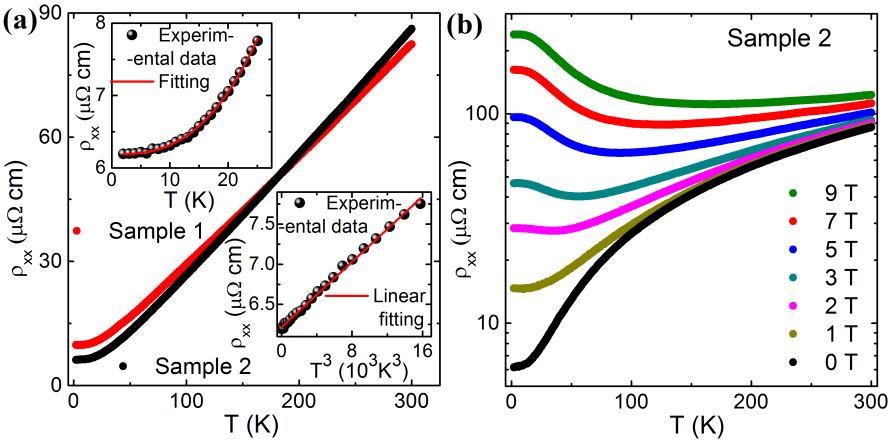

Figure 5.2: (a) Temperature dependence of resistivity for two samples from the same batch. The top inset shows the low-temperature region fitted with $\rho_{xx}(T) = A + BT^n$. The low-temperature resistivity is plotted with T^3 in the bottom inset. (b) $\rho_{xx}(T)$ under different transverse magnetic field strengths.

for sample 1 and ∼6 $\mu\Omega$ cm for sample 2, which are comparable to that reported for Dirac semimetal Cd_3As_2 and Weyl semimetals TaAs, NbP and TaP [69, 76, 143, 144]. The calculated residual resistivity ratio [RRR=ρ_{xx}(300 K)/ρ_{xx}(2 K)] for both the samples (sample 1 ∼8.4; sample 2 ∼14), suggests good metallicity of the grown LaSbTe crystals. For both the crystals, the low-temperature resistivity can be fitted well [Figure 5.2(a) inset] with $\rho_{xx}(T)$=$A + BT^n$ type relation for n∼3, where A and B are constants. As discussed earlier, deviation from a value n=2 is generally considered as a departure from the pure electronic correlation dominated scattering mechanism [64] and can be attributed to interband electron-phonon scattering [65, 66, 67, 68].

When a magnetic field is applied, resistivity is observed to increase rapidly, particularly in the low-temperature region [Figure 5.2(b)]. Above a critical value of the magnetic field ∼1 T, the resistive behavior of LaSbTe at low temperature modifies significantly. The nature of the slope of the $\rho_{xx}(T)$ curve changes and a metal-semiconductor-like crossover appears. Similar upturn in low-temperature

resistivity has been observed in several TSMs [65, 66, 69, 143]. In analogy to dynamical chiral symmetry breaking in the relativistic theory of (2+1)-dimensional Dirac fermions, Khveshchenko proposed that this type of magnetic field-induced crossover is due to the gap opening at the band crossing points [145]. However, subsequent explanations in terms of scaling analysis, have also been proposed [72, 73, 146]. Here, we have adopted both the approaches to discuss the resistivity turn-on behavior in LaSbTe. As discussed earlier, $\rho_{xx}(T)$ can be analyzed considering the thermal activated transport. In Figure 5.3(a), we have plotted $\ln\rho_{xx}$ as a function of T^{-1}. From the slope of the curve, the thermal activation energy gap $E_g \sim 2.6$ meV has been calculated at 9 T, which is quite small. As discussed in Chapter 3, the value of this calculated energy gap strongly depend on the temperature range over which the slope has been taken. Figure 5.3(b) illustrates that the energy gap is a function of the magnetic field.

Above the critical magnetic field, the crossover in the $\rho_{xx}(T)$ curve is followed by a plateau at low temperature. Although, the field-induced resistivity plateau has been observed in several topologically non-trivial semimetallic systems [65, 66, 69, 73, 143], its origin is not yet settled unambiguously. Very similar temperature-dependent resistivity has been observed in topological insulators Bi_2Te_2Se and SmB_6 in absence of magnetic field, where the low-temperature saturation-like behavior in resistivity arises due to the competition between conducting surface and insulating bulk states [147, 148]. On the other hand, the field-induced resistivity plateau in LaSbTe appears in the broken time-reversal symmetry scenario. In Figure 5.3(c), the first-order derivative of the resistivity $\partial\rho_{xx}/\partial T$ is plotted as a function of temperature for different magnetic field strengths. As shown in the inset, from the resultant curves, two distinct char-

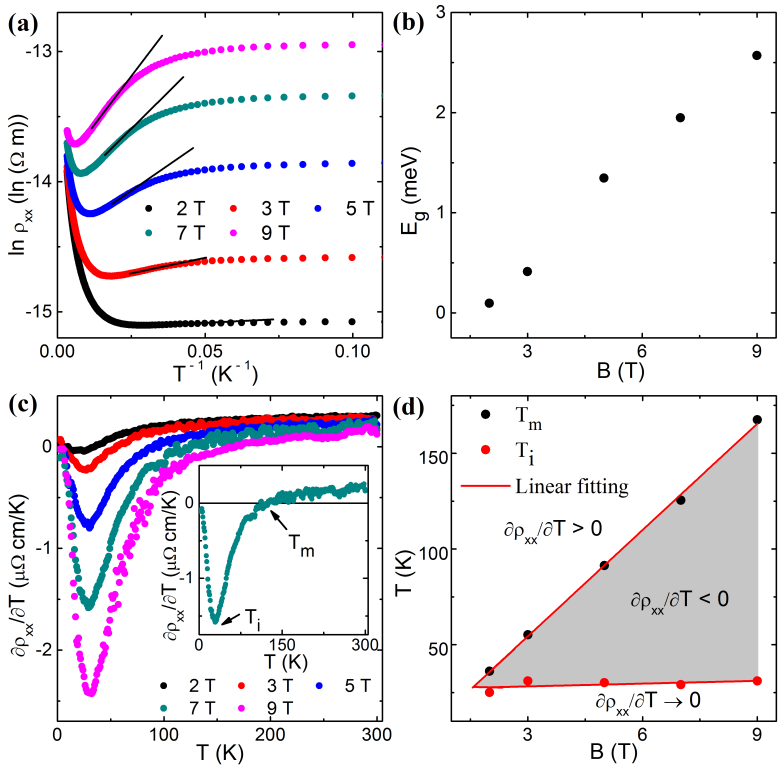

Figure 5.3: (a) lnρ plotted as a function of T^{-1}. (b) Field dependence of the calculated thermal activation energy gap. (c) $\partial\rho_{xx}/\partial T$ plotted as a function of temperature for different applied field strengths. Inset shows the crossover temperature T_m and plateau temperature T_i for 7 T. (d) Triangular temperature-field phase diagram constructed from T_m and T_i.

acteristic temperatures can be identified, the crossover temperature T_m, where $\partial\rho_{xx}/\partial T$ changes sign and T_i, below which the resistivity plateau starts to appear. While T_m increases monotonically with field, T_i is almost field independent. In Figure 5.3(d), following the approach of Tafti *et al.* [75], we have constructed a triangular temperature-field phase diagram for LaSbTe by plotting T_m and T_i as a function of magnetic field. This triangular phase diagram has been seen to be universal for all semimetallic systems showing extreme magnetoresistance [75]. In Figure 5.3(d), the gray shaded area which corresponds to $\partial\rho_{xx}/\partial T$<0, denotes the region, where extreme magnetoresistance (XMR) occurs. The linear fitted curves

of $T_m(B)$ and $T_i(B)$ merge at $B_0 \sim 1.6$ T, which is precisely the turn-on field above which metal-semiconductor-like crossover appears. The region above the shaded triangle with $\partial\rho_{xx}/\partial T > 0$ is of metallic conduction and negligible MR, whereas the area below the shaded triangle denotes the plateau region ($\partial\rho_{xx}/\partial T \to 0$). As has been seen in bismuth and graphite [146], the triangular region in the temperature-field phase diagram can be specified by the inequality, $\hbar/\tau \lesssim \hbar\omega_c \lesssim k_B T$, where τ is the electron-phonon scattering time and ω_c is the cyclotron frequency. In clean semimetals with low carrier density, $\tau^{-1} \ll k_B T/\hbar$ and hence, there exists a wide temperature-field range where XMR and metal-semiconductor-like crossover in resistivity appear. On the other hand, large carrier density and strong impurity scattering, limit the MR in conventional metals [149].

5.3.2 Large and anisotropic magnetoresistance

Next, we have measured the TMR. In Figure 5.4(a), the MR for two samples is compared at 5 K with current along a- and field along c-axis. It is clear that the sample with higher RRR (sample 2) shows stronger response to magnetic field than the other one (sample 1). Therefore, the value of MR clearly depends on the RRR. However, the MR for both the samples is observed to follow same power-law behavior, MR$\propto B^m$ with $m \sim 1.6$. In Figure 5.4(b), we have plotted MR at different temperatures for sample 2 as a representative. At 2 K and 9 T, a large MR $\sim 4\times10^3$ % is obtained without any signature of saturation. Though the observed MR is not among the largest reported so far, it is comparable to that observed in several topological semimetals [144, 150, 151, 152]. With the increase in temperature, however, the MR decreases rapidly to only $\sim$35 % at 300 K and 9 T. As shown in

Figure 5.4(c), employing the Kohler's rule,

$$MR = \alpha(B/\rho_0)^m, \tag{5.1}$$

with α=4.8×10^{-9} (Ω cm/T)$^{1.6}$ and m=1.6, the MR curves at different temperatures can be scaled to a single curve. According to semiclassical two-band theory, the validity of Kohler rule with MR$\propto(B/\rho_0)^2$ suggests a perfectly compensated system [64]. In LaSbTe, however, the exponent is not exactly 2 and as a result a small deviation from scaling in Figure 5.4(c) is observed at high temperature. The deviation becomes more prominent for temperature above 100 K. Several aspects [73, 77], including different densities and or temperature dependence of mobility for two types of carriers may lead to the violation of Kohler scaling in LaSbTe, which will be discussed later. Adopting a modified form of Equation 5.1,

$$\rho_{xx}(B) = \rho_0 + \alpha B^m/\rho_0^{m-1}, \tag{5.2}$$

it can be shown that the resistivity in a magnetic field consists of two components, zero-field resistivity ρ_0 and field-induced component $\Delta\rho_{xx}$=$\alpha B^m/\rho_0^{m-1}$. The competition between these two terms may give rise the observed minimum in the temperature dependence of resistivity above the critical field. In Figure 5.4(d), the field-induced resistivity component is plotted for different magnetic fields. As illustrated by the solid lines, the experimental data for all magnetic fields, can be described well by Equation 5.2 with α=4.8×10^{-9} (Ω cm/T)$^{1.6}$ and m=1.6. In fact, MR at different magnetic fields, collapses onto a single curve when normalized by their respective values at 2 K [Figure 5.5(a)]. This suggests that the temperature dependence of MR remains same for all magnetic fields. On the other hand, the

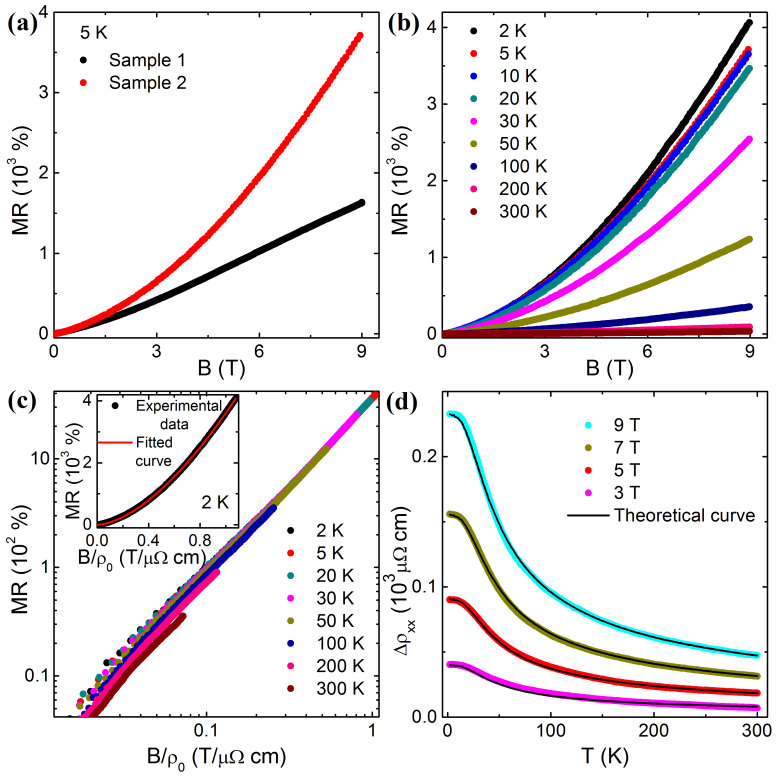

Figure 5.4: (a) TMR for sample 1 and sample 2. (b) TMR for sample 2 at different representative temperatures. (c) MR at different temperatures are scaled using Kohler's rule (Equation 5.1). Inset shows the power-law fitting of the experimental data. (d) Field-dependent part of ρ_{xx}(T). Solid lines denote the curves generated from Kohler's rule.

calculated thermal activation energy gap has been observed to increase monotonically with field. So, sharper metal-semiconductor-like crossover is expected at higher magnetic fields. Therefore, the validity of such scaling behavior, seems to be contradictory to the picture of possible field-induced gap at the band crossing points. Moreover, the gap opening model has several shortcomings. For example, the calculated small energy gap (∼2.6 meV) corresponds to a temperature ∼25 K. However, the semiconductor-like behavior persists up to a temperature as high as ∼150 K. In addition to that, no change in Hall resistivity has been observed through out the measured temperature range. As α and m are temperature-

independent constants, Equation 5.2 suggests that the temperature dependence of $\Delta\rho_{xx}$ is determined entirely by $\rho_0(T)$, which is again inversely proportional to the density and mobility of the charge carrier. Therefore, in a system where carrier density remains constant with temperature, the resistivity turn-on behavior may result from strong temperature dependence of the carrier mobility [73, 146]. In spite of being conflicting, both metal-semiconductor crossover [65, 153] and Kohler scaling analysis [72, 73, 146] are used simultaneously and can explain the observed transport behavior to some extent. However, the actual origin remains an open question, which has yet to be answered decisively.

For in-depth understanding of magnetotransport properties of LaSbTe, we have measured the MR by tilting the magnetic field along different crystallographic directions while keeping the current direction unaltered. The experimental configuration is shown schematically in the inset of Figure 5.5(b) with current along a-axis and magnetic field rotated within the bc-plane. As we increase the angle (θ) from 0° to 90°, MR is seen to increase and then decreases with further increase of θ beyond 90°. Maximum MR $\sim 5\times10^3$ is recorded at $\theta \sim 90°$ ($\mathbf{B}\|b$). In Figure 5.5(c), MR for two different field strengths, is plotted as a function of the tilting angle. The resultant curve possesses a two-fold rotational symmetry, indicating considerable anisotropy in the magnetotransport properties in LaSbTe. Anisotropic MR has also been reported in other members of the *WHM* family [92, 93, 94]. The MR in ZrSiS and ZrSiSe shows strong anisotropy and butterfly-like angular dependence. [93, 94]. On the other hand, the MR in ZrSiTe exhibits a two-fold symmetric pattern, which is similar to the present system [94].

We have also measured the MR with current along a-axis and magnetic field is rotated within the ac-plane. As shown in the Figure 5.5(d), the MR becomes

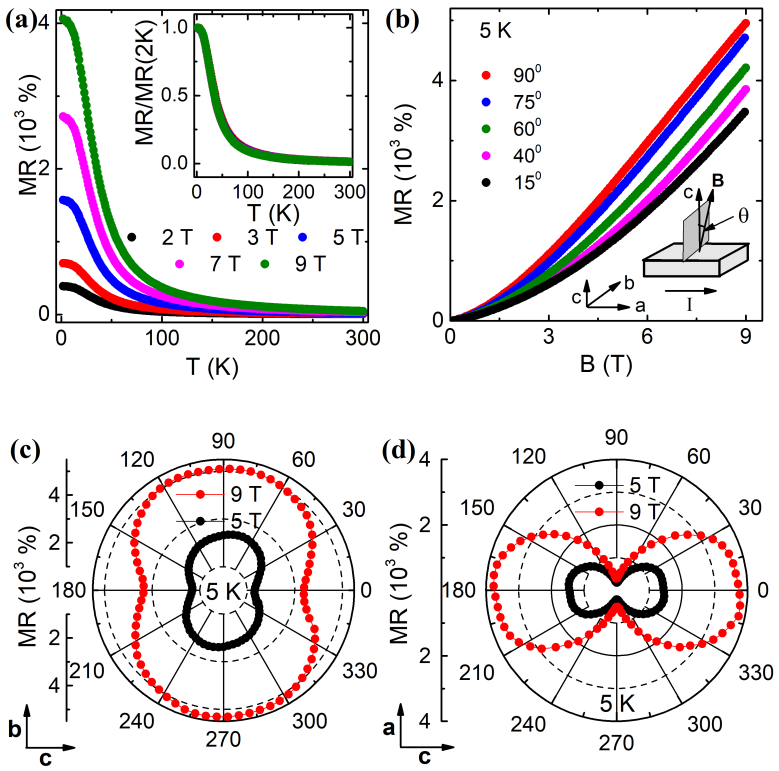

Figure 5.5: (a) Temperature dependence of MR. Inset shows the normalized MR with the value at 2 K. (b) MR as a function of magnetic field at 5 K when $\boldsymbol{B}$ is tilted along different crystallographic directions. Inset shows the schematic of the experimental setup. (c) Polar plot of TMR for two different field strengths with current along a-axis and magnetic field rotated in the bc-plane. (d) Angular dependence of MR with current parallel to a-axis and field rotated in the ac-plane.

minimum when electric and magnetic fields are parallel to each other (φ=90°; $\mathbf{B}\|a$), which is expected due to the absence of Lorentz force in such a configuration. MR increases monotonically as the angle decreases from 90° to 0°. For both the angle variation measurement configurations, weak but detectable kinks have been observed symmetrically at certain angles (at 60° and 240° for field rotated in the bc-plane; at 165° and 345° for field rotated in the ac-plane). They may be due to some higher order texturing, which has also been reported in another isostructural compound ZrSiS [93].

5.3.3 Hall measurement

To determine the nature and density of the charge carriers, we have performed the Hall resistivity measurement in the temperature range 10-300 K. In Figure 5.6(a), the measured Hall resistivity (ρ_{yx}) is plotted as a function of magnetic field. At 300 K, ρ_{yx} is found to be almost linear and positive, which indicate hole-dominated charge conduction. However, with decreasing temperature, $\rho_{yx}(B)$ becomes sublinear and, around 100 K, its sign changes from positive to negative at high fields. The magnetic field dependence of ρ_{yx} clearly shows that more than one type of charge carrier is present in LaSbTe. From the high-field slope of the $\rho_{yx}(B)$ curves, the Hall coefficient has been determined and shown in Figure 5.6(b) as a function of temperature. Following the semiclassical two-band model [76, 89], we have fitted the Hall conductivity σ_{xy} in Figure 5.6(c) using,

$$\sigma_{xy} = \left[n_h \mu_h^2 \frac{1}{1+(\mu_h B)^2} - n_e \mu_e^2 \frac{1}{1+(\mu_e B)^2} \right] eB, \tag{5.3}$$

where $\sigma_{xy}=\frac{\rho_{yx}}{\rho_{yx}^2+\rho_{xx}^2}$ has been obtained from the tensorial inversion of the resistivity matrix. From the fitting parameters, the electron and hole densities at 10 K are found to be, $1.5(3)\times10^{19}$ and $1.2(2)\times10^{19}$ cm^{-3} respectively, which indicate near-perfect electron-hole carrier compensation in LaSbTe. The obtained electron and hole mobilities are large and at 10 K are $\sim3.7(1)\times10^{3}$ and $\sim1.9(2)\times10^{4}$ cm^2 V^{-1} s^{-1} respectively, which are comparable to the carrier mobility observed in Dirac semimetals Cd_3As_2, $ZrTe_5$, TlBiSSe and Weyl semimetal WTe_2 [85, 150, 154, 155]. As shown in Figure 5.6(d), the mobility for both types of carriers decreases as the temperature increases. The inset of Figure 5.6(d) illustrates the temperature dependence of the extracted carrier density for both electrons and

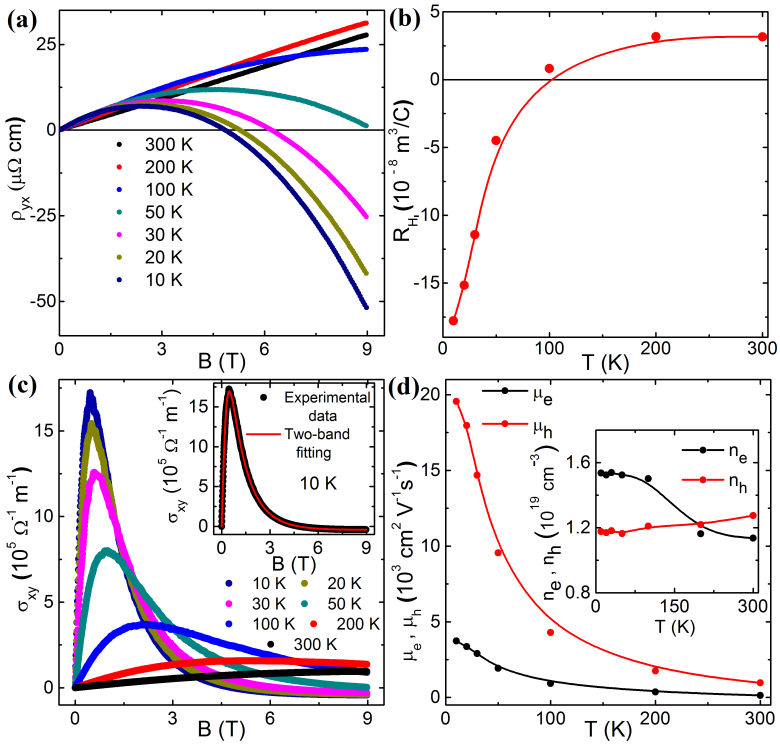

Figure 5.6: (a) Field dependence of the Hall resistivity at different temperatures. (b) Temperature dependence of the Hall coefficient obtained from the slopes of $\rho_{yx}(B)$ curves in the high-field region. At about 100 K, the Hall coefficient changes sign from positive to negative. (c) The Hall conductivity plotted as a function magnetic field. Inset shows the two-band fitting of the Hall conductivity at 10 K using Equation 5.3. (d) Temperature dependence of electron and hole carrier mobility obtained from two-band fitting. Inset shows the extracted carrier densities as a function of temperature.

holes. While the carrier densities remain almost same throughout the temperature range, the mobility shows strong temperature dependence and it is different for the two types of charge carriers. Due to the uncertainties in the numerical values of the parameters obtained from the two-band fitting, Figure 5.6(d) provides only a qualitative information about two types of carriers. At temperature above ∼100 K, the mobilities for electrons and holes become comparable and both types of carriers start to contribute significantly to the transport properties. This behavior is reflected in the Kohler scaling analysis, where the MR curves have been seen to

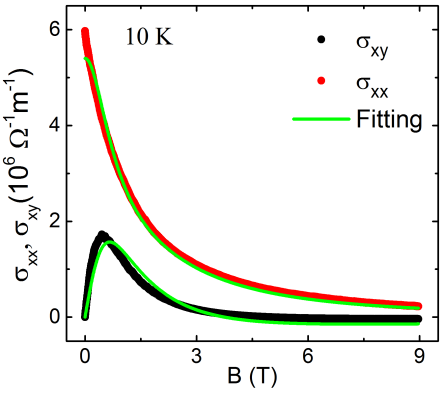

Figure 5.7: Global fitting of the Hall conductivity and longitudinal conductivity using two-band model [Equations 5.3 and 5.4].

deviate from the scaling at higher temperature.

To verify the results obtained from Hall resistivity, we have also analyzed the longitudinal conductivity ($\sigma_{xx} = \frac{\rho_{xx}}{\rho_{xx}^2+\rho_{yx}^2}$) using the two-band model [76, 156],

$$\sigma_{xx} = e\left[n_h\mu_h\frac{1}{1+(\mu_h B)^2} + n_e\mu_e\frac{1}{1+(\mu_e B)^2}\right]. \tag{5.4}$$

In Figure 5.7, we have shown the global fitting of σ_{xy} and σ_{xx}, i.e., these two quantities have been fitted simultaneously using Equations 5.3 and 5.4 to enhance the reliability of the extracted parameters. The obtained electron [hole] density $\sim$2.5(3)$\times10^{19}$ cm^{-3} [$\sim$1.9(5)$\times10^{19}$ cm^{-3}] and mobility $\sim$3.3(1)$\times10^{3}$ cm^2 V^{-1} s^{-1} [$\sim$1.2(8)$\times10^{4}$ cm^2 V^{-1} s^{-1}] at 10 K, are in good agreement with those calculated from the Hall measurements.

5.3.4 de Haas-van Alphen oscillation and Fermi surface topology

We have performed the magnetization measurement on the LaSbTe single crystals with magnetic field along c-axis. The field dependence of the magnetization data shows a diamagnetic behavior with prominent dHvA oscillation up to 10 K. Above this temperature, the thermal scattering of the carriers starts to dominate and the oscillations quickly wash out. To extract the oscillatory component (ΔM), we have subtracted a smooth background from the magnetization data and plotted in Figure 5.8(a) as a function of $1/B$. The corresponding FFT spectrum in the inset, shows a single frequency $\sim$55(1) T. From the Hall resistivity data, it is evident that there are one electron-type Fermi pocket and one hole-type Fermi pocket in LaSbTe. However, as the density of charge carrier for both the Fermi pockets is almost equal, their volume is expected to be equivalent. In addition, the weak anisotropy in the angular dependence of MR indicates nearly spherical geometry of the Fermi pockets. So, the cross-sectional areas of the Fermi pockets must be almost equal and as a consequence, it is difficult to distinguish them through quantum oscillation measurements. Similar behavior has also been observed for Dirac semimetal Cd_3As_2, where two equivalent ellipsoidal Fermi pockets result in single frequency quantum oscillation [157]. To ensure that this quantum oscillation corresponds to the bulk Fermi pocket, we have also performed the magnetization measurements along crystallographic a- and b-axis. For both directions, dHvA oscillations have been observed. The corresponding FFT spectra [Figures 5.8(b) and (c)] show almost similar oscillation frequency [75(3) T for $\mathbf{B}\|a$-axis and 77(2) T for $\mathbf{B}\|b$-axis] along three mutually perpendicular directions, indicating the three-dimensional

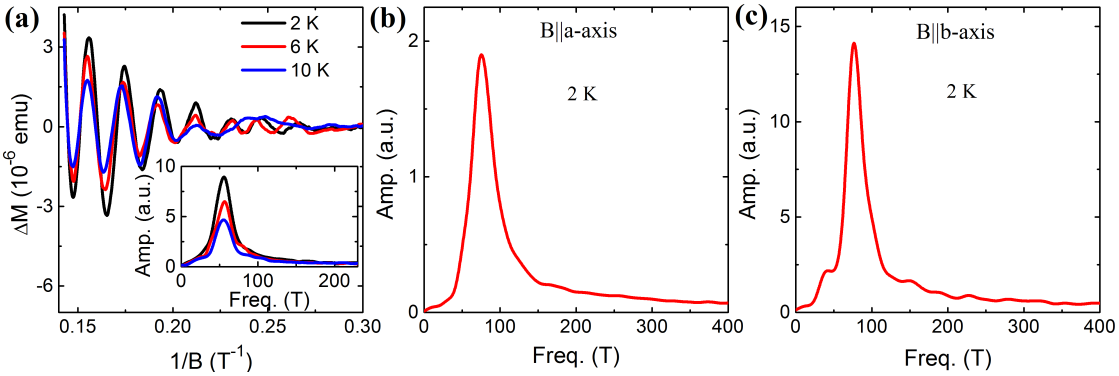

Figure 5.8: (a) dHvA oscillation in the magnetization data with field along c-axis, obtained after background subtraction. Inset shows the corresponding FFT result. FFT spectra of the dHvA oscillation for magnetic field applied along (b) a-axis and (c) b-axis.

nature of the Fermi surface in LaSbTe. Moreover, the estimated carrier density ($\sim 5\times10^{18}$ cm^{-3}) from the oscillation frequency is close to that obtained from Hall measurement and is two orders of magnitude higher than that observed for a typical two-dimensional surface state [158]. Using the Onsager relation, we have calculated the Fermi surface cross-section (A_F) $\sim 5.2(1)\times10^{-3}$ Å^{-2} perpendicular to the c-axis. The corresponding Fermi momentum (k_F) is $\sim 4.0(1)\times10^{-2}$ Å^{-1}. The temperature dependence of the oscillation amplitude is plotted in Figure 5.9(a) and has been fitted using the thermal damping factor of Lifshitz-Kosevich (L-K) formula. The cyclotron effective mass of the carriers is estimated to be $0.06(2)m_0$ from the fitting parameters, where m_0 is the rest mass of a free electron. In Figure 5.9(b), the magnetic field dependence of the oscillation amplitude at 2 K is shown. The experimental data have been fitted using the magnetic field dependent part of the L-K formula. From the fitting parameters, the Dingle temperature, quantum mobility and the mean free path of the charge carriers have been estimated. All the extracted parameters from the quantum oscillation are listed in Table 5.1. As expected, the calculated quantum mobility is seen to be smaller than the classical

Table 5.1: Fermi surface parameters extracted from dHvA oscillation.

F	A_F	k_F	m^*	v_F	T_D	μ_q	l
T	10^{-3} Å^{-2}	10^{-2} Å^{-1}	m_0	10^5 m/s	K	10^3cm^{2}V^{-1}s^{-1}	nm
55(1)	5.2(1)	4.0(1)	0.06(2)	8(3)	19(2)	1.8(3)	50(26)

Drude mobility, which has been obtained from the Hall resistance.

Further information about the topological nature of the band structure in LaSbTe, can be obtained from the Berry phase associated to the motion of the charge carrier. Considering the peak positions of ΔM as integer and valley positions as half integer, the x-axis intercept of a Landau level fan diagram will be 0 for trivial electronic band and 0.5 for non-trivial band structure and vise versa for oscillation in resistivity and magnetic susceptibility [94, 84, 159]. In Figure 5.9(c), we have plotted the Landau level fan diagram from the dHvA oscillation. The obtained intercept ∼-0.15(1) is close to the theoretical value for trivial band structure and far from that expected (0.5) for a non-trivial state. Hence, the observed Berry phase confirms that the bulk band structure of LaSbTe is topologically trivial.

5.3.5 Signature of the helical spin texture in the surface state

A TI is characterized by topologically distinct surface and bulk electronic states. While the bulk state is insulating with a gap between conduction and valence band, surface state hosts linear band crossings. The surface band structure is protected by time reversal symmetry and can be represented by a Dirac-type effective Hamiltonian [160], $H_{surf}(k_x, k_y) = \hbar v_F(\sigma^x k_y - \sigma^y k_x)$, where $\vec{\sigma}$ is the Pauli matrix. This leads to the spin-momentum locking and absence of backscattering of the charge

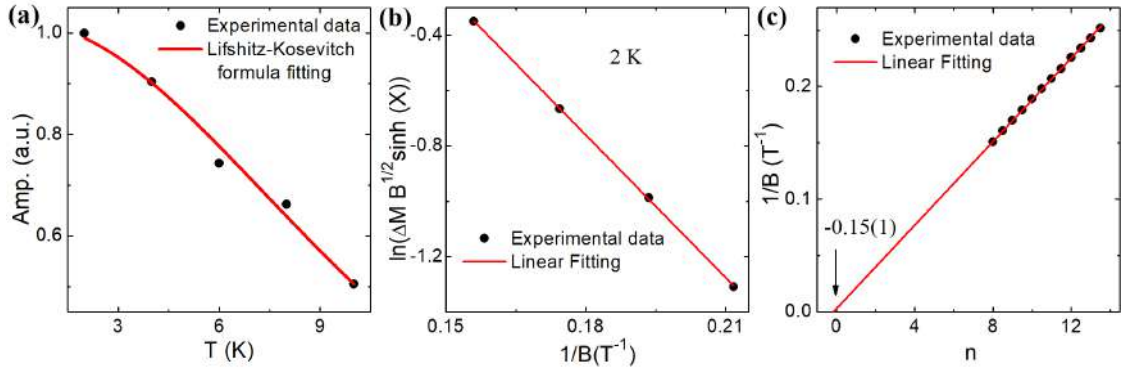

Figure 5.9: (a) Temperature dependence of the oscillation amplitude for magnetic field along c-axis, fitted using the thermal damping term of L-K formula. (b) Field dependence of the oscillation amplitude at 2 K. Solid line is the fit to the experimental data using L-K formula, where $X = 2\pi^2 k_B T m^*/e\hbar B$. (c) Landau level fan diagram with maximum position as n and minimum position as n+1/2. The arrow indicates the x-axis intercept.

carriers during conduction through surface channel [160, 161]. For a fixed momentum ($\boldsymbol{k}$), the electron 'spin' (i.e. total angular momentum) has a fixed direction, which forms a spin-texture [162, 163]. The electron-spin texture can be described in terms of a helicity operator $\hat{h} = (1/k)\hat{z}.(\vec{k} \times \vec{\sigma})$, which takes values +1 and -1 for the lower and upper Dirac cones of the surface electronic band structure, respectively [160]. As a consequence of opposite spin helicity for the upper and lower Dirac cones, the electronic states close to the Dirac point face singularity in their spin orientation, provided the Dirac spectrum is not gapped. This small number of electrons does not have any preferable spin alignment and the spins are randomly oriented. An external magnetic field can align the spins along its direction and as a result a paramagnetic contribution is observed in the total magnetic moment [164]. The corresponding magnetic susceptibility shows a cusp in the $\chi(B)$ plot. The spin-texture of the surface state in 3D TI is shown schematically in Figure 5.10(a). In Figure 5.10(b), the low-field region of the magnetization curve is shown for LaSbTe, at a representative temperature 2 K. Although, diamagnetic behavior

is observed at higher field, a clear paramagnetic signal appears in the low-filed region. The susceptibility (shown in the inset) exhibits a cusp at $B = 0$, as expected for a TI [164]. Similar field dependence of magnetic susceptibility has been reported for several TIs such as Bi_2Se_3, Bi_2Te_3, Sb_2Te_3, and $Bi_{1.5}Sb_{0.5}Te_{1.7}Se_{1.3}$ [164, 165, 166] and narrow gap topological semimetal $ZrTe_5$ [167], both with spin helical Dirac cone surface states. With temperature and chemical potential are set to zero, the total susceptibility can be mathematically formulated as [164],

$$\chi(B) \cong \chi_0 + \frac{\mu_0}{4\pi^2}\frac{x}{L}\left[\frac{(g\mu_B)^2}{\hbar v_F}\Lambda - \frac{2(g\mu_B)^3}{\hbar^2 v_F^2} \mid B \mid\right]. \tag{5.5}$$

Here χ_0, Λ, μ_B, g and L are the background contribution, effective size of the momentum space contributing to the singular part of the total free energy, Bohr magneton, Landé g-factor and thickness of the measured crystal, respectively. x is the fraction of the surface state contributing to the areal susceptibility. A linear field decay of $\chi(B)$ is expected from Equation 5.5, which is indeed observed for LaSbTe single crystals. Another interesting feature of such magnetic response is the 'robustness' of the paramagnetic signal. As shown in Figure 5.10(c), the susceptibility cusp exists even at room temperature and the peak height along with its sharpness are independent of the temperature. This unusual thermal stability of the paramagnetic signal can be attributed to an intrinsic surface cooling process of thermoelectric origin [164]. Such unique temperature independent behavior of susceptibility can not be explained assuming a small paramagnetic or ferromagnetic impurity in diamagnetic host and is completely different from the properties of dilute magnetic semiconductors. Moreover, the standard diamagnetic (Bi), paramagnetic (Pd) samples (Appendix A: Figure 10.1) and topological Dirac semimetal Cd_3As_2 [167], do not show such phenomena. To confirm the origin of the paramag-

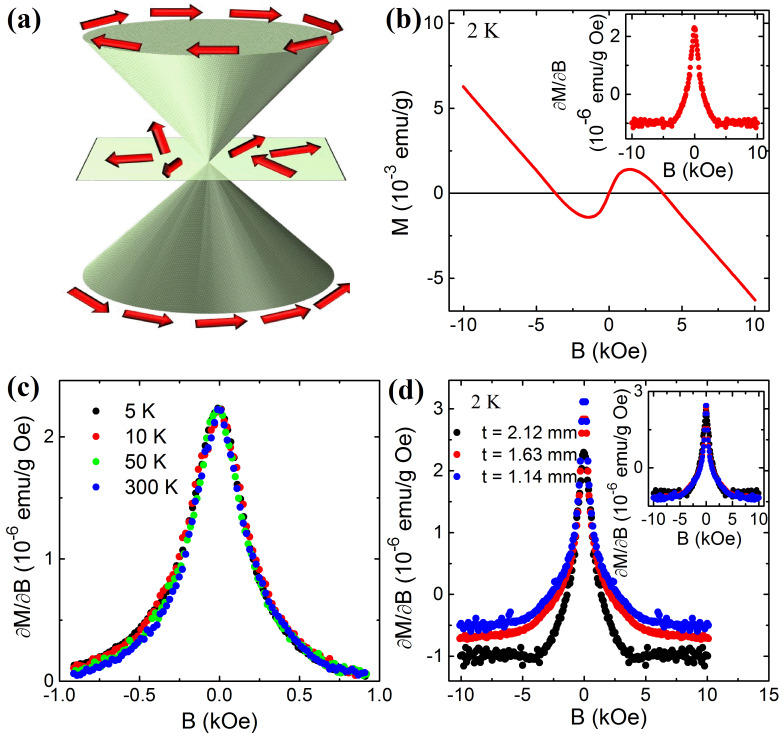

Figure 5.10: (a) Schematic representing the spin-texture of the surface state in a 3D topological insulator. The arrows indicate the direction of the electron spins. (b) Low field region of the magnetization data at 2 K for LaSbTe. Insets shows the corresponding magnetic susceptibility χ ($=\partial M/\partial B$). (c) Magnetic susceptibility at different temperatures, indicating the robustness of the signal. (d) Magnetic susceptibility curves at 2 K for different sample thickness (t). Inset shows the normalized curves.

netic singularity, we have done the magnetization measurements by changing the sample thickness (t). The corresponding susceptibility curves are shown in Figure 5.10(d). With decreasing bulk volume, the diamagnetic background has been seen to decrease and approximately scales with the thickness of the crystal. However, as shown in the inset, the height of the paramagnetic response remains unaltered, similar to that observed in Bi_2Se_3, Bi_2Te_3, Sb_2Te_3 [164]. Therefore, the observed paramagnetic singularity must originate from the non-trivial surface bands near the band crossing points and confirms the TI state in LaSbTe.

5.4 Discussions and conclusions

LaSbTe represents a large family of isostructural compounds. The members of this family have similar electronic band structure and proposed to be weak TIs from theoretical calculations [59]. The single layer of these compounds is an ideal candidate to realize a 2D TI with global band gap, which is induced by spin-orbit coupling. They lead to the weak TI, when the layers are stacked on top of another, thus forming a three-dimensional structure. From ARPES experiments, ZrSnTe (a member of *WHM* family) has been confirmed to host TI state on the surface [91]. On the other hand, several members of this family are shown to be topological nodal-line semimetals [60, 92, 94]. So, it is equally intriguing to explore the topological nature of other members of the family. The magnetotransport results of LaSbTe are identical to several TSMs. However, investigations on the surface state reveal a TI band structure. These results are somewhat similar to that obtained for $ZrTe_5$ [167]. While this compound shows semimetallic transport properties [168], from surface probing ARPES experiments [169] and magnetic measurements [167], it is identified as a TI with a narrow gap in the bulk band structure. In $ZrTe_5$, the semimetallic properties appear due to large bulk carrier density, which suppresses the surface state contribution.

In conclusion, we present the systematic study of magnetotransport and magnetic properties of single crystalline LaSbTe. Magnetic field-induced resistivity turn-on along with low-temperature resistivity plateau have been observed and analyzed from the aspects of possible metal-semiconductor crossover as well as the Kohler's scaling. From the $\rho_{xx}(T)$ curves, a triangular temperature-field phase diagram has been constructed, which is universal for semimetals showing XMR. At 2

K and 9 T, a large transverse MR $\sim 5\times10^3$ % has been observed without any signature of saturation. By rotating the magnetic field along different crystallographic directions, significant anisotropy in the magnetotransport properties has been observed. From the Hall measurement, the presence of two types of carriers has been confirmed. The semiclassical two-band fitting of the Hall and longitudinal conductivity reveals near-perfect carrier compensation with very high carrier mobilities and explains the large MR in the electron-hole resonance regime. The Fermi surface parameters have been calculated from de Haas-van Alphen oscillation in the magnetization measurement. In the low-field region of the magnetization data, a robust paramagnetic singularity has been detected, which is a clear signature of the helical spin-texture of the non-trivial surface state in a topological insulator. Thus our measurements unambiguously confirm a TI state in LaSbTe, which is in accordance with the theoretical calculations.

6

Fermi surface topology and signature of surface Dirac nodes in LaBi

6.1 Introduction

From electronic band structure calculations [170], the members of the family of rare earth monopnictides LaX (X=N, P, As, Sb, Bi) have been proposed to be potential candidates for either TSM or TI. Several magnetotransport studies have reported XMR in both LaSb and LaBi [65, 66, 75, 171]. However, little information is known on the topological nature of their band structure. For both the materials, in fact, the XMR has been attributed to the compensated electron-hole density instead of any non-trivial band topology [66, 172]. On the other hand, it is always challenging to experimentally probe the topological nature of the surface state, which can resolve the debate once and for all. LaBi has the strongest SOC among the members of the LaX family and shares many similarities with LaSb. With the increase in atomic number from N to Bi, the enhanced SOC strength is

predicted to open a energy gap in the bulk at the band crossing points and hence can induce a topological transition from semimetal to insulating phase [170]. While contradicting ARPES reports claim both trivial and non-trivial topological states in LaSb [173, 174], ARPES studies have shown multiple Dirac nodes at the surface of LaBi [174, 175, 176, 177]. Therefore, detailed investigations are required, which would not only settle the topological nature of LaBi but can also shed some light on the electronic band structure of other members of this family.

In this chapter, we have used the magnetotransport and magnetization measurements to probe the nature of both the bulk and surface electronic band structure of LaBi. In several earlier studies on LaBi, the Fermi surface properties have been investigated from the SdH oscillation observed in the MR. In spite of high sample quality, the number of Fermi pockets reported by different groups do not converge [66, 75, 171]. This discrepancy in the reported results can be the inherent problem of this technique. As the SdH oscillation is sensitive to quantum interference effects or noise from the electrical contacts, it may not be possible to identify some oscillation components, especially when the oscillation amplitude is small. Therefore, to complement the results of SdH oscillation we have also analyzed the dHvA oscillation in the magnetization data. This technique is not only free from interference effects, but the much sharper and readily distinguishable oscillation peaks down to very low magnetic field indicate that dHvA is a much better probe to study the Fermi surface than the SdH technique, which often requires high magnetic fields. The obtained Berry phase from both the oscillation techniques confirms the presence of 3D Dirac fermions in LaBi. Furthermore, we have observed a robust paramagnetic singularity in magnetic susceptibility at low field region, which originates from the electronic states near 2D surface Dirac nodes of

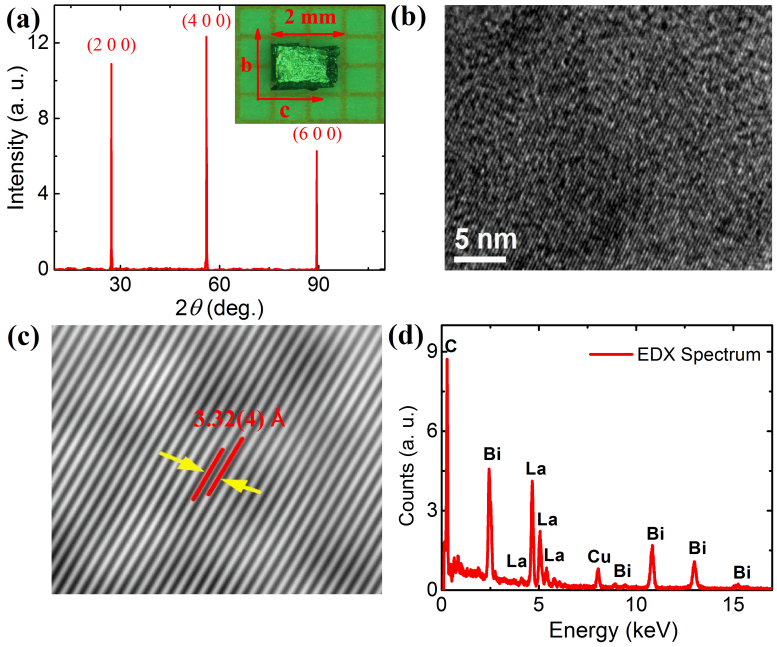

Figure 6.1: (a) XRD pattern of the as grown single crystal. Inset shows a typical LaBi crystal along with different crystallographic axes. (b) HRTEM image of the as-grown crystal. (c) Fourier filtered HRTEM image of the sample, showing the interlayer spacing along crystallographic (2 0 0) plane. (d) The EDX spectroscopy data of a typical crystal.

a TI. Thus our results confirm the topological insulating phase in LaBi along with linear dispersion in the gapped bulk states.

6.2 Sample preparation, characterization, and experimental details

The high quality single crystals of LaBi were grown using indium as flux [45]. We took elemental La (Alfa Aesar 99.9%), Bi (Alfa Aesar 99.999%) and In (Alfa Aesar 99.999%) in an alumina crucible in the molar ratio 1:1:20. The crucible was then sealed in an evacuated quartz tube. The quartz tube was heated to 1000°C, kept at this temperature for 5 h and then cooled slowly (4°C/h) to 700°C. At

this temperature, indium is decanted using a centrifuge. Several single crystals of typical dimension 2×1.8×1 mm were obtained. The single crystals were characterized using XRD technique and HRTEM. Magnetotransport measurements were done via four-probe technique utilizing the ac transport option in a 9 T PPMS. Magnetic measurements were performed using 7 T SQUID-VSM MPMS3. Prior to the magnetic measurements on LaBi, we measured the empty sample holders to make sure that there is no contamination. The obtained values are more than two orders of magnitude smaller than what we recorded with LaBi samples. The measurements were done on several single crystals obtained from the same batch, all of which produced similar results.

Figure 6.1(a) shows the XRD pattern for a typical LaBi crystal along the (1 0 0) plane. The presence of very sharp (h 0 0) diffraction peaks confirms the high crystalline nature of the samples. LaBi crystallizes in a rock salt type structure, belonging to the space group $Fm\bar{3}m$. From the XRD spectrum, the lattice parameter is extracted to be a=6.5703(2) Å, which is consistent with the earlier reports [75, 171]. In the inset, we have shown a typical single crystal of LaBi with different crystallographic axes, along which measurements have been done. The crystallographic a-axis is along [h 0 0] direction. The XRD measurements have been carried out on several single crystals from the same batch. Even though the peak intensity varies, no impurity phase has been detected within the experimental resolution. In Figure 6.1(b), the HRTEM image clearly illustrates the high quality crystalline nature of the LaBi samples. From the Fourier filtered HRTEM image [Figure 6.1(c)], an interlayer spacing d=3.32(4) Å is determined along (2 0 0) plane, which agrees with that calculated from our XRD data (d=a/2). EDX spectroscopy measurements, shown in Figure 6.1(d), confirm almost perfect stoi-

chiometry [La:Bi = 1:1.08] and the absence of any impurity in the LaBi crystals. The maximum relative error in the calculated atomic ratio is ∼5%. The copper and carbon signals in the spectrum correspond to the carbon coated copper grid on which the samples were mounted for HRTEM.

6.3 Results and discussions

6.3.1 Temperature dependence of resistivity and extreme magnetoresistance

As shown in Figure 6.2(a), the zero-field resistivity (ρ_{xx}) of LaBi is metallic in nature and monotonically decreases with decreasing temperature. ρ_{xx} becomes as small as ∼130 $n\Omega$ cm at 2 K and yields a large RRR ∼350. In the low temperature region, the resistivity obeys a power-law behavior, $\rho_{xx}(T)=\rho_0 + AT^n$ with $n\sim3$. When a magnetic field is applied along a-axis while current is parallel to c-axis, ρ_{xx} increases and a metal-semiconductor like crossover starts to appear along with resistivity plateau. As discussed in the previous chapter, such kind of resistivity behavior can be explained from Kohler scaling analysis [73, 178]. From the $\partial\rho_{xx}/\partial T$ curves [Figure 6.2(a) inset], we have identified two characteristic temperatures. T_m increases monotonically with magnetic field and follows a $T_m \propto (B - B_0)^{1/\nu}$ type relation with ν ∼2 above a critical field strength B_0∼1 T, which is similar to LaSbTe and other compensated semimetals [73, 179]. On the other hand, T_i is almost independent of the magnetic field strength.

With the current and magnetic field directions unchanged, an extremely large and non-saturating MR ∼4.4×10^4 % is obtained at 2 K and 9 T [Figure 6.2(b)], which is in agreement with the earlier reports on LaBi [66, 171] and comparable to

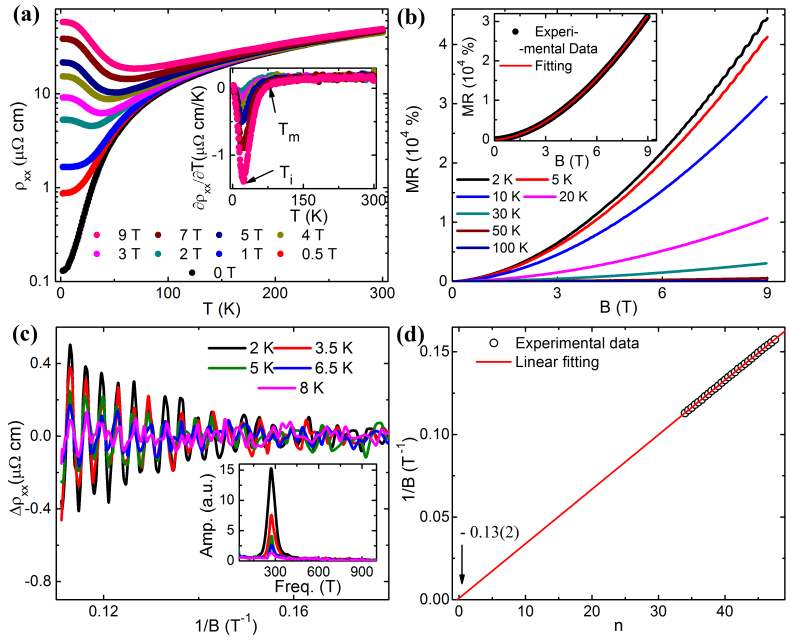

Figure 6.2: (a) Temperature dependence of resistivity for LaBi at different transverse magnetic field. Current and applied magnetic field are along crystallographic c and a-axis, respectively. Inset shows the temperature dependence of the first-order derivative of resistivity at different magnetic fields with characteristic temperatures T_m and T_i. (b) TMR with current parallel to c- and magnetic field along a-axis, at different representative temperatures. Inset shows the power-law behavior of the MR at 10 K. (c) SdH oscillation obtained after subtracting polynomial background from the MR data, plotted with inverse magnetic field ($1/B$) at different temperatures. Inset illustrates the corresponding FFT result. (d) Landau level index plot obtained from SdH oscillation. The arrow shows the the x-axis intercept value.

that observed for several TSMs [73, 153]. However, with increasing temperature the MR decreases rapidly and becomes only ∼6 % at 300 K and 9 T. The fitting in the inset of Figure 6.2(b) reveals that the MR curve obeys a power law, MR$\propto B^m$ with m ∼1.7. This power-law behavior is close to the parabolic magnetic field dependence (MR$\propto B^2$) expected for compensated semimetals from classical two-band theory [64].

6.3.2 Shubnikov-de Haas oscillation and Hall measurement

In Figure 6.2(c), we have plotted the oscillatory part of the resistivity [$\Delta\rho_{xx}(B)$] after subtracting a fifth order polynomial background from the experimental data. The FFT analysis of $\Delta\rho_{xx}(B)$ in the inset of Figure 6.2(c), shows an oscillation frequency 273(5) T, which is in agreement with the earlier report by Tafti *et al.* [75]. However, both Sun *et al.* [66] and Kumar *et al.* [171] have observed an additional higher frequency component in LaBi. From our SdH oscillation data, we can not identify any additional frequency branch, which may be due to very weak amplitude of oscillation for the higher frequency component within the measured magnetic field and temperature range. Whereas, we have clearly observed two Fermi pockets in the same crystal from our dHvA oscillation data to be discussed later. Using the Onsager relation, we have calculated the Fermi surface cross-section $\sim$2.6(1)$\times10^{-2}$ Å^{-2} perpendicular to the crystallographic a-axis. The corresponding Fermi momentum and Fermi velocity are found to be 9.1(2)$\times10^{-2}$ Å^{-1} and 5.6(1)$\times10^{5}$ m/s, respectively. The temperature dependence of oscillation amplitude can be fitted using the thermal damping factor of L-K formula. From the fitting parameters, we have calculated the cyclotron effective mass $\sim 0.19(1)m_0$ for the charge carriers. From the magnetic field-induced damping of the oscillation amplitude, the Dingle temperature is found to be 11.3(2) K. Using this Dingle temperature, we have also calculated the quantum mobility $\sim 10^3$ cm^2 V^{-1} s^{-1}, which can provide an estimate on the mobility of the charge carriers.

The Berry phase associated to the charge carriers can provide more information about the nature of band structure in LaBi. In Figure 6.2(d), we have plotted the Landau level fan diagram from the SdH oscillation data, assigning maximum positions as integers and minimum positions as half-integers. The ob-

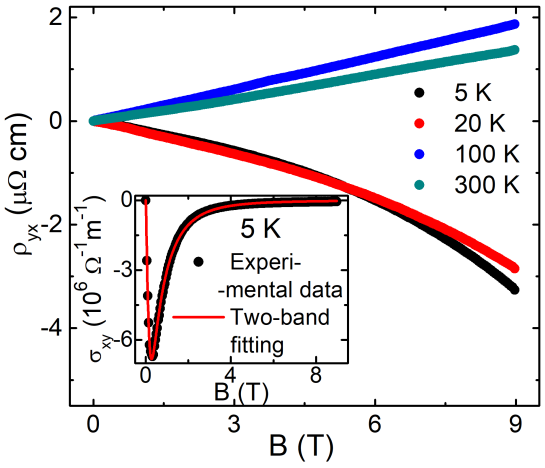

Figure 6.3: Magnetic field dependence of Hall resistivity in LaBi at different representative temperatures. Inset shows the classical two-band fitting of Hall conductivity.

tained intercept [∼-0.13(2)] is close to the theoretical value expected for 3D Dirac fermions (intercept∼±0.125) but far from that for a parabolic band dispersion (intercept∼0.5) [86], which confirms the presence of 3D Dirac fermions in LaBi.

In Figure 6.3, we have shown the Hall resistivity data for LaBi. While the Hall resistivity is positive and almost linear in the high temperature region, it becomes slightly non-linear and changes sign at low temperature. So, both electron and hole-type carriers are present in LaBi. In the inset of Figure 6.3, the Hall conductivity is fitted using classical two-band model [89]. The obtained electron and hole densities ∼2.47×10^{19} cm^{-3} and ∼2.45×10^{19} cm^{-3}, respectively, confirm that LaBi is a compensated semimetal. From the fitting parameters, the mobilities of the carriers are found to be ∼3.55×10^4 cm^2 V^{-1} s^{-1} and ∼0.45×10^4 cm^2 V^{-1} s^{-1} for electrons and holes, respectively. The obtained carrier mobility is quite large and comparable to that reported in several topological Dirac and Weyl semimetals [85, 92, 155].

6.3.3 de Haas-van Alphen oscillation and Fermi surface properties

In Figure 6.4(a), we have shown the results of magnetization measurements for magnetic field applied along crystallographic a-axis. Similar to other TSMs, a diamagnetic behavior has been observed together with very prominent dHvA oscillations. Contrary to the SdH oscillation, which can be identified only up to 8 K, we can easily resolve the dHvA oscillation even at 15 K. At the lowest measured temperature (2 K), weak but detectable oscillations have been observed down to 0.8 T, which leads to a magnetic length $l_B = \sqrt{\hbar/eB} \approx 29$ nm. This large magnetic length implies high quality of the LaBi crystals. We have extracted the oscillatory component (ΔM) by subtracting a smooth background and plotted in Figure 6.4(b). The corresponding FFT spectrum in the inset, reveals two oscillation frequencies 266(1) T and 598(2) T. The existence of more than one frequency branch is also evident from the small but sharp oscillation peak next to each higher amplitude peak in Figure 6.4(b) [also see Figure 6.4(d)]. The sharp peaks in the FFT spectrum imply almost no error in the frequency values deduced from this technique. On the other hand, in SdH oscillation, due to the relatively broad nature of the peak in FFT spectrum, the error in the obtained frequency value is higher compared to dHvA. This is indeed expected as we have used larger number of oscillation cycles for dHvA oscillation analysis compared to few peaks of oscillation obtained in SdH measurement. Moreover, quantum oscillations are expected to be observed in very clean samples, i.e., where the conductivity and hence mean free path of the carriers is very high. Therefore, in order to obtain appropriate electrical signals in SdH oscillation measurements, quite high current is required.

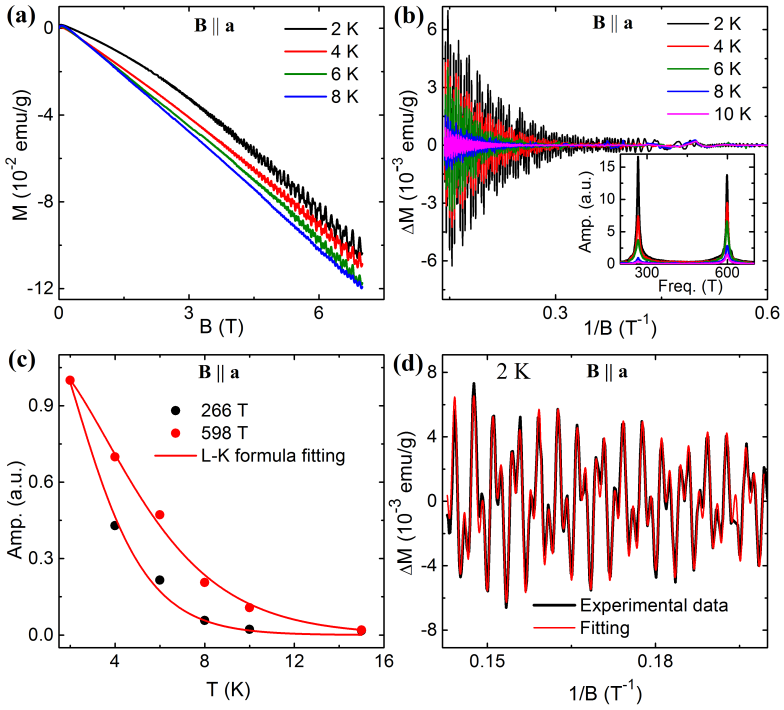

Figure 6.4: (a) Magnetic field dependence of magnetic moment of LaBi with field applied along crystallographic a-axis. (b) dHvA oscillation extracted by background subtraction at different temperatures. Inset shows the corresponding FFT spectra. (c) Temperature damping of dHvA oscillation amplitude, fitted using the L-K formula for $\mathbf{B}\|a$-axis. (d) Two-band L-K formula fitting of dHvA oscillation data.

This can cause local heating and, as a result, blur the finer details of the oscillation. However, dHvA technique is free from such drawback. From the Onsager relationship, the Fermi surface cross-sections have been found to be $2.53(1)\times10^{-2}$ Å^{-2} and $5.70(2)\times10^{-2}$ Å^{-2}, for smaller and larger pockets, respectively. The temperature dependence of the FFT amplitude is shown in Figure 6.4(c) and has been fitted using L-K formula. From the fitting parameters, we have calculated the effective masses $0.11(3)m_0$ and $0.07(2)m_0$ for 266(1) T and 598(2) T, respectively. Very clear dHvA oscillations have also been observed, when we apply the magnetic field along other two crystallographic axes. Although the oscillation frequencies

Table 6.1: Fermi surface parameters extracted from SdH and dHvA oscillations.

	Configuration	F T	A_F 10^{-2-2}	k_F 10^{-2-1}	m^* m_0	v_F 10^5 m/s
SdH	$\mathbf{B}\|a$	273(5)	2.6(1)	9.1(2)	0.19(1)	5.6(1)
dHvA	$\mathbf{B}\|a$	266(1)	2.53(1)	8.97(2)	0.11(3)	9.3(5)
		598(2)	5.70(2)	13.47(2)	0.07(2)	22(3)

are same for crystallographic a- and c-axis, both peaks in FFT spectrum shift slightly towards higher values [272(1) T and 602(2) T] for field parallel to b-axis. As LaBi has cubic symmetry, which we have also confirmed from our XRD and HRTEM measurements, it is expected that these three crystallographic axes should be equivalent. On the other hand, in LaBi, the hole pocket has been seen to be highly anisotropic [171]. Therefore, a slight misalignment of the magnetic field and crystallographic b-axis may result in this small deviation. In Table 6.1, we have summarized the Fermi surface parameters obtained from both the oscillation techniques. The small difference in the frequency values, extracted from these two methods, may be partially due to a small misalignment of the magnetic field and or the higher error in determining the SdH frequency as discussed earlier. However, the difference in the number of Fermi pockets, probed in these two techniques, can not be explained from such arguments.

As two frequencies are involved in the dHvA oscillation in LaBi, we can not extract the Berry phase from the simple Landau level index plot. In such case, the experimental data can be analyzed using a superposition of damped sine-function for each frequency component, which is given by the complete L-K formula [84, 94],

$$\Delta M \propto -B^{1/2} R_T R_D R_S sin\left[2\pi\left(\frac{F}{B} + \gamma - \delta\right)\right]. \tag{6.1}$$

Here, R_T and R_D are the thermal and field damping factors, respectively, as discussed before and $R_S = cos(\pi g m^*/m_0)$. Figure 6.4(d) shows the two-band L-K formula fitting with the experimental data. From the fitting parameters, the Berry phase has been calculated to be $2\pi[0.50(3)+\delta]$ and $2\pi[0.46(2)+\delta]$ for 266(1) T and 598(2) T frequency branches, respectively, which are close to the π Berry phase expected for the Dirac fermions. Small deviation in Berry phase value is quite common in this type of materials and can be associated with the Fermi surface anisotropy [63, 94]. The obtained Berry phase for both the Fermi pockets confirms the non-trivial nature of the electronic band structure in LaBi.

6.3.4 Paramagnetic singularity in magnetization measurement

Figure 6.5(a) schematically illustrates the spin-texture of the surface state for a typical 3D topological insulator both without and with magnetic field. In Figure 6.5(b), we have shown the low-field region of the $M(B)$ curves for LaBi, when the applied magnetic field is along crystallographic c-axis. While the magnetization data predominantly demonstrate diamagnetic nature throughout the measured magnetic field range, a clear paramagnetic behavior is observed in the vicinity of zero field. In Figure 6.5(c), the corresponding susceptibility plots are shown at different representative temperatures. We have observed robust cusps at B=0, which persist up to room temperature. As discussed for LaSbTe, similar paramagnetic singularity in the low-field region, which originates from the topologically non-trivial surface states, has been previously reported in several topological materials [164, 166, 167]. $\chi(B)$ should decrease linearly with magnetic field, which is indeed observed in LaBi [Figure 6.5(c) inset]. We performed the measurements on

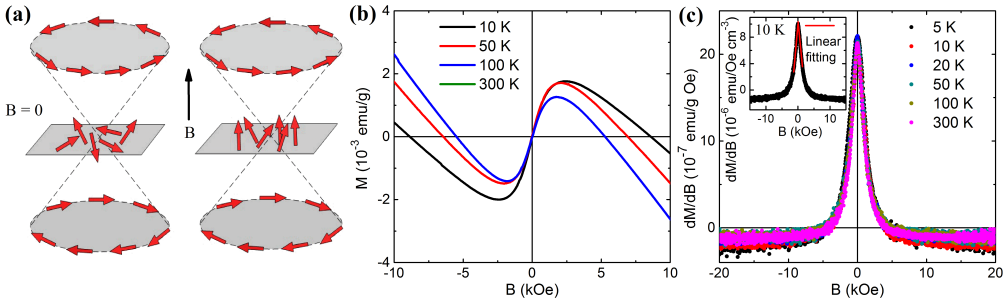

Figure 6.5: (a) Schematic illustrating the helical spin-texture of the Dirac cones in the surface state for a 3D topological insulator both without and with magnetic field. The arrows show the direction of the electron spins. (b) Magnetic field dependence of the magnetic moment for LaBi in low-field region at different representative temperatures. (c) Field dependence of magnetic susceptibility χ, calculated by taking first order derivative of magnetic moment. Inset shows the linear field decay of χ.

several crystals from the same batch. Though the cusp width varies slightly with the dimensions, as expected from Equation 5.5, the general behavior remains unaltered. So, this low-field magnetic response is an intrinsic property of the measured crystals. Therefore, LaBi certainly hosts topological Dirac fermions in the surface state, which is in accordance with the ARPES reports [174, 175, 176, 177].

6.4 Discussion and conclusions

LaBi has emerged as another new material with XMR and large carrier mobility. Although few studies have been focused on the magnetotransport properties, the topology of its electronic band structure remains substantially unexplored. Furthermore, the XMR is believed to appear due to the compensated semimetallic nature of LaBi in the electron-hole resonance regime. On the other hand, from the recent ARPES measurements, multiple Dirac cones have been observed at the surface of LaBi, which support the picture of a topological insulator, as also pre-

dicted by theoretical calculation. We have combined the magnetotransport and magnetization measurements to probe the bulk Fermi surface along with the surface electronic states of LaBi. Similar to earlier reports, a non-saturating XMR ($\sim$4.4$\times$10^4 %) and magnetic field-induced resistivity turn-on behavior have been observed. The measured non-linear Hall resistivity shows the presence of two types of charge carriers with high carrier mobility and almost perfectly compensated carrier densities. The Fermi surface parameters have been analyzed from both SdH and dHvA oscillations. In the low-field region of the magnetization data, a robust paramagnetic singularity has been identified, which persists up to room temperature. This phenomenon is the signature of the helical spin texture of a 3D TI surface state. On the other hand, the Berry phase extracted from both SdH and dHvA oscillations confirms the presence of 3D Dirac fermions in LaBi. These results can only be explained assuming a small energy gap in the electronic band structure of the bulk state due to the strong SOC and linearly dispersing bulk bands. Therefore, LaBi must be a three-dimensional topological insulator, which also hosts gapped Dirac cone in its bulk band structure. Thus from our experimental results, we can comprehensively conclude the debate over the topological nature of LaBi and confirm the results of ARPES and band structure calculations.

7

Probing the Fermi surface and magnetotransport properties of $MoAs_2$

7.1 Introduction

The group of transition metal dipnictides (TMDs) [XPn_2 (X = Ta, Nb; Pn = P, As, Sb)], has been theoretically predicted as potential candidates for investigating the topology protected electronic systems [180]. These materials possess identical band structure and host multiple band anticrossings in the vicinity of the Fermi level. In absence of SOC, these anticrossings form a nodal-line in the $\boldsymbol{k}$-space. However, with the introduction of SOC, the nodal line is gapped out, resulting in only isolated electron and hole pockets. Several magnetotransport studies have been reported for different members of this family [71, 181, 182, 183]. Though the results vary slightly for different systems, they all exhibit low-temperature resistivity saturation, large MR and high carrier mobility, which are some of the characteristic features of TSMs. On the other hand, in these reports [71, 181, 182,

183], the magnetotransport properties are often attributed to the compensated electron and hole density rather than any non-trivial band topology.

In this chapter, we have investigated the electronic transport properties of $MoAs_2$, a member of the XPn_2 family. We have observed large and anisotropic MR and low-temperature resistivity plateau, in spite of quite high carrier density and single-band dominated transport. The Fermi surface properties have been analyzed from dHvA oscillation. The band structure calculations reveal a large electron-type Fermi pocket along with an 'open-orbit' hole-type Fermi surface.

7.2 Sample preparation, experimental, and computational details

The single crystals of $MoAs_2$ were grown via the iodine vapor transport method [184]. First, the polycrystalline powder was synthesized from the elemental Mo (Alfa Aesar 99.95%) and As (Alfa Aesar 99.9999%) in an evacuated quartz tube at 950°C for 5 days. The powder and iodine (5 mg/cc.) were then sealed in another quartz tube under vacuum and put in a gradient furnace for 7 days. The hotter end of the tube, containing the polycrystalline powder, was kept at 950°C, while the other end was maintained at 900°C. Needle like single crystals with typical dimensions $1\times0.8\times0.4$ mm^3 were obtained at the cold end. The as grown crystals were characterized by powder XRD technique. The transport measurements were done in a 9 T PPMS using ac-transport option and rotating sample holder. The electrical contacts were made using gold wires and conducting silver paint in a four-probe configuration. Magnetization measurements were performed in 7 T SQUID-VSM MPMS3.

Band structure calculations have been done using density functional theory within the Local Density Approximation (LDA) exchange correlation as implemented in VASP [103]. PAW pseudo-potentials are used to describe the core electron in the calculation [105]. LDA+U method is used to deal with the strong correlation in this compound with the standard value of U=2.4 eV for the correlated Mo-4d orbitals. The electronic wavefunction is expanded using plane wave up to a cutoff energy of 224.584 eV. Brillouin zone sampling is performed by using a (8×8×8) Monkhorst-Pack $\boldsymbol{k}$-grid. Both atomic position and cell parameters are allowed to relax, until the forces on each atom are less than 0.01 eV/Å.

7.3 Results and discussion

7.3.1 Sample characterization

$MoAs_2$ crystallizes in $OsGe_2$-type structure with monoclinic space group *C12/m1* [185]. The primitive unit cell contains two inequivalent Mo atoms. The crystal structure is shown in Figure 7.1(a). Each molybdenum atom is surrounded by six arsenic atoms, forming a trigonal prism. A typical single crystal of $MoAs_2$ is shown in the inset of Figure 7.1(b) with appropriate length scale. The needle-like single crystals of XPn_2 family, preferably grow along the b-axis [181]. Here, the top facet of the crystal corresponds to (0 0 1) plane, whereas inclined side facet is the (2 0 1) plane. The long edge, shared between these two planes, gives the direction of the crystallographic b-axis [181]. For simplicity, we have discussed the experimental results along three mutually perpendicular crystallographic directions, b, c [perpendicular to (0 0 1) plane] and b×c-axes, throughout this chapter. The XRD spectrum of the powdered crystals is shown in Figure 7.1(b). The obtained

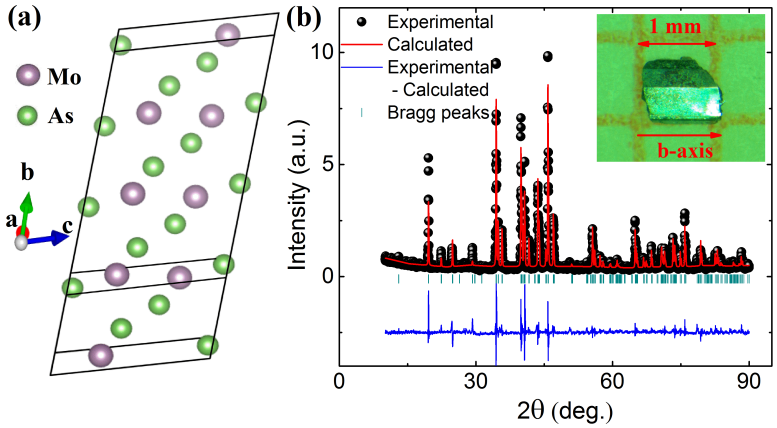

Figure 7.1: (a) Crystal structure of $MoAs_2$. (b) XRD spectra of the powdered $MoAs_2$ crystals. Inset shows a typical single crystal grown along the crystallographic *b*-axis.

spectrum confirms the phase purity of the as grown crystals and absence of any impurity. We have analyzed the XRD pattern by Rietveld structural refinement using FULLPROF software package. The refined parameters, a=9.062(5), b=3.296(2), and c=7.715(4) Å and β=119.3(2)°, are consistent with an earlier report [185].

7.3.2 Temperature dependence of resistivity

The resistivity measurements on as grown single crystals have been done with current along *b*-axis. As illustrated in Figure 7.2(a), the temperature dependence of zero-field resistivity [ρ_{xx}(T)] exhibits metallic character throughout the measured temperature range. ρ_{xx} becomes as small as ∼0.35 $\mu\Omega$ cm at 2 K and leads to a RRR ∼312. Very low residual resistivity as well as high RRR are the clear signatures of the high quality of the single crystals. While the resistivity decreases linearly with temperature from 300 K, the experimental data can be fitted well with $\rho_{xx}(T) = a + bT^n$ (n ∼3) type relation below 75 K [Figure 7.2(a) inset]. When a transverse magnetic field is applied, the low-temperature resistivity shows

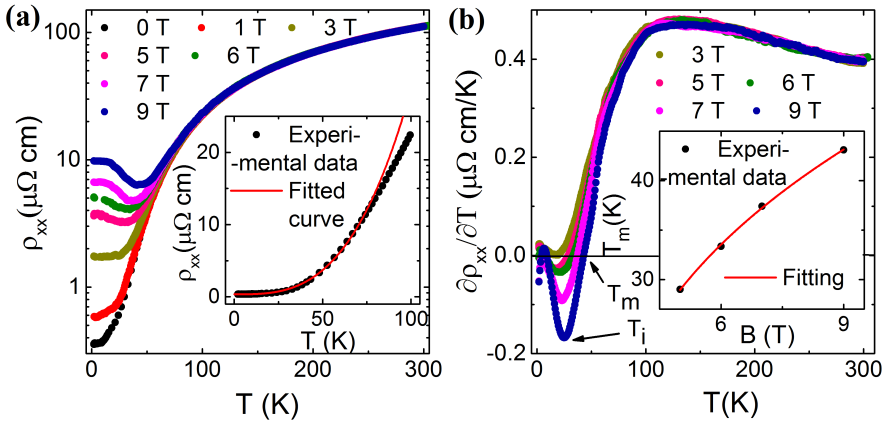

Figure 7.2: (a) Temperature dependence of resistivity at different transverse magnetic fields, applied along c-axis. Inset shows the zero-field resistivity in the low temperature region, fitted using $\rho_{xx}(T) = a + bT^n$ type relation. (b) $\partial\rho_{xx}/\partial T$ vs. temperature curves at different magnetic field strengths, which reveal two characteristic temperatures T_m and T_i. The magnetic field dependence of metal-semiconductor-like crossover temperature is shown in the inset.

a drastic enhancement followed by a saturation behavior. The field-induced metal-semiconductor-like crossover and resistivity plateau have been found to be generic features of TSMs [69, 70, 92]. From the $\partial\rho_{xx}/\partial T$ curves in Figure 7.2(b), we have identified two characteristic temperatures (T_m and T_i). As shown in the inset of Figure 7.2(b), T_m increases monotonically with applied magnetic field strength and follows a $(B - B_0)^{1/3}$ type relation. On the other hand, T_i shows a weak magnetic field dependence.

7.3.3 Large and anisotropic magnetoresistance

We have measured the transverse MR with current along b-axis and magnetic field parallel to c-axis in the temperature range 300 K down to 2 K. At 9 T and 2 K, a very large and non-saturation MR $\sim 2.75\times10^3\%$ has been observed [Figure 7.3(a)]. The obtained value is smaller than that reported for other members of the XPn_2

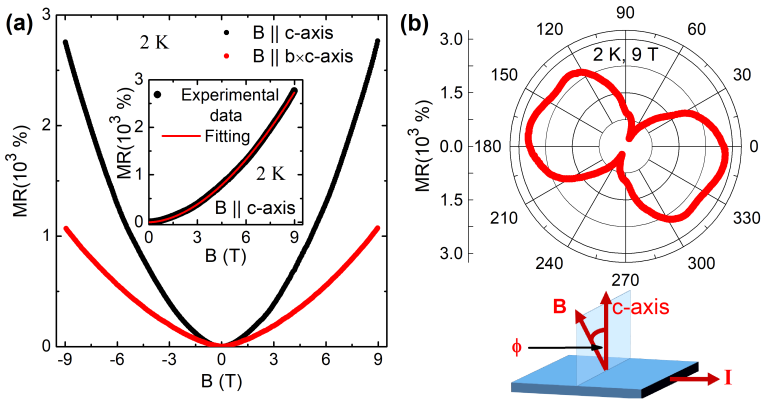

Figure 7.3: (a) TMR of $MoAs_2$ at 2 K with current along b-axis and magnetic filed applied along two mutually perpendicular crystallographic directions, c-axis and $b\times c$-axis. In the inset, the fitting illustrates nearly parabolic magnetic field dependence of MR. (b) Polar plot of MR, when the field is rotated in the plane perpendicular to the crystallographic b-axis. The inset shows the schematic of the experimental set-up.

family [71, 181, 183], but is comparable to several other TSMs [144, 150, 151, 152]. With the increase in temperature, MR decreases drastically and becomes less than 1% at 300 K. As shown in the inset for a representative temperature, the MR data obey almost quadratic magnetic field dependence (MR$\propto B^{1.8}$). Keeping the current direction unaltered, when the magnetic field is applied along $b\times c$-axis, the value of MR changes significantly and becomes $\sim 1.1\times 10^3$% at 2 K and 9 T. To map the complete directional dependence of the magnetotransport properties, the magnetic field is rotated in the plane perpendicular to the current, while keeping the current direction always along b-axis. The calculated MR is shown as a polar plot in Figure 7.3(b). The MR manifests a two-fold rotational symmetry with 'butterfly-like' strong anisotropy. At 2 K and 9 T magnetic field, the maximum MR value is $\sim 2.8\times 10^3$% at $\sim 170°$ (and $\sim 350°$), whereas it becomes as small as 250% at around 65° (and $\sim 245°$). The large anisotropic ratio (~ 11.2) suggests the highly anisotropic nature of the Fermi surface in $MoAs_2$. In addition to this

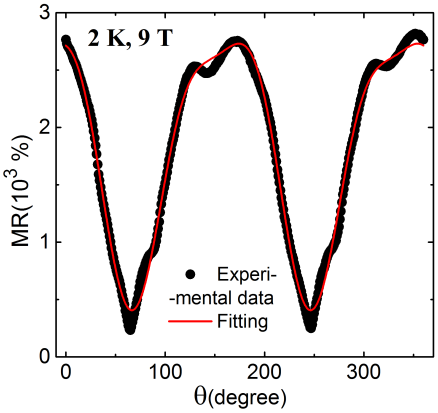

Figure 7.4: Angle dependence of the transverse magnetoresistance, fitted assuming the contributions from both two-fold and four-fold symmetry.

two-fold symmetry pattern, we have observed dips and kinks in the MR value at ∼145° (and ∼325°) and ∼90° (and ∼270°), respectively. They may be due to some higher order texturing, which disappears quickly with increasing temperature. Butterfly-like anisotropic pattern in MR has been previously observed in manganite system, underdoped cuprate superconductor as well as in ZrSiS [93, 186, 187]. However, in these materials, higher order textures are found to be more robust than in $MoAs_2$. The experimental data can be fitted to a great extent (Figure 7.4) assuming contributions from both two-fold and four-fold symmetries [186], $\mathrm{MR}(\phi) = C + A_2 sin[2(\phi - \phi_2)] + A_4 sin[4(\phi - \phi_4)]$, where A_2 (A_4) and ϕ_2 (ϕ_4) are the amplitude and phase of the two-fold (four-fold) symmetry, respectively. C is an arbitrary constant. The overall pattern in Figure 7.3(b) appears to be tilted with respect to the crystallographic axes. This may be the consequence of the complex nature of the Fermi surface and the relative contributions of different Fermi pockets in the electronic transport properties [188].

We have also measured the MR by changing the angle between current and magnetic field, i.e., by rotating the magnetic field along *bc*-plane. Although the

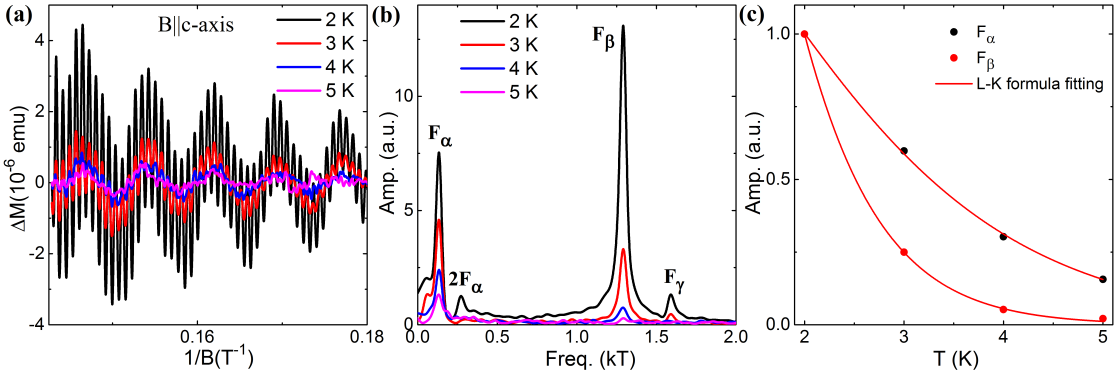

Figure 7.5: (a) dHvA oscillation in the magnetization data of $MoAs_2$ for magnetic field along crystallographic c-axis at different representative temperatures. (b) The FFT spectra of the dHvA oscillation. (c) Oscillation amplitude as a function of temperature for two Fermi pockets, F_α and F_β.

MR value becomes minimum with parallel electric and magnetic field as expected, it still remains positive. In an earlier study [189], negative LMR has been observed for $MoAs_2$ below 40 K. Negative LMR is a signature of the ABJ chiral anomaly [76, 168]. However, negative LMR can also appear due to the current jetting effect, i.e., because of inhomogeneous current distribution inside the sample [190]. In fact, for $TaAs_2$, it has been shown that this effect can be easily suppressed by changing the current and voltage lead positions [182]. Nevertheless, chiral anomaly induced negative LMR has a specific temperature and magnetic field dependence [76], which is distinct from current jetting effect. For $MoAs_2$, we did not find any negative LMR, even when we change the angle between current and magnetic field by a few degrees to compensate for any possible misalignment.

7.3.4 de Haas-van Alphen oscillation and Fermi surface properties

The magnetization measurement of the $MoAs_2$ crystals with magnetic field along c-axis shows a diamagnetic character with prominent dHvA oscillation up to ∼5 K. We have extracted the oscillatory part in the magnetization data by subtracting a smooth background and plotted in Figure 7.5(a) as a function of inverse magnetic field at different temperatures. The corresponding FFT spectrum in Figure 7.5(b), reveals three fundamental frequencies F_α [134(3) T], F_β [1290(2) T] and F_γ [1589(5) T]. Using the Onsager relation, we have calculated the Fermi surface cross-sections for these three Fermi pockets perpendicular to the c-axis [See Table 7.1]. The obtained cross-sections for F_β and F_γ, are the largest among the members of XPn_2 family [71, 153, 181, 182, 183] as well as other TSMs and comparable to those of the three-fold degenerate TSMs WC and MoP [191, 192]. As a consequence, the carrier density is also expected to be quite higher than conventional semimetals, which we will discuss later. The oscillation amplitude decreases rapidly with increasing temperature and the F_γ component vanishes completely above 3 K. Therefore, due to lack of experimental points, we could not analyze the thermal damping of F_γ component. However, the temperature dependence of oscillation amplitude for F_α and F_β pockets, has been shown in Figure 7.5(c) and fitted using the thermal damping factor of the L-K formula. From the fitting parameters, the cyclotron effective mass has been obtained to be $0.37(1)m_0$ and $0.74(2)m_0$ for F_α and F_β Fermi pockets, respectively. We have also calculated the Fermi momentum and Fermi velocity from the quantum oscillations. All the extracted parameters have been summarized in Table 7.1.

Table 7.1: Fermi surface parameters of $MoAs_2$ calculated from dHvA oscillations. A'_F corresponds to the theoretically calculated Fermi surface cross-sections.

Configuration	F T	A_F 10^{-3} Å^{-2}	k_F 10^{-3} Å^{-1}	m^* m_0	v_F 10^5 m/s	A'_F 10^{-3} Å^{-2}
B‖c-axis	134(3)	12.8(3)	63.8(8)	0.37(1)	1.99(8)	10
	1290(2)	123.0(2)	197.8(2)	0.74(2)	3.09(8)	200
	1589(5)	151.5(4)	219.6(3)	-	-	300
B‖b-axis	1330(3)	126.8(3)	200.9(2)	-	-	120
	1524(5)	145.3(5)	215.1(3)	-	-	145
B‖b×c-axis	135(3)	12.9(3)	64.0(7)	-	-	10
	458(4)	43.7(4)	117.9(5)	-	-	109
	1909(3)	182.0(3)	240.7(2)	-	-	209

The dHvA oscillation has also been observed, when the magnetic field is applied along other two mutually perpendicular directions, i.e., along crystallographic b-axis and $b\times c$-axis (Figure 7.6). From the comparison of the FFT spectrum along different directions, it is clear that the Fermi surface of $MoAs_2$ is quite complex with at least three Fermi pockets present in the system. The Fermi surface geometry also has a strong anisotropy, which is consistent with the observed anisotropic MR. The extracted frequency components and related parameters are listed in Table 7.1. We could not calculate the effective mass and Fermi velocity of the charge carriers for the Fermi pockets along these two directions due to the lack of experimental data, as the oscillations suppress rapidly with increasing temperature.

7.3.5 Hall measurement

To get an estimate about the carrier density and mobility, the Hall resistivity of the crystal has been measured at different temperatures. In Figure 7.7, ρ_{yx} is shown at some representative temperatures. At 300 K, Hall resistivity is negative and linear

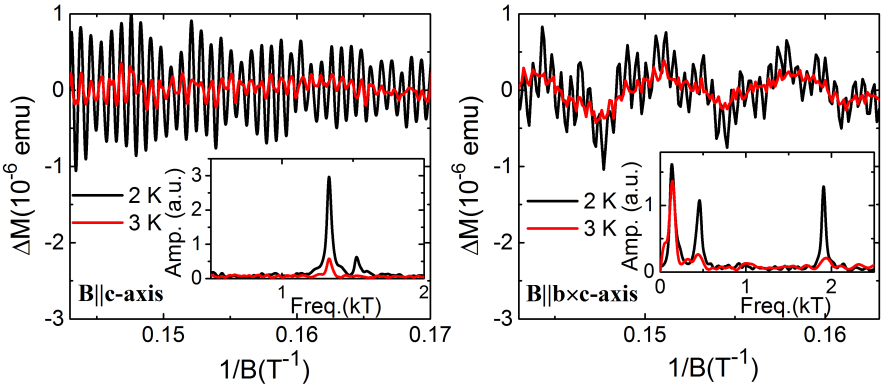

Figure 7.6: dHvA oscillation for magnetic field parallel to b- and $b\times c$-axes. Insets show the corresponding FFT spectrum.

with magnetic field, which indicate electron type charge carriers. As temperature is decreased, ρ_{yx} shows a slightly non-linear behavior at around 50 K, which is a signature of multi-band transport, as also apparent from the quantum oscillation analysis. However, ρ_{yx} remains negative throughout the measured temperature range and can be analyzed using one-band model. From the slope of the curve $R_H = -\frac{1}{ne}$, the electron density (n) is calculated to be $4.8(2)\times10^{21}$ cm^{-3} at 2 K. The carrier density is at least two orders of magnitude higher than that observed for most of the TSMs and is in agreement with the large Fermi pockets, which have been probed from the quantum oscillation measurements. In spite of such high carrier density, the value of carrier mobility is quite high $3.6(1)\times10^3$ cm^{2}V^{-1}s^{-1} and comparable to different topological systems [150, 152, 155].

7.3.6 Band structure calculations

The calculated electronic band structure of $MoAs_2$ is plotted in Figure 7.8 along the high-symmetry directions, without including the effect of SOC. Even with SOC, the band structure remains almost the same. The band structure in the low-energy

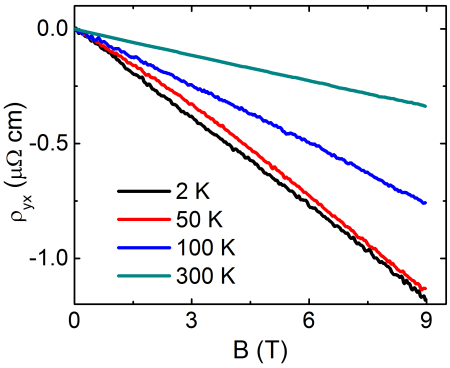

Figure 7.7: Magnetic field dependence of Hall resistivity at different temperatures.

spectrum is dominated by Mo-d electrons. The overall electronic structure gives two large Fermi surface pockets (Figure 7.9), one electron pocket, extending along Y and F-points, and a hole-Fermi-surface along the direction of Γ to X. With small tuning of the chemical potential, one can also find a tiny hole pocket along Γ to Y, and another electron pocket at X-points. However, these two tiny pockets are subjected to the details of the electronic band structure calculation, and more importantly, they are difficult to detect. From the quantum oscillation results, at least two large and one small Fermi pockets have been identified in $MoAs_2$. On the other hand, from the Hall measurement, it is clear that the measured single crystals are electron doped. Hence, it is possible that there are two electron-type pockets, one large and one tiny, whereas the other large Fermi pocket is hole-type. However, the mobility of the holes must be quite small compared to the electrons so that the transport properties are dominated only by electron-type charge carriers.

7.4 Discussions

One of the striking aspects of this compound is that the hole pocket is an 'open-orbit' Fermi surface and is strongly three-dimensional. This leads to an important

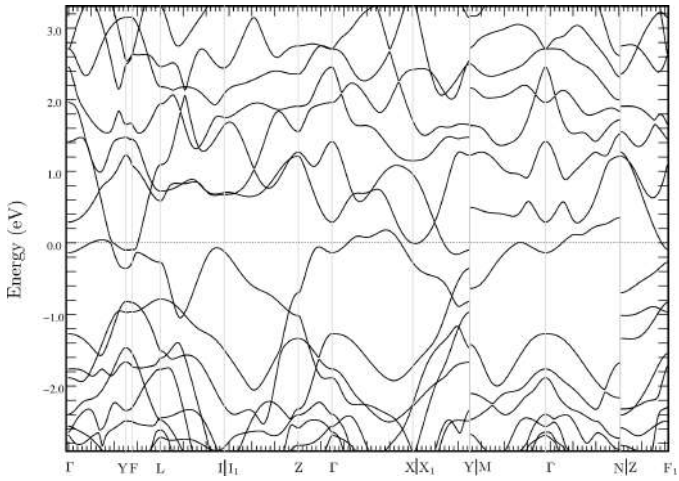

Figure 7.8: The bulk band structure of $MoAs_2$ without spin-orbit coupling. The Fermi energy has been aligned with E=0 eV.

question: can an open orbit Fermi surface show quantum oscillations? We note that open Fermi surface is also present in several organic compounds [193, 194, 195, 196, 197, 198, 199], as well as in the Ortho-II phase of $YBa_2Cu_3O_{7-\delta}$ (δ>0) cuprates [200, 201, 202, 203, 204]. In these materials, we observe quantum oscillation with multiple frequencies. There are also several theories, modeling the origin of quantum oscillation from open-orbit Fermi surface [205, 206, 207, 208, 209, 210]. In Table 7.1, we have shown the theoretically calculated Fermi surface cross-sections (A'_F) with those obtained from our quantum oscillation measurements. Although the obtained values are comparable, there are some differences, which may occur due to different factors such as small deviation from perfect stoichiometry during the crystal growth and various approximations for the theoretical calculations. We have noticed that the theoretically overestimated cross-sections are the ones, which are related to the open-orbit Fermi surface. For open orbit, band renormalization plays crucial role. The effective correlation strength of this band becomes larger, which may lead to the reduction of its Fermi surface area. From our theoretical

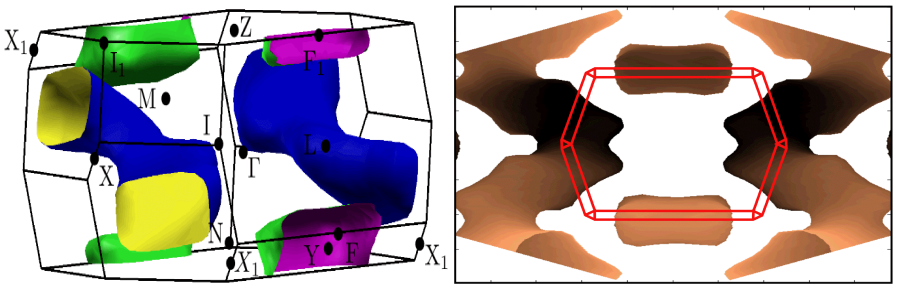

Figure 7.9: The theoretically calculated Fermi surface for $MoAs_2$, showing two large Fermi pockets including hole-type open-orbit Fermi surface.

results, we have also found an additional small Fermi pocket (A'_F=4×10^{-3} Å^{-2}) along crystallographic *b*-axis, which is not detectable in our dHvA oscillation. This could be due to the large effective mass or lower mobility of the charge carriers associated with this pocket and may require higher magnetic field to resolve.

Unlike for $NbAs_2$ and $TaAs_2$ materials, $MoAs_2$'s band structure does not show any Dirac cone, at least not a cone, which is isolated from other quadratic bands. Even for NbP, a widely studied Weyl semimetal, MR measurements revealed the coexistence of linear dispersion of a Weyl cone, and quadratic dispersions. The interplay between these two dispersions led to a complex experimental scenario, in that while some experiments claimed the existence of non-trivial Berry curvature [69, 211], others obtained a trivial topological phase in NbP [212]. In $MoAs_2$, there might be linear band crossing along $X1$ to Y direction, which is about 200 meV above the Fermi level.

In spite of the trivial electronic band structure, the magnetotransport properties of $MoAs_2$ show striking similarities with TSMs and warrant further investigations. Although there is no conclusive evidence of the actual origin of such a large transverse MR, a few possible explanations have been proposed. For example, in TSMs, the electronic transport through the conducting surface state is

protected from backscattering by TRS. Under applied magnetic field, the TRS breaks and leads to increasing electron scattering, i.e., an increase in resistivity [62]. For $MoAs_2$, however, we have not obtained any signature of topology protected electronic band structure from our first-principle calculations. In several cases, the large MR and the low-temperature crossover behavior can also be described well using a semiclassical two-band model [73, 178]. The large MR then appears as a consequence of compensated electron-hole density. Indeed, this model works well to understand the observed magnetotransport properties in TMDs [71, 153, 181, 182, 183]. However, as is evident from the Hall measurements, the transport properties of $MoAs_2$ are dominated by electron-type charge carriers, which is far from any electron-hole compensation scenario. Moreover, in $MoAs_2$, the carrier density is much higher than in typical TSMs and almost comparable to that of a good metal. In order to realize large MR due to Lorenz force in metals, the primary requirement is that the quantity $\omega_c\tau >> 1$, where ω_c and τ are the cyclotron frequency and scattering time, respectively [149]. This condition is typically valid in ultraclean samples, where the mean free path (i.e., mobility) of the charge carriers is quite large. The low residual resistivity and prominent quantum oscillation indicate that this seems to be the case in $MoAs_2$. Furthermore, in $MoAs_2$, the value of RRR is very large and comparable to the highest reported values for TMDs [182]. RRR is generally considered as a measure of the sample quality and the value of the MR usually scales with this factor [182, 62]. Another important aspect is the open-orbit Fermi surface, which emerged from the theoretical calculations. As shown for the layered compound $PdCoO_2$ [213], such open-orbit Fermi surface leads to very small scattering rate and can also be the possible origin of the large MR in $MoAs_2$.

7.5 Summary and conclusions

To summarize the results, in this chapter, we have presented the systematic study of the magnetotransport and Fermi surface properties of a transition metal dipnictide $MoAs_2$. Magnetic field-induced resistivity plateau and large magnetoresistance have been observed, which are characteristics of a TSM. The MR shows a strong butterfly-like anisotropy, when the magnetic field is applied along different crystallographic directions. Unlike other isostructural compounds, Hall measurements for $MoAs_2$ reveal quite high carrier density with electron-type majority carriers. The Fermi surface properties have been analyzed from dHvA oscillation along three mutually perpendicular crystallographic directions. The observed Fermi pockets are largest among the members of the XPn_2 group and are highly anisotropic in nature. The first-principles calculations show that the band structure of $MoAs_2$ is significantly different from that for other TMDs. The Fermi surface mainly consists of one large electron-type pocket and an open-orbit hole pocket, which may be the reason for such high MR in this compound.

8

Planar Hall effect in type II Dirac semimetal VAl_3

8.1 Introduction

As discussed in Chapter 1, type-II TSMs host the Lorentz-violating Dirac and Weyl fermions, which are impossible to realize in relativistic particle physics. These quasiparticle excitations are predicted to exhibit several exotic physical phenomena [214, 215, 216]. Although type II Weyl fermions have been identified in few systems [43, 217, 218, 219, 220], the candidates for type II Dirac semimetals are rather limited [44, 221]. From first-principle calculations, the members of the family MA_3 (M=V, Nb, Ta; A=Al, Ga, In) are proposed to be type II Dirac semimetals [222]. The Dirac cone emerges at the contact point of electron and hole pockets and shows a mirror Chern number 2, which has not been observed in type I TSMs so far. This Dirac node splits into two quadratic Weyl nodes carrying chiral charges ± 2 under broken time-reversal symmetry. Each quadratic Weyl cone can be further broken

into two linearly dispersing Weyl cones, when the inherent C_4 rotational symmetry of the crystal structure is lifted. On the other hand, the material can be driven to a topological crystalline insulating state by breaking only the C_4 rotational symmetry. Therefore, MA_3 family offers an excellent prospect and tunability to study type II Dirac fermions as well as other exotic topological phases.

Identifying Dirac or Weyl fermions in a compound is a formidable task and requires sophisticated techniques such as ARPES. Nevertheless, the signatures of Dirac/Weyl fermions can be obtained in transport experiments. Large MR, small carrier effective mass, and ultra high carrier mobility are some of the characteristics of the TSMs and considered as primary criteria to propose new materials in this class [62, 69, 70, 92]. However, these prominent features are often hindered by parabolic bands near the Fermi energy. On the other hand, different mechanisms like electron-hole compensation [182] or open-orbit Fermi surface [223] can also lead to the above-mentioned properties. In addition, multiple Fermi pockets can make it very difficult to accurately extract the Berry phase from quantum oscillation. The ABJ chiral anomaly is widely accepted as a direct evidence of the Dirac/Weyl cones in the electronic band structure [76, 81, 168, 224]. This relativistic effect originates from the non-conservation of the number of Weyl fermions with a particular chirality and results in negative MR under parallel electric and magnetic fields [76, 168]. To observe this phenomenon, the necessary condition is to have the Dirac/Weyl nodes very close to the Fermi energy [81, 224], which is not the case for most of the TSMs. As these compounds show large positive MR under transverse electric and magnetic field, a small misalignment between these two can easily mask the weak negative MR component [76]. In addition, other mechanisms such as current jetting [190], weak localization [225] can also gener-

ate negative MR. Therefore, it is very difficult to distinguish the chiral anomaly induced negative MR from other effects. Recently, from theoretical calculations, a planar Hall effect (PHE) has been predicted in TSMs, which appears due to the ABJ chiral anomaly and non-trivial Berry curvature [226, 227]. As PHE is completely different from conventional Hall effect, both in experimental configuration and angle dependence, this phenomenon is easier to identify and unambiguously confirms the Dirac/Weyl type excitations in the system. Large PHE has been reported in topological insulator $ZrTe_5$ [228], Dirac semimetal Cd_3As_2 [229], and Weyl semimetals WTe_2 [230] and GdPtBi [231]. We note that a weak PHE can also be observed in ferromagnetic compounds due to magnetic ordering [232]. However, this effect does not arise in TSMs as most of these systems are non-magnetic.

In this chapter, we present the magnetotransport properties of proposed type II Dirac semimetal VAl_3. Large non-saturating MR has been observed together with large carrier mobility. The non-linear field dependence of Hall resistivity reveals the presence of both electron and hole type carriers, as predicted from the theoretical calculations. We have observed a prominent PHE, which persists up to high temperature and confirms the non-trivial nature of the electronic band structure in this material.

8.2 Sample preparation, characterization, and experimental details

We have grown the single crystals of VAl_3 in aluminium-flux [45]. High purity V granules (Alfa Aesar 99.8%) and Al pieces (Alfa Aesar 99.999%) were taken in 1:9 molar ratio in an alumina crucible. The crucible was then sealed in a evacuated

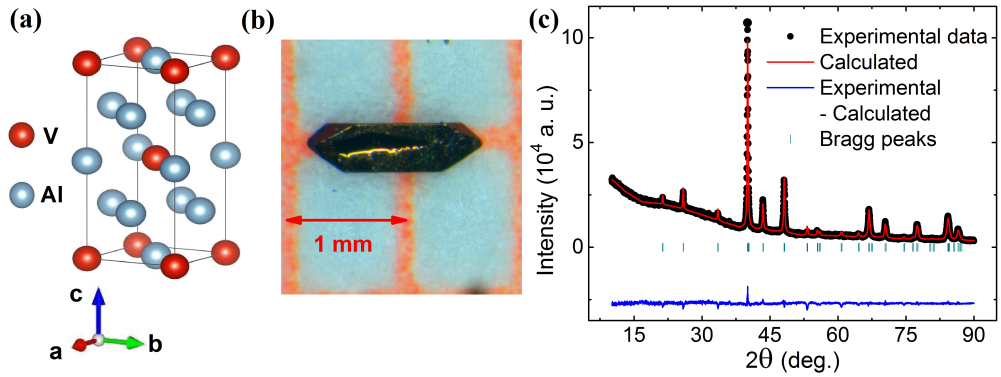

Figure 8.1: (a) Crystal structure of VAl_3. (b) A typical single crystal of VAl_3 with appropriate length scale. (c) XRD spectra of the powdered single crystals. The experimental data have been analyzed by Rietveld structural refinement.

quartz tube. The tube was heated to 950°C and kept at this temperature for 12 hrs. After that it was slowly cooled (3°C/h) to 750°C. At this temperature, the excess aluminium flux was decanted using a centrifuge. Several needle like single crystals with typical dimensions 1.5×0.3×0.2 mm^3 were extracted, which were further etched using sodium hydroxide solution to get rid of any remaining aluminium on the surface. The phase purity of the crystals was confirmed by powder XRD and HRTEM. The elemental composition was checked using EDX spectroscopy. We performed the transport measurements via four probe technique in a Quantum Design 9 T PPMS with horizontal sample rotator option. The electrical contacts were made with gold wire and conducting silver paint.

VAl_3 crystallizes in a tetragonal structure with crystallographic symmetry $I4/mmm$ (space group no. 139) [222, 233]. As evident from the crystal structure in Figure 8.1(a), each Al atom is surrounded by four neighboring V atoms either in planar square or tetrahedron geometry. The image of a typical single crystal is shown in Figure 8.1(b) with appropriate length scales. Figure 8.1(c) represents the XRD pattern of the powdered crystals. We have analyzed the experimental data by

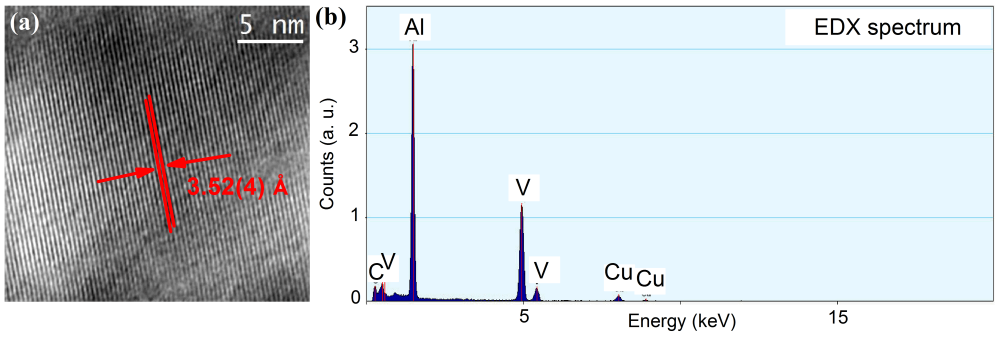

Figure 8.2: (a) The HRTEM image of the as grown VAl_3 crystal. (b) EDX spectroscopy spectrum of a typical single crystal.

Rietveld structural refinement using FULLPROF software package. The refined lattice parameters, a=b=3.777(2) and c=8.324(5) Å, are in excellent agreement with those reported earlier [233]. The absence of any impurity peak within our experimental resolution, confirms the phase purity of the grown single crystals. The HRTEM image of a typical single crystal along ab-plane is shown in Figure 8.2(a), which reveals the high quality crystalline nature of the sample. The calculated interplanar spacing 3.52(4) Å is consistent with the extracted lattice parameters from XRD data. We have also performed EDX spectroscopy on the as grown single crystals to check the elemental composition. From the experimental data [Figure 8.2(b)], we have obtained the V and Al atomic ratio to be 1:2.8 with maximum relative error ∼5%, which is close to the desired stoichiometry. The C and Cu signals in EDX spectrum come from the carbon coated copper grid, on which the sample was mounted for HRTEM.

8.3 Results and discussion

8.3.1 Temperature dependence of resistivity and transverse magnetoresistance

In Figure 8.3(a), we have plotted the longitudinal resistivity (ρ_{xx}) of a typical single crystal as a function of temperature. VAl_3 shows metallic character, i.e., ρ_{xx} decreases monotonically from room temperature. At 2 K, the resistivity becomes $\sim$9.3 $\mu\Omega$ cm and yields a residual resistivity ratio [ρ_{xx}(300 K)/ρ_{xx}(2 K)] $\sim$12. As shown in the inset, ρ_{xx} follows a quadratic temperature dependence in the low temperature region, which is consistent with the Fermi liquid theory [64]. Above 100 K, the resistivity increases linearly with temperature. With the application of magnetic field perpendicular to the current, the resistivity in the low temperature region, increases. However, within the applied field range, we have not observed any field-induced metal-semiconductor-like crossover as in the case of most TSMs [69, 70, 76, 92]. Next, the magnetic field dependence of the resistivity has been measured at different temperatures [Figure 8.3(b)]. With transverse magnetic field and current, a large, non-saturating MR $\sim$158 % has been observed at 2 K and 9 T. This MR value is two to three orders of magnitude smaller than that for a typical TSM [62, 69, 70, 76, 92]. The electronic band structure of VAl_3 consists of several parabolic bands, which cross the Fermi energy [222]. Hence, we expect that the transport properties are dominated by the carriers associated with these trivial Fermi pockets. With increasing temperature, the MR reduces drastically and becomes almost negligible at 300 K. In the inset of Figure 8.3(b), we have fitted $\rho_{xx}(B)$ using a αB^m type power-law with m $\sim$1.3, where α is an arbitrary param-

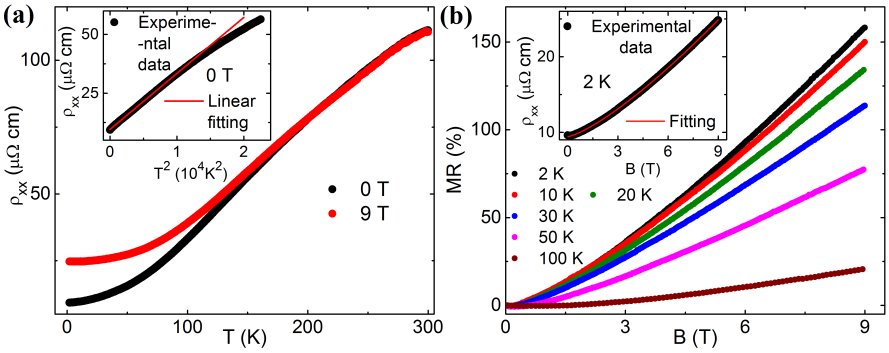

Figure 8.3: (a) Temperature dependence of the longitudinal resistivity (ρ_{xx}) for VAl_3 without and with a transverse magnetic field. The inset shows the T^2 dependent behavior of ρ_{xx} at low temperature. (b) Transverse magnetoresistance at different temperatures. In the inset, we have fitted the experimental data using αB^m-type power-law.

eter. In semiclassical two-band theory, a quadratic field dependence is expected for compensated semimetals with equal density of electron and hole type charge carriers [64]. For VAl_3, however, $m \neq 2$ suggests an uncompensated scenario.

8.3.2 Conventional Hall measurement

We have performed the Hall resistivity measurement to obtain further information about the carrier density and mobility of the charge carriers. In Figure 8.4(a), the Hall resistivity (ρ_{yx}) is plotted as a function of magnetic field for few representative temperatures. At 300 K, $\rho_{yx}(B)$ is almost linear and negative, confirming that the majority carrier is electron type. With decreasing temperature, a non-linear behavior emerges and persists down to 2 K. The non-linear magnetic field dependence of Hall resistivity reveals the presence of more than one type of charge carrier and different temperature dependence of their mobilities. As shown in Figure 8.4(b), we have calculated the Hall conductivity (σ_{xy}) using the tensorial inversion of the resistivity matrix, $\sigma_{xy}=\frac{\rho_{yx}}{\rho_{yx}^2+\rho_{xx}^2}$. The experimental data have been fitted [Figure

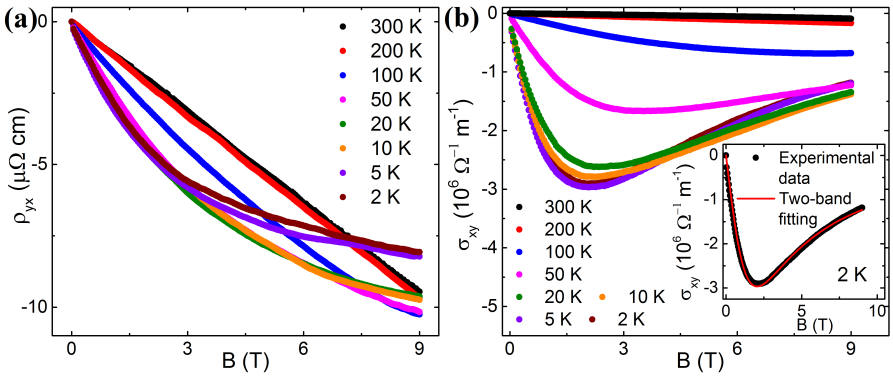

Figure 8.4: (a) Hall resistivity as a function of magnetic field at different temperatures. (b) Field dependence of the calculated Hall conductivity. Inset illustrates the two-band fitting of σ_{xy} at 2 K as a representative.

8.4(b) inset] using the semiclassical two-band theory [89]. From the fitting parameters, the calculated electron and hole densities are $7.7(3)\times10^{19}$ and $3.7(1)\times10^{19}$ cm^{-3}, respectively at 2 K. Similarly, at 2 K, we have found the mobility of the electrons and holes to be $4.8(1)\times10^{3}$ and $0.3(2)\times10^{3}$ $cm^2V^{-1}s^{-1}$, respectively. These values confirm that the magnetotransport properties in VAl_3 are primarily dominated by electron-type charge carrier. The obtained carrier density and mobility are comparable to those reported for several TSMs [150, 152, 155].

8.3.3 Planar Hall measurement

Identifying the topological nature of the electronic band structure in VAl_3 is of fundamental interest to verify the theoretical prediction of the type II Dirac fermions in this compound [222]. However, the complex band structure, which consists of several bands coexisting at the Fermi energy [222], makes it extremely difficult to probe the Dirac cone from low-energy experiments. In fact, due to this reason, quantum oscillation study on the members of the MA_3 family could not confirm the Berry phase corresponding to different Fermi pockets [234]. On the other hand,

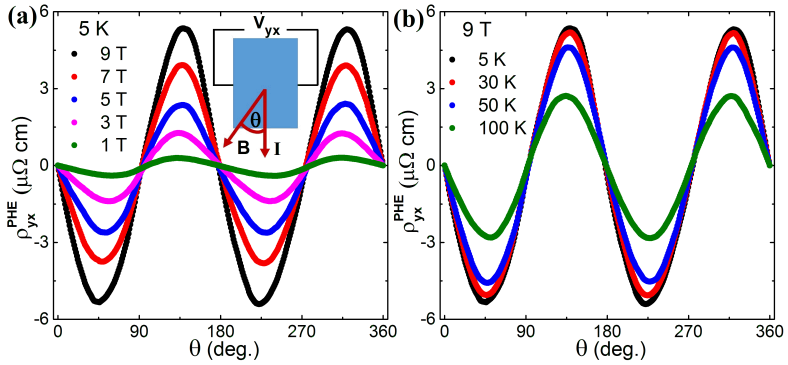

Figure 8.5: (a) Angle dependence of the planar Hall resistivity at 5 K for different magnetic field strengths. The schematic in the inset shows the experimental set-up. (b) Angle dependence of ρ_{yx}^{PHE} at 9 T for different temperatures.

PHE does not possess such shortcoming and is a direct evidence of the Dirac or Weyl fermions in the system [226, 227]. In the inset of Figure 8.5(a), we have shown the experimental set-up for PHE measurement, where the current, applied magnetic field and the Hall voltage (V_{yx}) are coplanar. During the measurement, magnetic field is rotated within this plane. Here, θ is the angle between the current and magnetic field. In Figure 8.5(a), the angle dependence of the planar Hall resistivity (ρ_{yx}^{PHE}) is shown for VAl_3 at 5 K for different magnetic field strengths. To eliminate any contribution from the conventional Hall effect, we did the measurements with both positive and negative magnetic field directions and took the average. ρ_{yx}^{PHE} exhibits a periodic behavior with the amplitude decreasing with decreasing magnetic field strength. The most striking feature of PHE is the position of the extrema points. Due to the nature of the Lorentz force, the Hall resistivity is zero for a magnetic field applied parallel to the current, whereas it becomes extremum when current, magnetic field, and Hall voltage are mutually perpendicular for conventional Hall measurements. In Figure 10.2 (Appendix B), we have shown the conventional Hall resistivity of VAl_3 as a function of the angle between the

current and magnetic field. As expected, ρ_{yx} becomes maximum and minimum at 90° and 270°, respectively. In PHE, the experimental configuration ensures that there is no Lorentz force. As evident from Figure 8.5(a), the experimental data show minima and maxima at 45° (and 225°) and 135° (and 315°), respectively. These positions of extrema are consistent with the theoretically predicted PHE [227] and confirm the non-trivial nature of the electronic band structure in VAl_3. On the other hand, conventional metals and semiconductors with trivial band structure, are not expected to show PHE (Appendix B: Figure 10.3). PHE can be mathematically formulated from the semiclassical Boltzmann theory [226, 227],

$$\rho_{yx}^{PHE} = -\Delta\rho_{chiral} \sin\theta \cos\theta \tag{8.1}$$

$$\rho_{xx}^{planar} = \rho_{\perp} - \Delta\rho_{chiral} \cos^2\theta \tag{8.2}$$

where $\Delta\rho_{chiral} = \rho_{\perp} - \rho_{\parallel}$ is the chiral anomaly induced resistivity component and ρ_{xx}^{planar} represents the planar resistivity. $\rho_{\perp}$ and $\rho_{\parallel}$ are the resistivity for current applied perpendicular (transverse resistivity) and parallel to the magnetic field direction, respectively. In Figure 8.5(b), we have plotted ρ_{yx}^{PHE} for different temperatures at applied magnetic field 9 T. ρ_{yx}^{PHE} shows weak temperature dependence and remains quite large and detectable at 100 K and above. This behavior is in sharp contrast to the chiral anomaly induced negative LMR, which disappears quickly with increasing temperature [76, 81, 168, 224]. One of the reasons is the unavoidable small misalignment between electric and magnetic field, which contributes an additional positive TMR component. Both LMR and TMR have different temperature dependence. Hence, with increasing temperature, they compete with each other. If the misalignment angle is slightly larger and the TMR is

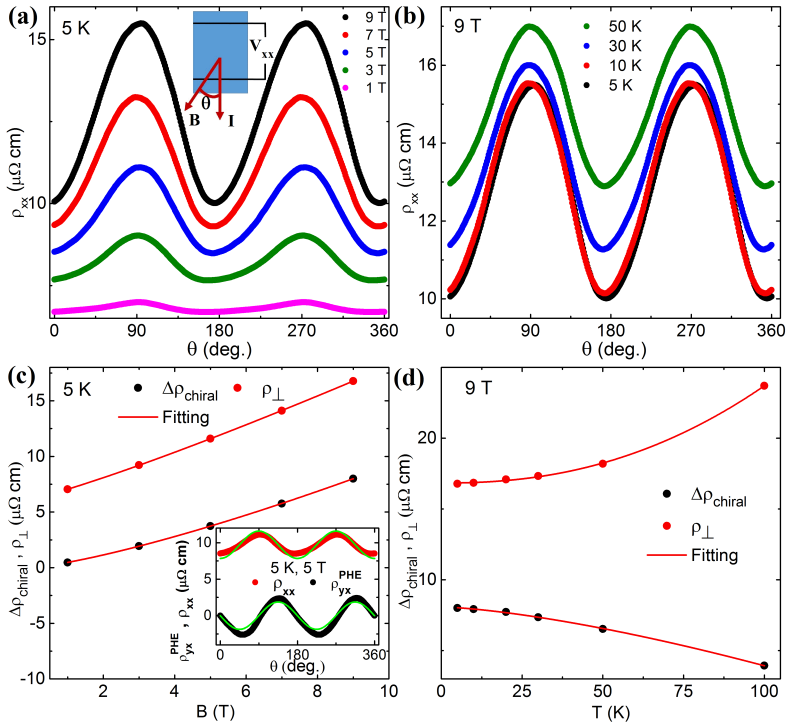

Figure 8.6: (a) Anisotropy in planar resistivity for different magnetic field strengths. The inset shows the measurement set-up. (b) Angle dependence of ρ_{xx}^{planar} at different temperatures. (c) The magnetic field dependence of the extracted chiral anomaly induced resistivity component and transverse resistivity. Inset shows the global fitting of ρ_{yx}^{PHE} and ρ_{xx}^{planar} using Equations. 8.2 and 8.3. (d) The temperature dependence of $\Delta\rho_{chiral}$ and $\rho_{\perp}$ at 9 T.

a slowly varying function of temperature as compared to LMR, then above a certain temperature, the negative LMR becomes too weak to detect experimentally [76, 81, 168, 224]. We have also measured the planar resistivity ρ_{xx}^{planar} for different magnetic field and temperature combinations. The experimental set-up has been shown schematically in the inset of Figure 8.6(a). In Figures 8.6(a) and (b), ρ_{xx}^{planar} has been plotted for different magnetic field strengths at 5 K and for different temperatures at 9 T, respectively. ρ_{xx}^{planar} shows a periodicity π with maximum at 90° and 270°, i.e., when applied magnetic field and current are in transverse configuration. To further confirm the nature of the PHE, we have fitted ρ_{yx}^{PHE} and ρ_{xx}^{planar}

using the theoretical Equations 8.1 and 8.2. As shown in the inset of Figures 8.6(c), our global fitting is in excellent agreement with the experimental data. From the fitting parameters, we have extracted the values of chiral resistivity and transverse resistivity components. Both of these quantities increase monotonically with magnetic field and follow a B^n-type relation with $n \sim 1.3$ [Figure 8.6(c)]. Figure 8.6(d) illustrates the temperature dependence of $\Delta\rho_{chiral}$ and $\rho_\perp$. As expected, at 9 T, $\Delta\rho_{chiral}$ decreases with increasing temperature. The experimental results can be described well by $\Delta\rho_{chiral} = C_1 - C_2T^{1.4}$ type power law, where C_1 and C_2 are arbitrary constants. On the other hand, $\rho_\perp$ shows almost quadratic temperature dependence.

8.4 Summary and conclusions

In conclusion, we have analyzed the electronic transport properties of single crystalline VAl_3. A large non-saturating MR has been observed along with high carrier mobility in this material. The magnetic field dependence of Hall resistivity reveals the presence of both electron and hole type charge carriers. From our measurements, a large planar Hall effect has been identified. This effect is robust and detectable up to quite high temperature. As planar Hall effect originates from the relativistic ABJ chiral anomaly and non-trivial Berry phase, it is an excellent tool to verify the presence of Dirac or Weyl fermions in a system. Hence, our experimental results unambiguously confirm the theoretically predicted type II Dirac semimetal phase in VAl_3. This material represents a large family (MA_3) of isostructural compounds, which are all predicted to be type II Dirac semimetals. Materials with identical crystal and electronic band structures offer a wide range of tunability of the electronic state, simply by varying the chemical composition or

doping. For example, SOC is an crucial parameter, which significantly influences the topological phases in a system. With increasing atomic number (Z) from V (Z=23) to Ta (Z=73), one can effectively change the SOC and hence can tune the electronic properties of the system. On the other hand, through doping, we can move the chemical potential closer to the type II Dirac node and make it easily accessible by low energy experiments. Therefore, our results present a detailed study on VAl_3 as well as encourage further investigation on the other members of the MA_3 family.

9

Summary and scope for future work

9.1 Summary

In the present thesis, we have probed the topological state, Fermi surface, electronic transport properties, and lattice dynamics of some topological semimetals. We have been motivated by earlier theoretical predictions and in few cases preliminary experimental reports. In this thesis work, our goal remains twofold. Firstly, we experimentally confirm the novel topological quantum states in new materials and try to understand the crystallographic symmetries, which protect such band structure. Secondly, we have analyzed the electronic transport properties in these systems to reveal the exciting features, relevant for fundamental physics as well as technological applications. To explain these phenomena, particular emphasis has been given on the Fermi surface properties, which govern the scattering mechanisms in a material.

These topological materials (ZrSiS, LaSbTe, LaBi, $MoAs_2$, and VAl_3) have been synthesized in single crystalline form. In Chapter 3, we have presented the mag-

netotransport properties of ZrSiS, a theoretically proposed nodal-line semimetal with highest reported energy range (∼2 eV) of linearly dispersing bands. We have observed very large and non-saturating MR ∼1.4×10^5 % at 2 K and 9 T magnetic field. This is among the highest reported values for any material so far. Interestingly, this MR is highly anisotropic because of the quasi two-dimensional nature of the Fermi surface. Under parallel electric and magnetic field, ZrSiS shows the Adler-Bell-Jackiw chiral anomaly, a long-sought relativistic phenomenon of massless Dirac fermions. By analyzing the crystallographic direction dependent quantum oscillation in resistivity and magnetization, we have constructed the complete Fermi surface and calculated several related parameters. These oscillations also enabled us to confirm the non-trivial Berry phase and hence the Dirac fermionic nature of the charge carriers. Hall resistivity measurements reveal the presence of both electron and hole-type carriers and their very large mobility. By combing the quantum oscillation and Hall effect results, we show that ZrSiS hosts multiple Dirac nodes at different energy values, which is in accordance to the band structure calculations.

As discussed in Chapter 1, crystallographic symmetries play a key role in protecting the topologically non-trivial electronic states in a material. ZrSiS has a layered structure, where the Si atom sublattice essentially dictates the topological properties. Furthermore, ZrSiS represents a large family of compounds (*WHM* with *W*=Zr, Hf, La; *H*=Si, Ge, Sn; *M*=O, S, Se, Te), all of which have identical band structure. Therefore, a systematic study on the phonon subsystem can shed some light to understand the topological nodal-line phase in this family of materials. In Chapter 4, we have investigated the lattice dynamics and electron-phonon interaction in ZrSiS using Raman spectroscopy. We have analyzed the polarization

and angle-resolved Raman data using crystal symmetries and theoretically calculated atomic vibrational patterns as well as phonon dispersion spectra. Wavelength and temperature-dependent measurements reveal the complex interplay of electron and phonon degrees of freedom, leading to resonant phonon and quasielastic electron scattering through interband transition. The high-pressure Raman studies show vibrational anomalies, which are the signature of structural phase transitions. Further investigations, using high-pressure synchrotron x-ray diffraction technique, clearly show pressure-induced structural transitions and coexistence of multiple phases, which also suggest possible electronic topological transitions in ZrSiS.

The materials in the *WHM* family have been theoretically proposed to be weak topological insulators. However, several members including ZrSiS have been experimentally confirmed as topological nodal-line semimetals. In Chapter 5, we present the magnetotransport and magnetization properties of LaSbTe, a member of the *WHM* family with somewhat distinct structural parameters. We have observed magnetic-field-induced turn-on behavior and low-temperature resistivity plateau. The possible origin of the temperature and magnetic field dependence of resistivity have been discussed by adopting both metal-semiconductor crossover and Kohler scaling analysis. A large, nonsaturating transverse MR $\sim 5\times10^3$ % has been obtained at 5 K and 9 T. The MR shows significant anisotropy, when the magnetic field is applied along different crystallographic directions. The nonlinear magnetic field dependence of the Hall resistivity confirms the presence of two types of charge carriers. From the semiclassical two-band fitting of Hall conductivity and longitudinal conductivity, we have deduced very high carrier mobilities and almost equal electron and hole densities, which result in large MR. The Fermi surface

properties have been analyzed from dHvA oscillation. From the magnetization measurement, we have detected the signature of the nontrivial surface state, which confirms that LaSbTe is a topological insulator, consistent with the earlier band structure calculations.

Extremely large MR and ultrahigh carrier mobility are two major hallmarks of topological materials and frequently used as primary criteria to identify new compounds belonging to this class. While LaBi shows the aforementioned properties, the topological nature of its electronic band structure remains unresolved. In Chapter 6, using the magnetotransport and magnetization measurements, we have probed both the bulk and surface states of LaBi. We have observed extremely large MR and high carrier mobility with compensated electron and hole density. The Fermi surface properties have been analyzed from both SdH and dHvA oscillation techniques. A prominent paramagnetic singularity has been observed in the magnetization measurement, which demonstrates the non-trivial nature of the surface state. Our study unambiguously confirms that LaBi is a three-dimensional topological insulator with possible linear dispersion in the gapped bulk band structure.

Transition-metal dipnictides have been identified as potential candidates to host a topology protected electronic band structure. These materials represent an isostructural family and show several exotic transport properties. Especially, the large values of MR and carrier mobility have attracted significant attention from the perspective of technological applications. In Chapter 7, we have investigated the magnetotransport and Fermi surface properties of $MoAs_2$, another member of this group. A field-induced resistivity plateau and a large MR have been observed, which are comparable to those in several topological systems. Interestingly, in

contrast to other isostructural systems, the carrier density in $MoAs_2$ is quite high and the transport properties are dominated by a single band. The Fermi pockets, which have been analyzed from the quantum oscillation, are the largest among the members of this family and have significant anisotropy. The results of our first-principles calculations reveal a substantial difference between the band structures of $MoAs_2$ and that of other TMDs. The Fermi surface consists of one electron pocket and another 'open-orbit' hole pocket, which has not been observed in TMDs so far.

From theoretical calculations, VAl_3 has been proposed to be a type II topological Dirac semimetal. This compound represents a large family of isostructural materials, all having similar band structure and is an ideal system to explore Lorentz symmetry violating Dirac fermions. In Chapter 8, we present a detailed analysis on the magnetotransport properties of VAl_3 single crystals. A large, non-saturating MR has been observed. Hall measurements show the presence of two types of charge carriers with high mobility. Our measurements reveal a large planar Hall effect in this material, which is robust and easily detectable up to high temperature. This phenomenon originates from the relativistic chiral anomaly and nontrivial Berry phase, which confirms the theoretical prediction of the Dirac semimetal phase in VAl_3.

9.2 Scope for future work

9.2.1 Topological materials under extreme conditions - high magnetic field and high pressure

One of the interesting aspects of topological materials is the emergence of exotic quantum phases under extreme conditions, i.e., very high magnetic field and pressure. Such study can unveil the exciting properties in the quantum limit regime and can be extremely fruitful to understand the complex physics of topological materials. At very high magnetic field, electrons can be pushed to the lowest Landau level (n=1), i.e., towards the quantum limit. In this limit, we look for novel transport phenomena such as linear MR, quantum phase transition, etc [85, 235, 236]. For example, in ZrSiS, very large magnetic field ($\sim$33 T) lead to enhanced correlation effects and magnetic breakdown across gaps in the nodal-line structure [237]. This results in unconventional enhancement of the effective mass of the charge carriers. External pressure is a clean way to tune the lattice as well as electronic states without introducing complex band structure as in chemical doping. In fact, several topological semimetals have been reported to show superconductivity under applied pressure [238, 239, 240, 241]. The study of superconductivity in topological systems has its own importance due to the possibility of realizing the elusive Majorana fermions [242] to rejuvenate the field of quantum computation [243]. External pressure can also modulate the chemical potential in a material making Dirac nodes at different energy values accessible through low energy transport experiments.

9.2.2 Excitations beyond Dirac or Weyl fermions

So far, the main efforts in topological band theory has been focused in searching for high-energy particles such as Dirac, Weyl or Majorana fermions in condensed matter systems. However, there is a fundamental difference in the formulation of quasiparticle excitations in condensed matter and relativistic particle physics. While quantum field theory is constrained by Poincare symmetry, a real material only obeys crystal symmetry of one of the 230 space groups. Therefore, it is possible to realize new type of particles in condensed matter systems that have no counterpart in high-energy physics. As we have already discussed, Lorentz symmetry violating Dirac/Weyl fermions can only be found in condensed matter physics. In 2016, Bradlyn *et al.* have predicted a wide range of new free fermionic excitations that appear at three, six, and eight-fold degenerate linear or quadratic band crossings, which are protected by space group symmetries [244]. They have also proposed several materials, where such particles can be discovered. Indeed, three-component fermions have already been observed in MoP [245] and WC [246].

9.2.3 Topological semimetal based electronic devices

The non-trivial band structure of topological materials have stimulated enormous interest in spintronics technology. There are numerous proposals of topological insulator based electronic devices, which particularly utilize the spin-polarization of the surface state [247, 248, 249, 250, 251]. On the other hand, large MR and ultra-high mobility in topological semimetals can be used in magnetic sensors, magnetic switch, memory devices, and highly efficient low-power electronics [252]. Recently, topological semimetals have also been shown to be highly photosensitive and can be

used for optoelectronics and photonics applications [253, 254]. Therefore, finding suitable topological materials for such technological use is one of the emerging fields of research.

10

Appendix

10.1 Appendix A

10.1.1 Magnetization measurement for standard samples

The results of the magnetization measurement for standard diamagnetic (Bi) and paramagnetic (Pd) samples are shown in Figure 10.1. In both the cases, no cusp-like feature has been observed in the magnetic susceptibility data around $B = 0$.

10.2 Appendix B

10.2.1 Angle dependence of conventional Hall resistivity

In Figure 10.2, we have plotted the conventional Hall resistivity of VAl_3 as a function of the angle between current and magnetic field. The experimental set-up has been shown schematically in the inset. Due to the nature of the Lorentz force, ρ_{yx} becomes zero and extremum, when current and applied magnetic field are parallel

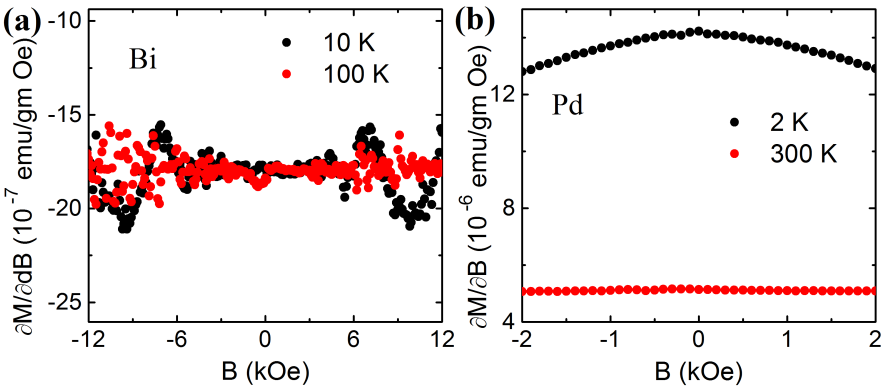

Figure 10.1: Magnetic susceptibility χ ($=\partial M/\partial B$) of (a) bismuth and (b) palladium at different temperatures.

and perpendicular to each other, respectively.

10.2.2 Planar Hall effect measurement in conventional metal or semiconductor

To identify the nature of the angular dependence of planar Hall effect, we can also perform such experiments in ordinary metals and semiconductors. However, the results can be predicted from the very nature of the Lorentz force, which is the only contributing factor in those materials. As shown in Figure 10.3, for PHE, the magnetic field is rotated in the plane of current and voltage probes (xy-plane). In this configuration, Lorentz force dictates that the charge carriers will only be scattered along the out of plane direction (z-direction as shown by the dotted arrows). So, in such case, we expect to observe a Hall voltage only along the z-direction, which should show a two-fold symmetry (i.e., extrema at 90° and 270°). The arrangements of the voltage probes ensure that the measured signal along the x-direction is not get affected by these scattered electrons or holes. So there

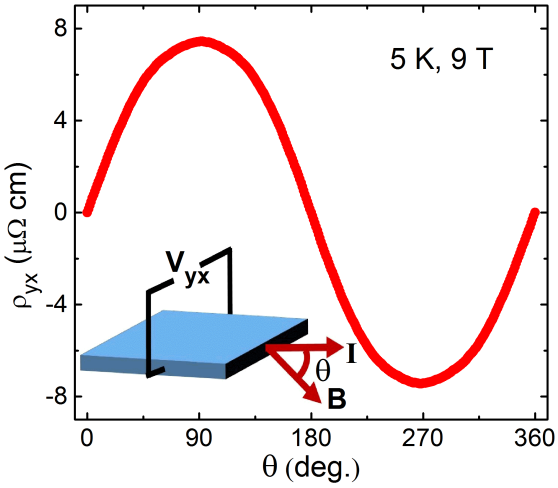

Figure 10.2: Directional dependence of conventional Hall resistivity for VAl_3. The inset schematically illustrates the experimental set-up.

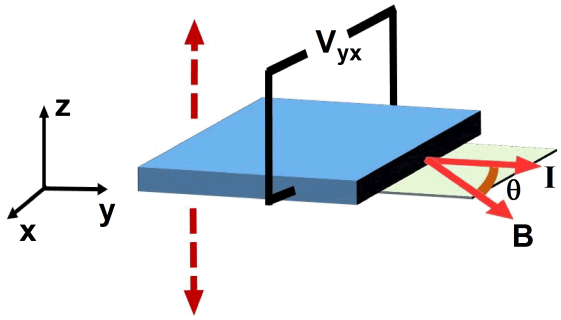

Figure 10.3: Schematic illustrating the expected results of planar Hall effect measurement in conventional metal or semiconductor.

will be no PHE in conventional metals or semiconductors. In addition, in metals, the conventional Hall resistivity is always temperature independent. However, as chiral anomaly is a function of temperature, the PHE in topological semimetals shows a strong temperature dependence.

Bibliography

[1] K. v. Klitzing *et al.*, Phys. Rev. Lett. **45**, 494 (1980).

[2] K. v. Klitzing, Phil. Trans. R. Soc. London, Ser. A **363**, 2203 (2005).

[3] M. Nakahara, *Geometry, Topology and Physics*, 2nd edition, Institute of Physics Publishing, Bristol and Philadelphia (2003).

[4] M. Z. Hasan *et al.*, Rev. Mod. Phys. **82**, 3045 (2010).

[5] X.-L. Qi *et al.*, Rev. Mod. Phys. **83**, 1057 (2011).

[6] D. J. Thouless *et al.*, Phys. Rev. Lett. **49**, 405 (1982).

[7] F. D. M. Haldane, Phys. Rev. Lett. **61**, 2015 (1988).

[8] B. A. Bernevig *et al.*, Phys. Rev. Lett. **96**, 106802 (2006).

[9] B. A. Bernevig *et al.*, Science **314**, 1757 (2006).

[10] M. König *et al.*, Science **318**, 766 (2007).

[11] S. Murakami, New J. Phys. **9**, 356 (2007).

[12] X.-L. Qi *et al.*, Physics Today **63**, 33 (2010).

[13] C. L. Kane *et al.*, Phys. Rev. Lett. **95**, 146802 (2005).

[14] L. Fu *et al.*, Phys. Rev. Lett. **98**, 106803 (2007).

[15] L. Fu *et al.*, Phys. Rev. B **76**, 045302 (2007).

[16] J. E. Moore *et al.*, Phys. Rev. B **75**, 121306(R) (2007).

[17] Z. Ringel *et al.*, Phys. Rev. B **86**, 045102 (2012).

[18] D. Hsieh *et al.*, Nature **452**, 970 (2008).

[19] H. Zhang *et al.*, Nat. Phys. **5**, 438 (2009).

[20] Y. L. Chen *et al.*, Science **325**, 178 (2009).

[21] Y. Xia *et al.*, Nat. Phys. **5**, 398 (2009).

[22] D. Hsieh *et al.*, Phys. Rev. Lett. **103**, 146401 (2009).

[23] S.-Y. Xu *et al.*, Science **332**, 560 (2011).

[24] S. M. Young *et al.*, Phys. Rev. Lett. **108**, 140405 (2012).

[25] Z. Wang *et al.*, Phys. Rev. B **85**, 195320 (2012).

[26] Z. Wang *et al.*, Phys. Rev. B **88**, 125427 (2013).

[27] S.-Y. Xu *et al.*, Science **347** 294 (2015).

[28] Z. K. Liu *et al.*, Science **343**, 864 (2014).

[29] Z. K. Liu *et al.*, Nat. Mater. **13**, 677 (2014).

[30] H. Yi *et al.*, Sci. Rep. **4**, 6106 (2014).

[31] H. Weyl, Zeitschrift für Physik **56**, 330 (1929).

[32] W. W.-Krempa, Annu. Rev. Condens. Matter Phys. **5**, 57 (2014).

[33] X. Wan *et al.*, Phys. Rev. B **83**, 205101 (2011).

[34] H. Weng *et al.*, Phys. Rev. X **5**, 011029 (2015).

[35] S.-M. Huang *et al.*, Nat. Commun. **6**, 7373 (2015).

[36] S.-Y. Xu *et al.*, Science **349**, 613 (2015).

[37] B. Q. Lv *et al.*, Phys. Rev. X **5**, 031013 (2015).

[38] S.-Y. Xu *et al.*, Science Adv. **1**, e1501092 (2015).

[39] S.-Y. Xu *et al.*, Nat. Phys. **11**, 748 (2015).

[40] A. A. Burkov *et al.*, Phys. Rev. B **84**, 235126 (2011).

[41] C.-K. Chiu *et al.*, Phys. Rev. B **90**, 205136 (2014).

[42] G. Bian *et al.*, Nat. Commun. **7**, 10556 (2016).

[43] A. A. Soluyanov *et al.*, Nature **527**, 495 (2015).

[44] M. Yan *et al.*, Nat. Commun. **8**, 257 (2017).

[45] P. C. Canfield *et al.*, Phil. Mag. Part B **65**, 1117 (1992).

[46] R. J. Hill, *The Rietveld Method*, Oxford University Press (1995).

[47] J. R.-Carvajal, *An Introduction to the Program FullProf 2000*, Laboratoire Leon Brillouin, CEA-CNRS, Saclay (2001).

[48] A. P. Hammersley, *FIT2D: An Introduction and Overview*, ESRF, BP 220, 38043 Grenoble, France (1997).

[49] A. C. Larson *et al.*, *General Structure Analysis System (GSAS)*, Los Alamos National Laboratory Report LAUR 86-748 (1994).

[50] D. B. Williams and C. B. Carter, *Transmission Electron Microscopy: A textbook for Material Science*, Springer, New York (2009).

[51] J. H. Scofield, Rev. Sci. Instrum. **58**, 985 (1987).

[52] *Physical Properties Measurement System User Manual*, Quantum Design, USA (2002).

[53] *Magnetic Property Measurement System: SQUID VSM User Manual*, Quantum Design, USA (2009).

[54] C. V. Raman *et al.*, Ind. J. Phys. **2**, 387 (1928).

[55] C. V. Raman *et al.*, Nature **121**, 501(1928).

[56] R. Loudon, Adv. in Phys. **13**, 423(1964).

[57] H.-K. Mao *et al.*, Rev. Mod. Phys. **90**, 015007 (2018).

[58] P. Wang *et al.*, Phys. Rev. B **97**, 235202 (2018).

[59] Q. Xu *et al.*, Phys. Rev. B **92**, 205310 (2015).

[60] L. M. Schoop *et al.*, Nat. Commun. **7**, 11696 (2016).

[61] A. K. Haneveld *et al.*, Recueil des Travaux Chimiques des Pays-Bas **83**, 776 (1964).

[62] T. Liang *et al.*, Nat. Mater. **14**, 280 (2015).

[63] Y. Zhao *et al.*, Phys. Rev. X **5**, 031037 (2015).

[64] J. M. Ziman, *Electrons and Phonons*, Classics Series, Oxford University Press, New York (2001).

[65] F. F. Tafti *et al.*, Nat. Phys. **12**, 272 (2016).

[66] S. Sun *et al.*, New J. Phys. **18**, 082002 (2016).

[67] P. M. Hall *et al.*, Phys. Rev. **116**, 1447 (1959).

[68] X. Zhang *et al.*, Chem. Mater. **26**, 6638 (2014).

[69] C. Shekhar *et al.*, Nat. Phys. **11**, 645 (2015).

[70] M. N. Ali *et al.*, Nature **514**, 205 (2014).

[71] K. Wang *et al.*, Sci. Rep. **4**, 7328 (2014).

[72] Y. Kopelevich *et al.*, Phys. Rev. B **73**, 165128 (2006).

[73] Y. L. Wang *et al.*, Phys. Rev. B **92**, 180402(R) (2015).

[74] J. Hu *et al.*, Nat. Mat. **7**, 697 (2008).

[75] F. F. Tafti *et al.*, Proc. Natl. Acad. Sci. USA **113**, E3475 (2016).

[76] X. Huang *et al.*, Phys. Rev. X **5**, 031023 (2015).

[77] R. H. McKenzie *et al.*, Phys. Rev. B **57**, 11854 (1998).

[78] S. Adler, Phys. Rev. **177**, 2426 (1969).

[79] J. S. Bell *et al.*, Il Nuovo Cimento A. **60**, 47 (1969).

[80] H. B. Nielsen *et al.*, Phys. Lett. B **130**, 389 (1983).

[81] H. Li *et al.*, Nat. Commun. **7**, 10301 (2016).

[82] J. Xiong *et al.*, Science **350**, 413 (2015).

[83] N. Kikugawa *et al.*, Nat. Commun. **7**, 10903 (2016).

[84] D. Shoenberg, *Magnetic oscillations in metals*, Cambridge University Press (1984).

[85] A. Narayanan *et al.*, Phys. Rev. Lett. **114**, 117201 (2015).

[86] H. Murakawa *et al.*, Science **342**, 1490 (2013).

[87] A. A. Taskin *et al.*, Phys. Rev. B **84**, 035301 (2011).

[88] Y. Ando, J. Phys. Soc. Jpn. **82**, 102001 (2013).

[89] C. M. Hurd, *The Hall effect in metals and alloys*, Plenum Press, New York (1972).

[90] K. K. Huynh *et al.*, Phys. Rev. Lett. **106**, 217004 (2011).

[91] R. Lou *et al.*, Phys. Rev. B **93**, 241104(R) (2016).

[92] R. Singha *et al.*, Proc. Natl. Acad. Sci. USA **114**, 2468 (2017).

[93] M. N. Ali *et al.*, Sci. Adv. **2**, e1601742 (2016).

[94] J. Hu *et al.*, Phys. Rev. Lett. **117**, 016602 (2016).

[95] S. Caramazza *et al.*, Eur. Phys. J. B **91**, 35 (2018).

[96] C. Marini *et al.*, Phys. Rev. B **86**, 064103 (2012).

[97] P. Postorino *et al.*, Phys. Rev. B **65**, 224102 (2002).

[98] H. Mao *et al.*, J. Geophys. Res. **91**, 4673 (1986).

[99] P. Hohenberg *et al.*, Phys. Rev. **136**, B864 (1964).

[100] W. Kohn *et al.*, Phys. Rev. **140**, A1133 (1965).

[101] G. Kresse *et al.*, Phys. Rev. B **47**, 558(R) (1993).

[102] G. Kresse *et al.*, Comput. Mater. Sci. **6**, 15 (1996).

[103] G. Kresse *et al.*, Phys. Rev. B **54**, 11169 (1996).

[104] P. E. Blöchl, Phys. Rev. B **50**, 17953 (1994).

[105] G. Kresse *et al.*, Phys. Rev. B **59**, 1758 (1999).

[106] J. P. Perdew *et al.*, Phys. Rev. Lett. **77**, 3865 (1996).

[107] G. Kresse *et al.*, Europhys. Lett. **32**, 729 (1995).

[108] K. Parlinski *et al.*, Phys. Rev. Lett. **78**, 4063 (1997).

[109] A. Togo *et al.*, Scr. Mater. **108**, 1 (2015).

[110] A. Togo *et al.*, Phys. Rev. B **78**, 134106 (2008).

[111] Baroni *et al.*, Rev. Mod. Phys. **73**, 515 (2001).

[112] W. Tremel *et al.*, J. Am. Chem. Soc. **109**, 124 (1987).

[113] P. Haas *et al.*, Phys. Rev. B **79**, 085104 (2009).

[114] B. Salmankurt *et al.*, Phil. Mag. 10.1080/14786435.2016.1250967 (2016).

[115] P. Yu, M. Cardona, *Fundamentals of Semiconductors: Physics and Materials Properties*, 4th edition, Springer-Verlag, Berlin (2010).

[116] X. Ma *et al.*, Phys. Rev. B **94**, 214105 (2016).

[117] M. B. Schilling *et al.*, Phys. Rev. Lett. **119**, 187401 (2017).

[118] A. Sharafeev *et al.*, Phys. Rev. B **95**, 235148 (2017).

[119] B. H. Bairamov *et al.*, Phys. Rep. **229**, 221 (1993).

[120] Y. Gillet *et al.*, Phys. Rev. B **88**, 094305 (2013).

[121] M. Klein, *Light Scattering in Solids I*, Topics in Applied Physics Vol. 8, edited by M. Cardona, Springer, Berlin, pp. 147-204 (1983).

[122] H.-M. Eiter *et al.*, Phys. Rev. B **90**, 024411 (2014).

[123] A. Duzynska *et al.*, Appl. Phys. Lett. **105**, 213105 (2014).

[124] A. Taube *et al.*, ACS Appl. Mater. Interfaces **6**, 8959 (2014).

[125] A. C. Ferrari, Solid State Commun. **143**, 47 (2007).

[126] J. S. Bae *et al.*, J. Korean Phys. Soc. **48**, 946 (2006).

[127] Y. A. Sorb *et al.*, J. Phys. Condens. Matter **25**, 155401 (2013).

[128] N. Subramanian *et al.*, Phys. Rev. B **58**, R555(R) (1998).

[129] C. Wang *et al.*, Inorg. Chem. **34**, 5524 (1995).

[130] R. Schmelczer *et al.*, Zeitschrift für Naturforschung B, 10.1515/znb-1981-0412 (1981).

[131] A. Bera *et al.*, Phys. Rev. Lett. **110**, 107401 (2013).

[132] V. Gnezdilov *et al.*, Phys. Rev. B **89**, 195117 (2014).

[133] M. Eddrief *et al.*, Nanotechnology **25**, 245701 (2014).

[134] N. Yedukondalu *et al.*, Phys. Rev. B **83**, 165117 (2011).

[135] H. Barninghaausen *et al.*, Zeitschrift für anorganische und allgemeine Chemie **338**, 250 (1965).

[136] E. B. Brackett *et al.*, J. Phys. Chem. **6**, 2132 (1963).

[137] N. Subramanian *et al.*, Physica B **351**, 5 (2004).

[138] N. Bandaru *et al.*, J. Phys. Chem. C **118**, 3230 (2014).

[139] V. K. Gudelli *et al.*, J. Phys. Chem. C **117**, 21120 (2013).

[140] B. Sundarakannan *et al.*, Solid. State. Commu. **124**, 24115 (2002).

[141] E. DiMasi *et al.*, Phys. Rev. B **54**, 13587 (1996).

[142] C. Wang *et al.*, Inorg. Chem. **34**, 5524 (1995).

[143] J. Hu *et al.*, Sci. Rep. **6**, 18674 (2016).

[144] Z. J. Xiang *et al.*, Phys. Rev. Lett. **115**, 226401 (2015).

[145] D. V. Khveshchenko, Phys. Rev. Lett. **87**, 206401 (2001).

[146] X. Du *et al.*, Phys. Rev. Lett. **94**, 166601 (2005).

[147] Z. Ren *et al.*, Phys. Rev. B **82**, 241306(R) (2010).

[148] D. J. Kim *et al.*, Sci. Rep. **3**, 3150 (2013).

[149] A. A. Abrikosov, *Fundamentals of the Theory of metals*, North-Holland, Amsterdam (1988).

[150] M. Novak *et al.*, Phys. Rev. B **91**, 041203(R) (2015).

[151] N. Wakeham *et al.*, Phys. Rev. B **93**, 205152 (2016).

[152] O. Pavlosiuk *et al.*, Sci. Rep. **6**, 38691 (2016).

[153] Y.-Y. Wang *et al.*, Phys. Rev. B **94**, 041103(R) (2016).

[154] G. Zheng *et al.*, Phys. Rev. B **93**, 115414 (2016).

[155] Y. Luo *et al.*, App. Phys. Lett. **107**, 182411 (2015).

[156] C.-L. Zhang *et al.*, Phys. Rev. B **95**, 085202 (2017).

[157] L. P. He *et al.*, Phy. Rev. Lett. **113**, 246402 (2014).

[158] J. G. Analytis *et al.*, Nat. Phys. **6**, 960 (2010).

[159] P. Sergelius *et al.*, Sci. Rep. **6**, 33859 (2016).

[160] H. Zhang *et al.*, Phys. Rev. Lett. **111**, 066801 (2013).

[161] A. A. Burkov *et al.*, Phys. Rev. Lett. **105**, 066802 (2010).

[162] D. Hsieh *et al.*, Nature **460**, 1101 (2009).

[163] Z.-H. Pan *et al.*, Phys. Rev. Lett. **106**, 257004 (2011).

[164] L. Zhao *et al.*, Nat. Mater. **13**, 580 (2014).

[165] S. G. Buga *et al.*, Chem. Phys. Lett. **631-632**, 97 (2015).

[166] P. Dutta *et al.*, Sci. Rep. **7**, 4883 (2017).

[167] A. Pariari *et al.*, Sci. Rep. **7**, 40327 (2017).

[168] Q. Li *et al.*, Nat. Phys. **12**, 550 (2016).

[169] Y. Zhang *et al.*, Nat. Commun. **8**, 15512 (2017).

[170] M. Zeng *et al.*, arxiv:1504.03492v1 (2015).

[171] N. Kumar *et al.*, Phys. Rev. B **93**, 241106(R) (2016).

[172] P.-J. Guo *et al.*, Phys. Rev. B **93**, 235142 (2016).

[173] L.-K. Zeng *et al.* Phys. Rev. Lett. **117**, 127204 (2016).

[174] X. H. Niu *et al.* Phys. Rev. B **94**, 165163 (2016).

[175] J. Nayak *et al.* Nat. Commun. **8**, 13942 (2017).

[176] R. Lou *et al.*, Phys. Rev. B **95**, 115140 (2017).

[177] Y. Wu *et al.*, Phys. Rev. B **94**, 081108(R) (2016).

[178] R. Singha *et al.*, Phys. Rev. B **96**, 245138 (2017).

[179] Y.-Y. Wang *et al.*, Phys. Rev. B **94**, 041103(R) (2016).

[180] C. Xu *et al.*, Phys. Rev. B **93**, 195106 (2016).

[181] B. Shen *et al.*, Phys. Rev. B **93**, 195119 (2016).

[182] Z. Yuan *et al.*, Phys. Rev. B **93**, 184405 (2016).

[183] Y. Li *et al.*, Phys. Rev. B **94**, 121115(R) (2016).

[184] J. J. Murray *et al.*, J. Crys. Growth **15**, 231 (1972).

[185] P. Jensen *et al.*, Acta Chem. Scan. **20**, 403 (1966).

[186] V. P. Jovanović *et al.*, Phys. Rev. B **81**, 134520 (2010).

[187] Y. Q. Zhang *et al.*, Appl. Phys. Lett. **97**, 172502 (2010).

[188] A. Collaudin *et al.*, Phys. Rev. X **5**, 021022 (2015).

[189] J. Wang *et al.*, Sci. Rep. **7**, 15669 (2017).

[190] J. Hu *et al.*, Phys. Rev. Lett. **95**, 186603 (2005).

[191] J. B. He *et al.*, Phys. Rev. B **95**, 195165 (2017).

[192] C. Shekhar *et al.*, arXiv:1703.03736 (2017).

[193] S. Uji *et al.*, Phys. Rev. B **54**, 9332 (1996).

[194] P. Auban-Senzier *et al.*, J. Physique I **5**, 1301 (1995).

[195] E. Ohmichi *et al.*, Phys. Rev. B **57**, 7481 (1998).

[196] H. Weiss *et al.*, Phys. Rev. B **59**, 12370 (1999).

[197] P. M. Chaikin *et al.*, Synthetic Metals **27**, B163 (1988).

[198] A. V. Kornilov *et al.*, Phys. Rev. B **76**, 045109 (2007).

[199] A.V. Korndov *et al.*, J. Low Temp. Phys. **142**, 305 (2006).

[200] N. D.-Leyraud *et al.*, Nature **447**, 565 (2007).

[201] J. Singleton *et al.*, Phys. Rev. Lett. **104**, 86403 (2010).

[202] S. E. Sebastian *et al.*, Phys. Rev. B **81**, 214524 (2010).

[203] S. E. Sebastian *et al.*, Proc. Natl. Acad. Sci. USA **107**, 6175 (2010).

[204] E.A. Yelland *et al.*, Phys. Rev. Lett. **100**, 047003 (2008).

[205] P. S. Varma *et al.*, arXiv:1602.05269 (2016).

[206] R. W. Start *et al.*, J. Low. Temp. Phys. **26**, 763 (1976).

[207] A. B. Pippard, Proc. R. Soc. A **270**, 1 (1962);

[208] A. B. Pippard, Proc. R. Soc. A **287**, 165 (1965).

[209] M. Y. Azbel *et al.*, Phys. Rev. Lett. **59**, 582 (1987).

[210] T. Osada *et al.*, Sol. Stat. Commun. **69**, 1169 (1989).

[211] Z. Wang *et al.*, Phys. Rev. B **93**, 121112(R) (2016).

[212] Sudesh *et al.*, Sci. Rep. **7**, 46062 (2017).

[213] H. Takatsu *et al.*, Phys. Rev. Lett. **111**, 056601 (2013).

[214] M. Udagawa *et al.*, Phys. Rev. Lett. **117**, 086401 (2016).

[215] Z-M. Yu *et al.*, Phys. Rev. Lett. **117**, 077202 (2016).

[216] T. E. O'Brien *et al.*, Phys. Rev. Lett. **116**, 236401 (2016).

[217] K. Deng *et al.*, Nat. Phy. **12**, 1105 (2016).

[218] K. Koepernik *et al.*, Phys. Rev. B **93**, 201101(R) (2016).

[219] G. Chang *et al.*, Science Adv. **2**, e1600295 (2016).

[220] I. Belopolski *et al.*, Phy. Rev. B **94**, 085127 (2016).

[221] F. Fei *et al.*, Phys. Rev. B **96**, 041201(R) (2017).

[222] T-R. Chang *et al.*, Phys. Rev. Lett. **119**, 026404 (2017).

[223] R. Singha *et al.*, Phys. Rev. B **97**, 155120 (2018).

[224] Y. Wang *et al.*, Nat. Commun. **7**, 13142 (2016).

[225] J. P. Ulmet *et al.*, Phys. Rev. B **38**, 7782 (1988).

[226] A. A. Burkov, Phys. Rev. B **96**, 041110(R) (2017).

[227] S. Nandy *et al.*, Phys. Rev. Lett. **119**, 176804 (2017).

[228] P. Li *et al.*, arXiv:1803.01213 (2018).

[229] H. Li *et al.*, Phys. Rev. B **97**, 201110(R) (2018).

[230] Y. J. Wang *et al.*, arXiv:1801.05929 (2018).

[231] N. Kumar *et al.*, Phys. Rev. B **98**, 041103(R) (2018).

[232] A. M. Nazmul *et al.*, Phys. Rev. B **77**, 155203 (2008).

[233] J. H. Maas *et al.*, Z. Metallkd. **74**, 294 (1983).

[234] K-W. Chen *et al.*, Phys. Rev. Lett. **120**, 206401 (2018).

[235] P. J. W. Moll *et al.*, Nat. Commun. **7**, 12492 (2016).

[236] B. J. Ramshaw *et al.* Nat. Commun. **9**, 2217 (2018).

[237] S. Pezzini *et al.*, Nat. Phys. **14**, 178 (2018).

[238] Y. Zhou *et al.*, Proc. Natl. Acad. Sci. USA **113** 2904 (2016).

[239] L. He *et al.*, npj Quan. Mater. **1**, 16014 (2016).

[240] F. F. Tafti *et al.*, Phys. Rev. B **95**, 014507 (2017).

[241] Z. Chi *et al.*, npj Quan. Mater. **3**, 28 (2018).

[242] L. Fu *et al.*, Phys. Rev. Lett. **100**, 096407 (2008).

[243] C. Nayak *et al.*, Rev. Mod. Phys. **80**, 1083 (2008).

[244] B. Bradlyn *et al.*, Science **353**, aaf5037 (2016).

[245] B. Q. Lv *et al.*, Nature **546**, 627 (2017).

[246] J.-Z. Ma *et al.*, Nat. Phys. **14**, 349 (2018).

[247] I. Vobornik *et al.*, Nano Lett., **11**, 4079 (2011).

[248] H. B. Zhang *et al.*, Adv. Mater. **24**, 132 (2012).

[249] P.-H. Chang *et al.*, Nano Lett., **14** 3779 (2014).

[250] Y. Fan *et al.*, Nat. Mater. **13**, 699 (2014).

[251] J. Tian *et al.*, Solid State Commun. **191**, 1 (2014).

[252] R. D. Y. Hills *et al.*, Phys. Rev. B **95**, 214103 (2017).

[253] Q. Wang *et al.*, Nano Lett. **17**, 834 (2017).

[254] S. Chi *et al.*, Adv. Mater. **30**, 1801372 (2018).